AALBORG UNIVERSITY
DENMARK

Control and Driving Methods for LED Based Intelligent Light Sources

Beczkowski, Szymon

Publication date:
2012

Document Version
Publisher's PDF, also known as Version of record

Control and driving methods for LED based intelligent light sources

Szymon Bęczkowski

August 2012

Department of
ENERGY TECHNOLOGY
Aalborg University

E.T.

Abstract

High power light-emitting diodes allow the creation of luminaires capable of generating saturated colour light at very high efficacies. Contrary to traditional light sources like incandescent and high-intensity discharge lamps, where colour is generated using filters, LEDs use additive light mixing, where the intensity of each primary colour diode has to be adjusted to the needed intensity to generate specified colour.

The function of LED driver is to supply the diode with power needed to achieve the desired intensity. Typically, the drivers operate as a current source and the intensity of the diode is controlled either by varying the magnitude of the current or by driving the LED with a pulsed current and regulate the width of the pulse. It has been shown previously, that these two methods yield different effects on diode's efficacy and colour point.

A hybrid dimming strategy has been proposed where two variable quantities control the intensity of the diode. This increases the controllability of the diode giving new optimisation possibilities. It has been shown that it is possible to compensate for temperature drift of white diode's colour point using hybrid dimming strategy. Also, minimisation of peak wavelength shift was observed for InGaN diodes.

Control of trichromatic luminaires, dimmed with either pulse-width modulation or amplitude modulation, cannot be optimised. Introduction of hybrid dimming mechanism creates three additional degrees of freedom therefore luminaire parameters such as luminous flux, efficacy and colour quality can be maximised. Simulations show that the gamut of the device can be increased, especially in the cyan colour range for RGB luminaires.

A current-voltage model of light-emitting diode is presented. It utilises the fact that instantaneous values of diode's current and voltage correspond uniquely to a set of diode's colorimetric properties, like tristimulus values. This model can be used for colorimetric feedback in colour control loop. The model was created in thermal steady-state conditions and its validity has been tested with a diode driven with a pulsed current. The model can also be used to create highly accurate luminaire model.

Finally, a dual interleaved buck converter has been proposed for driving high power light-emitting diodes. Interleaving two converters lowers the output ripple current thus lowering the requirement on the output capacitor. It has been shown that at the expense of cost and increased complexity an efficient design can be created for supplying high current to LEDs without the need for electrolytic capacitors.

Contents

3

List of abbreviations, symbols and physical constants

AC	alternating current
AM	amplitude modulation (same as CCR)
DC	direct current
IC	integrated circuit
IV	current-voltage
PI	proportional–integral (controller)
PC	phosphor-converted (diode)
ADC	analog-digital conversion
CCR	continous current reduction (same as AM)
CCT	correlated colour temperature
CFF	critical flicker frequency
CIE	Commission Internationale de l'Eclairage
CPU	central processing unit
CRI	colour rendering index
DAC	digital-analog conversion
DCR	DC resistance
DSP	digital signal processor
EMI	electro-magnetic interference
FFB	flux feedback
HID	high-intensity discharge
LED	light-emitting diode
PCB	printed circuit board
PFC	power factor correction
PWM	pulse width modulation
RGB	red, green and blue
SRH	Shockley-Read-Hall recombination
TFF	temperature feed forward
TIM	thermal interface material
TCS	test colour sample
VRM	voltage regulation module
CCFB	colour coordinates feedback
FWHM	full width at half maximum
MOSFET	metal-oxide-semiconductor field-effect transistor

λ	wavelength	m
v	frequency of optical radiation	Hz
η	efficiency	p.u.
η_{lum}	luminous efficacy	lm/W
t	time	s
τ	time constant	s
F	luminous flux	lm
A	area	m^2
C	capacitance	F
L	inductance	H
R	resistance	Ω
P	power	W
P_{rad}	radiometric power	W
i	current	A
v	voltage	V
d	duty cycle	p.u.
f	frequency	Hz
T	temperature	°C, K
R_i	colour rendering index for i-th sample	—
R_a	general colour rendering index	—
E_g	bandgap energy	eV
C_{th}	thermal capacitance	J/K
R_{th}	thermal resistance	K/W
CT/CCT	colour temperature/corelated colour temperature	K
FWHM	full width at half maximum	eV, nm
x, y	colour coordinates in CIE 1931 colour space	—
u, v	colour coordinates in CIE 1960 colour space	—
u', v'	colour coordinates in CIE 1976 (L', u', v') colour space	—
a^*, b^*	colour coordinates in CIE 1976 (L^*, a^*, b^*) colour space	—
$\overline{x}, \overline{y}, \overline{z}$	colour matching functions	p.u.
X, Y, Z	tristimulus values	W, lm

$e = 1.6022 \cdot 10^{-19}\,$C   elementary charge
$c = 2.9979 \cdot 10^{8}\,$m/s   speed of light in vacuum
$h = 6.6261 \cdot 10^{-34}\,$Js   Planck constant
$h = 4.1357 \cdot 10^{-15}\,$eVs   Planck constant
$k = 1.3807 \cdot 10^{-23}\,$J/K   Boltzman constant
$k = 8.6175 \cdot 10^{-5}\,$eV/K   Boltzman constant

1 Introduction

Intelligent lighting such as projectors and moving heads are used, whenever there is a need for a light source that can be tuned to individual needs during lamp operation. Typically these lamps can have programmable light colour, intensity, focus and sometimes the ability to project special shapes such as patterns or logos. Intelligent lighting is commonly used in theatres, concerts halls and clubs.

Figure 1.1: Martin smartMAC moving head (left) and Exterior 1200 image projector (right).

Two examples of such a lamps are shown in figure 1.1. Moving head lamps are designed with the ability to pan and tilt the light beam. Projectors, on the other hand, are fixed at specific target during installation. Both lamp types can be designed to provide a narrow or diffused beam of light, depending on the need.

Intensity of the light provided by a luminaire must be high, so typically high-intensity discharge lamps are used as a light source. A compact passive-cooled luminaire like the smartMAC uses a 150 W HID lamp while the Exterior 1200 uses a 1200 W metal halide lamp yielding ca. 10 and 92 klm, respectively. Because the output light beam shape is very different from the light source profile, the optics inside the lamp must collect and collimate. A portion of the light is lost in the process. The output light flux for aforementioned luminaires is ca. 2700 lm for the smartMAC and 20–35 klm for the Exterior 1200 (depending on the configuration). As can be seen, the efficiency of the luminaire is around 30 %, not including the power needed to drive the control electronics.

Above flux values are valid for generation of white light. Colour light is created by inserting a colour filter in the light beam (fig. 1.2). The transmissivity of the filters depends on the desired colour and its saturation. Saturated red and blue colour

Figure 1.2: Martin MAC III moving head luminaire and its blow-out diagram showing the 1.5 kW discharge light source, dimming mechanism and the colour wheel.

filters can have transmission as low as few percent. This lowers the overall efficacy of the luminaire. Moreover, it is hard to create filters with sharp characteristics to create saturated colours. Transition from one colour to another requires mechanical change of the filter in the path of the light. Depending on the filter arrangement, it may be necessary to transition through a different colours to obtain the desired colour.

Dimming of high power HID lamps is done by either a high frequency lamp ballast (limited dimming range) or inserting a specially shaped shutter in the light path (fig. 1.2). When the light is to be turned off for a short period of time the full-blocking shutter is placed in front of the light source. This is done because metal halide lamps cannot ignite unless they are cold because the high pressure obtained during normal operation prevents the lamp to restart. This requires a few minute cool down after the lamp was turned off.

Lifetime of HID lamps is limited to a few thousands hours. At the end of their lifetime high-intensity discharge lamps exhibit phenomenon called cycling, when the lamps periodically turn on and off because of the ageing effects. Sometimes the stress caused by off-on cycles or the increased pressure of the gas inside the lamp can lead to an explosion of the lamp tube, containing small amount of mercury.

Constantly increasing intensity of LED sources already allows their use in low power (watts–tens of watts) applications such as replacement for conventional halogen and incandescent light sources in general lighting. Slowly, they enter medium power (hundreds of watts) applications like moving heads. LEDs do not contain any toxic chemicals and have much longer lifetime than HID lamps. Long lifetime decreases the service costs of the luminaire.

Compared to incandescent and discharge lamps, LEDs emit a narrow spectrum light that produces saturated colours. This means the white light cannot be directly generated by a single LED die. White light can be generated using either two or

more pure colour LEDs or a phosphor coated blue LED. Similarly to obtain any other colour in the device gamut, a combination of primary colours must be used. Generated colour range is not limited to the number of colour filters used, but on the accuracy of a colour control scheme. High bandwidth of intensity control allows for fast transition between colours and for strobing without the need for mechanical shutter. Removing mechanical parts like colour wheel or shutters decreases luminaire's weight and size and, at the same time, increases the reliability of the device.

Using light-emitting sources in luminaires comes at a price of increased complexity in colour control, thermal management, optical system and power electronics controlling LED light sources. Colour control system depends on the accuracy needed in the luminaire. It can be as simple as open loop control or an advanced feedback loop compensating for diode's changing colour point. LED's properties depend on the junction temperature therefore the diodes should be kept as cool as possible. High power LEDs can dissipate even 80 % of their input power in a few square millimetre area chip. The thermal management system should remove the heat from the LED structure as efficiently as possible or the junction temperature will increase and the light intensity and lifetime of the LED will drop.

This work is part of an INLED project (Intelligent Light Emitting Diodes), a collaboration between Martin Professional, Aalborg University (Institute for Energy Technology and Institute for Nano-Physics) and the Danish National Advanced Technology Foundation (Højteknologifonden). The objective of the project is to increase the knowledge in LED based luminaire technology. The knowledge gained from the project should be useful for designing substitutes for existing technologies. The project focuses on creating: optics with nano scale coatings that would maximise the light transmission from LEDs to the output port, efficient power electronic drivers supplying power to the diodes and a heat management system for the luminaire. *INLED PROJECT*

The aim of the work shown in this dissertation is to research the driving of high power light-emitting diodes and to create an intelligent LED driver that would fully utilise the benefits of solid-state lighting technology. *MOTIVATION*

1.2 RELATED WORK

A research of the state of the art in solid-state lighting has been conducted to show current solution of the existing problems and show potentially beneficial research areas. Three main topics are covered: properties of LED devices, control of luminaires and methods of driving light-emitting diodes.

9

With the introduction of high power blue GaN LEDs by Nakamura of Nichia Corporation LEDs finally gained the potential to enter general illumination market. Four basic diode colours: red, green, blue and white became available on the market as high power devices in the mid 2000s. At this point scientist started investigating their driving properties. At that time phosphor-converted white LEDs had high enough efficacy for practical lighting applications. Lighting Research Center at Rensselaer Polytechnic Institute pioneered in colorimetric research of high-power devices. Dyble et al. [1] analysed the chromaticity shifts of PC white LED under pulse width modulation and amplitude modulation dimming. A year later research on red, green, blue and white diodes was conducted by Gu et al. [2] on the effects of different dimming schemes on diodes' spectra, luminous flux and efficacy. In 2007, Manninen and Orreveteläinen [3] from Helsinki University of Technology published their work on spectral and thermal behaviour of AlGaInP diodes under PWM dimming. General consensus from these three research papers was that PWM dimming method provides linear dimming in 0–100 % range with low colour shifts. AM on the other hand yielded higher efficacies at lower current levels but at the price of much higher colour shifts and limited dimming range.

DIMMING PROPERTIES

Work on more advanced dimming mechanisms started with Ashdown [4] proposing the use of pulse-code modulation to remove the need of hardware PWM generators to dim the diodes.

HYBRID DIMMING In 2009, Tse et al. [5] from Hong Kong Polytechnic University proposed a general driving scheme of using two current levels to control LEDs. Using low current magnitude together with high current PWM signal both high efficiency and limited colour shifts can be achieved. A variation of their general driving technique, where one of the currents is set to zero, was investigated in this dissertation.

DRIVING CURRENT In 2007, Schmid et al. [6] measured the effect of the typical driving currents on diode performance. The accuracy of the results is limited due to the measurement hardware used but it shows the effect of ripple content in the diode current on the light output.

1.2.2 Thermal properties

Thermal properties of high-power LEDs have been a topic for many research programmes since mid 2000s. Scientists quantified the effect of junction temperature on such parameters as: luminous flux, colour point, spectrum shape and lifetime of the device. Three major research topics can be identified on the thermal properties of LEDs: methods for measuring the junction temperature, estimating the junction temperature using a thermal model of LED luminaires and the research on the effect of temperature on the device properties.

The measurement of the junction temperature is done mostly through indirect methods, where the temperature dependent parameter is measured and using model or previous calibration the temperature is calculated.

In 2004 Xi et al. [7] proposed a method based on forward voltage measurement. In order to calibrate the measurement, the diode is measured when driven with very small duty cycle, typically 0.1 %, to reduce the self heating effect. This method was used throughout the writing of this dissertation. Another method provided by Xi et al. [8] is based on the relationship between the peak of the spectrum and the junction temperature.

A method based on the diode spectrum was presented by Chhajed et al. [9]. It is based on the high energy slope of the diode's spectrum. When plotted in semilogarithmic scale, the slope is proportional to the carrier temperature.

Instead of measuring the junction temperature indirectly, a thermal model of the diode can be used to estimate it. Farkas et al. [10] pioneered the use of diode thermal model. They applied a method described by Székely in 1988 [11], used previously for high power silicon chips to measure and model the thermal path of the dissipated heat. This thermal model is used further in the dissertation to simulate the performance of both LEDs and whole luminaires.

The effect of junction temperature on InGaN and AlGaInP has been documented by Chhajed et al. [12] in 2005. They measure the effect of varying the junction temperature on colour diodes and on trichromatic luminaires composed of these diodes. Moreover, they described the LED spectrum model based on a Gaussian function. They used the model to find a good combination of primary diode colours to create a luminaire with high luminous efficacy and colour rendering index.

In 2006, Man and Ashdown [13] extended the model presented by Chhajed into double Gaussian model composed of sum of two Gaussian curves, accurately modelling the LED spectrum in wide range of temperatures.

The linearity of PWM dimming method is limited to a constant heatsink temperature case but this temperature changes with average driving current, bending the current-luminous flux relationship. Garcia et al. [14] created a flux estimator basing on the LED case and ambient temperatures to deal with transient and steady-state behaviour of the luminous flux. This estimator can accurately predict the instantaneous value of luminous flux, therefore it allows a linear dimming behaviour and precise intensity control, but lack of the colour shift information limits the practical use to control of a phosphor-converter white LEDs or a single colour diode. It is not sufficient for precise colour control of polychromatic luminaires.

Hui and Qui [15] analysed the static performance of the LED-heatsink system in 2009. They showed that above certain thermal resistance in the heat flow path limiting the driving current will increase the maximum intensity of the diode. This phenomenon is very important for driving AlGaInP diodes which have very high temperature dependency.

Huang and Tang [16] presented a complete thermal-electrical-luminous model of an LED luminaire in 2009. Derivation of system coefficients was done using power perturbation on individual diodes and system identification methods. Unfortunately, the model disregards the colour shifts and nonlinearities present in LED based luminaires.

1.2.3 Lifetime

FAILURE MECHANISMS In 2004, Narendran et. al. [17] analysed the failure mechanisms in white LEDs. Junction temperature was identified as major contributor in light output degradation phenomenon. Since then, many long time tests have been performed in order to create a reliable model of light output degradation. Jacob et al. [18] analysed the failure modes of high power LEDs in 2006. They mention a few separate failure mechanisms: shunting of the structure through parasitic dendrites growing on the structure, leakage paths in the active area or bond wire dislocations.

GALLIUM NITRIDE DIODES In 2008, Hu et al. [19] performed a degradation test on GaN diodes. They report a change in thermal structure of the diodes. The increase in thermal resistance of the package increases the junction temperature and speeds up degradation.

GALLIUM PHOSPHIDE DIODES Mathematical model of light output degradation for AlGaInP diodes was derived by Grillot et al. [20] in 2006. They proved that useful lifetime of the device is a linear function of current density and logarithmic function of stress time.

DRIVING CURRENT IMPACT Meneghini et al. [21] and Buso et al. [22] compared the LED output degradation speed under DC and pulsed driving current. Their reliability tests showed that the device lifetime is similar under both driving conditions. However, different families of devices showed different effect on both driving conditions, indicating that the internal structure of the device and package may influence the reliability behaviour under various driving currents.

1.2.4 Luminaire control

Many different control techniques have been developed over the years to control light-emitting diodes based luminaires. Basic colour control loops have been presented by Deurenberg et al. [23].

OPEN LOOP The simplest open loop control is very easy to implement as it requires only a single point calibration but it does not compensate for self heating of the diode structure, change of ambient temperature or the reduced intensity with time.

COLOUR FEEDBACK Most common feedback mechanism implemented to control LED luminaires are the colour sensors. Subramanian et al. [24] describe a simple colour control loop that reduces the colour shift of the luminaire compared to an open loop solution. The dynamics of this system is described later by Subramanian and Gaines [25]. Over the years many researchers used various colour sensors to control luminaires:

Ackermann et al. [26], Lim et al. [27] and Chang et al. [28]. The consensus is that colour sensors provide easy feedback method with relatively good accuracy but LED spectra shifts can create colour errors. Additionally, the colour sensor stability is a major concern. To increase the accuracy of the colour sensors Robinson and Ashdown [29] proposed an advanced feedback solution capable of estimating the spectral shifts.

Subramanian et al. [24] proposed using a single photodetector instead of colour sensor and measure each of the diodes separately using a timing scheme.

As temperature is the main cause of the variation of diodes' parameters, some control schemes are based on the temperature dependence models. Moisio et al. [30] measured the heatsink temperature and approximated the intensity of the LEDs installed in the luminaire. Forward voltage of the diode is proportional to the junction temperature at a single current level. Qu et al. [31] measured the diode voltage and converted it directly to tristimulus values.

Huang et al. [32] described the system model of a multi-chip polychromatic luminaire. They used power perturbation and system identification methods for each colour string of diodes.

1.2.5 Optimisations

Luminaires can be optimised from a few different angles. The number of primary colours and the exact device choice to be installed in the luminaire can be subjected to optimisation procedures. Žukauskas et al. [33] analysed the effect of number of primaries in the luminaire on the colour quality and luminous efficacy achievable by the luminaire. Chhajed et al. [12] used a Gaussian LED spectrum model to choose the best combination of three colours yielding high CRI value in the required colour range.

When the luminaire consists of more than three primary colours, the colour control system becomes underdetermined and diode control can be optimised. Ries et al. [34] showed the possibility to optimise such parameters of luminaires as luminous flux, efficacy and colour rendering index. Ou-Yang and Huang [35] showed a method to estimate the gamut of multi-primary LED based luminaires.

In 2010, Lin [36] presented a method to optimise the CRI of a luminaire using mathematical formulations of the problem and numerical method based on the complex method.

1.2.6 LED driver

The work of Schmid et al. [6] on the impact of driving current shape and various research on different dimming techniques indicates that in order to achieve high efficacy the diode should be driven with a DC current. Van der Broeck et al. [37]

analysed different converter topologies for driving LEDs from a DC voltage source using both DC and pulsating current. They present different types of isolated and non-isolated converters describing their output current shape. Their conclusion is that pulsed output current converters contain, in general, less components (like output capacitor) and therefore may be beneficial for the lifetime of the converter.

Many different topologies were applied for driving high current LEDs. Depending on the application, solutions include using a buck by Torres et al. [38], boost by Xiaoru and Xiaobo [39], Ćuk by de Britto et al. [40], flyback by Pan et al. [41] or SEPIC by Zhongming et al. [42] etc. Most of the research on LED drivers focus on high-power LEDs supplied with a current up to 700 mA. Although some of the solutions presented for these diodes can be easily scaled to a diode driven with 13.5 A, the high current converter design calls for more advanced solution.

Early processors were supplied with a few volts and tens of amps, similarly to high power LEDs. For this kind of load Xunwei et al. [43] proposed using a multiphase interleaved buck converters.

1.3 SCIENTIFIC CONTRIBUTIONS

Following contributions of this work have been identified as extending the current state of the art.

HYBRID PWM/AM DIMMING

Introduction of hybrid PWM/AM dimming technique (chapter 3.10.3). This dimming technique is a combination of pulse width modulation with variable peak current amplitude. It can be easily adapted to current designs as integrated LED drivers typically have the possibility to use both PWM and AM dimming.

Typically, one variable quantity is used to control the intensity of the diode: either a duty cycle or DC current. By controlling a single LED with both peak current and duty cycle an additional degree of freedom appears and LED parameters can be optimised.

Hybrid dimming mechanism can be used e.g. to reduce the colour point shifts of a white, phosphor converted diode under varying heatsink temperature or to minimise spectra shifts in InGaN diodes.

Application of hybrid dimming mechanism to polychromatic luminaires creates opportunities to optimise luminaires' control, increase their efficacy and device gamut (chapter 4.2.2). Using this technique, optimisation possibilities are given even for di- and trichromatic luminaires.

CURRENT VOLTAGE LED MODEL

LED empirical model, described in chapter 3.11, based on instantaneous values of current and voltage of the diode can form a basis of a luminaire colour control scheme (chapter 4.1.6). The model is valid for any form of diode dimming and accurately predicts colour shifts created by the changes of ambient temperature and by the dimming technique. The model can be used as a feedback mechanism for precise colour control.

An interleaved buck topology was proposed for driving high current LED light sources. Because of relatively low dynamic resistance the working point of the driver can be set so that the converter always works close to 50 % duty cycle where the ripple cancellation effect is the strongest. This removes the need for high value, electrolytic output capacitors.

Some of the work presented in this dissertation has also been published in other sources:

1 S. Bęczkowski. Advanced dimming strategy for solid state luminaires. In *Proceedings of the 10th International Conference on Solid State Lighting*. pp. 1–6. SPIE International Society for Optical Engineering. 2010.

2 S. Bęczkowski, S. Munk-Nielsen. LED spectral and power characteristics under hybrid PWM/AM dimming strategy. In *Proceedings of the IEEE Energy Conversion Congress and Exposition, ECCE 2010*, pp. 731–735. IEEE press. 2010.

3 S. Bęczkowski, S. Munk-Nielsen. Dual interleaved buck converter for driving high power LEDs. In *Proceedings of the 2011—14th European Conference on Power Electronics and Applications, EPE 2011*, pp.1–6. 2011.

4 L. Török, S. Bęczkowski, S. Munk-Nielsen, J. Gadegaard, T. Kari, K. Pedersen. High output LED-based profile lighting fixture. (accepted for publication) *Proceedings of IECON 2011—37th Annual Conference of the IEEE Industrial Electronics Society, IECON 2011*, 2011.

5 DK PA 2011 70529 patent application. S. Bęczkowski. Method of controlling illumination device based on current-voltage model.

1.4   METHODOLOGY

The manufacturing of light-emitting diodes is a complex process performed in clean room environment. Diode structures are created using epitaxial growth and the diode colour is controlled by the GaN/InN ratio or by the AlInP composition [44]. On account of local variations, colour point of diodes in a batch can differ from sample to sample. The same applies to intensity and forward voltage magnitude. Manufacturers split the diode batches into smaller bins with similar diode's parameters like forward voltage, intensity and colour point.

Data shown in the dissertation has been obtained using measurements on particular diode sample. No statistical analysis has been done, therefore the results apply to the measured diodes and do not apply to the diode batch in general. However, the principles demonstrated on particular devices are applicable to the whole batch

but may yield different results. Different internal diode structures may show different behaviour. All tests were performed on high power, state of the art devices.

Tests performed at fixed temperatures are performed using constant heatsink temperature. The use of constant junction temperature eliminates the impact of thermal structure of the diode on results, but its measurement a complex process, therefore it was not used in the data gathering. Furthermore, the experiments can be easily recreated using inexpensive hardware.

1.4.1 Measurement hardware

SPECTROMETER Optical measurements were performed using an Instrument Systems CAS 140 CT array spectrometer. This spectrometer uses a diffraction grating technique for measurement of the visible part of the light spectrum. Light is directed on an optical component with a periodic structure which diffracts the light. Diffracted light is analysed by a CCD detector. The spectrometer can analyse light within 360–830 nm range with 2.2 nm resolution and 0.5 nm data point interval.
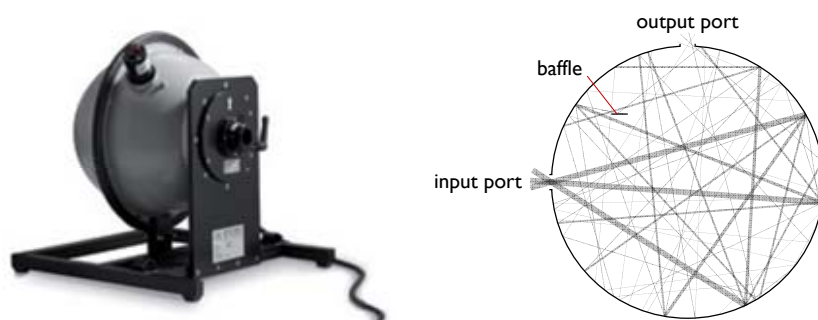

Figure 1.3: Instrument Systems ISP250 integrating sphere used in the test setup (left) and the principles of integrating sphere operation (right). Input beam is reflected diffusely inside the sphere many times before hitting the output port. A baffle inside the sphere blocks the input light from hitting the output port directly.

INTEGRATING SPHERE A 25 cm diameter Instrument Systems ISP250 integrating sphere shown in figure 1.3 is used to gather the light from device under test. Inner surface of the sphere is coated with diffusely reflecting material, barium sulphate ($BaSO_4$), of a well defined reflectance. Light is diffusely reflected from the walls many times before it hits the output port of the sphere, therefore the measurement is not dependent on the shape of the input light beam. An Instrument Systems ISP500-220 adapter plate is used to mount a LED test fixture.

TEST FIXTURE Instrument Systems LED-850 test fixture is used for LED assembly. It is possible to test various LED types from different manufacturers with special adapters. These adapters provide electrical contacts for four wire sensing and a thermal connection

Table 1.1: National Instruments compactDAQ modules used in the experiments.

MODULE	RESOLUTION	SAMPLING RATE	RANGE	COMMENTS
NI 9201	12 bit	500 kS/s	±10 V	8-channel
NI 9229	24 bit	50 kS/s	±60 V	4-channel (isolated)
NI 9227	24 bit	50 kS/s	5 A RMS	4-channel

between LED and thermally controlled plate. Arroyo Instrument 5310 TECsource temperature controller was used to control the temperature of the plate.

Measurements of power converter were done using following hardware: Fluke 8845 A multimeter, 100 MHz 4 channel Tektronix TDS 3014C digital phosphor oscilloscope, 50 MHz Tektronix TCP202 current probe, Delta Elektronika SM 52-AR-60 power supply and Zentro-Elektrik EL1000 electronic load.

NI 6215 data acquisition module containing 16 analog inputs (16 bit, 250 kS/s) was also used for bigger tests that needed high number of input channels.

For electrical measurements a National Instruments compactDAQ system was used. The system consists of a NI CDAQ-9172 chassis with interchangeable measurement modules (table 1.1). Voltage output modules were used to control LED drivers. Current and voltage inputs were used to acquire electrical quantities.

1.5 OUTLINE

The first chapter gives background to the topic of this dissertation, followed by review of previous scientific work done by other parties to show the state of the art in light-emitting diodes control. Finally methodology used in the work is described. CHAPTER 1

Colour theory chapter gives an insight of how the light is perceived by the human eye and how it is measured. Various colour spaces, used throughout the dissertation, are defined. The definitions of light quality and colour distance are given in order to quantify the performance of the colour control. CHAPTER 2

The principles of operation and properties of light-emitting diodes are described in the third chapter. Firstly the physical structures of the diodes are discussed. Optical and electrical properties are analysed with focus on the parameter change with respect to junction temperature variations. The lifetime of the devices is analysed. The impact of dimming the diodes with different methods is presented. Hybrid dimming technique is introduced and its properties in increasing the controllability of LEDs are analysed. In the end, an empirical model of the light-emitting diodes is presented and verified. CHAPTER 3

Luminaire control is presented in the fourth chapter. Firstly the review of state of the art control methods is given. A colour control scheme based on the empirical model, described in chapter three, is presented. Finally optimisation routines for designing and controlling polychromatic luminaires are described. CHAPTER 4

17

CHAPTER 5 Fifth chapter reviews available power converter topologies with respect to driving light-emitting diodes. An interleaved buck topology is analysed and its benefits and drawbacks are discussed. Power stage and control are designed. Laboratory results are presented and discussed.

CHAPTER 6 Final sixth chapter summarises the dissertation by providing an overview of the results and gives recommendations on the future work.

2 Colour theory

Colour science has its origins in late 17th century when Sir Isaac Newton conducted his experiments on the nature of light. Using two prisms Newton showed that white light can be divided into separate colours and that pure colours cannot be divided more. In order to prove that the prism is not colouring the light, he reconstructed white light using pure colours.
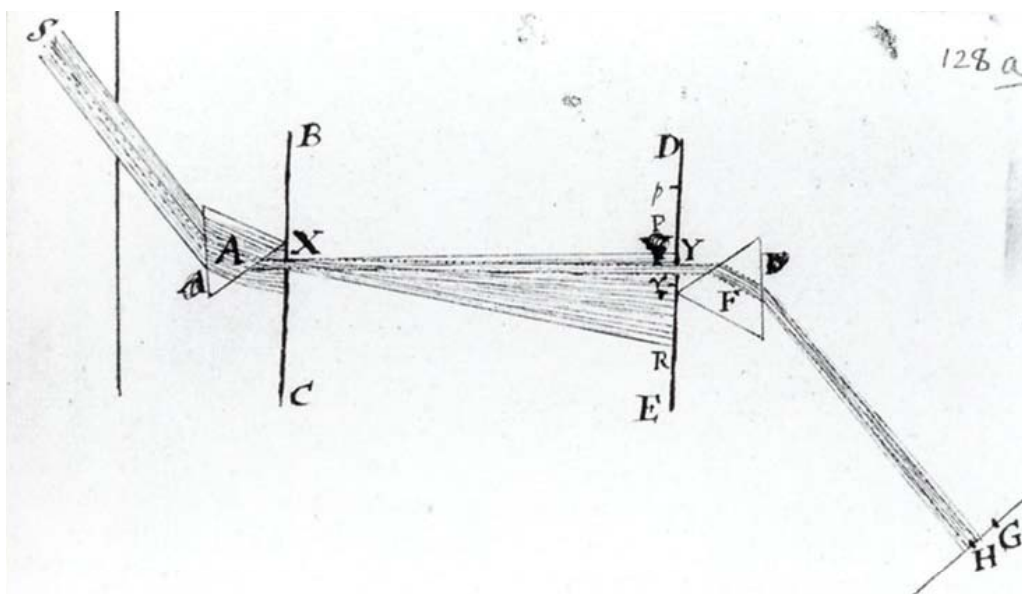

Figure 2.1: The diagram from Sir Isaac Newton's experiment. The first prism (A) splits the white light into its constituent colours. A single colour part of the spectrum hits the second prism (F) proving that a pure colour cannot be divided any more.

Colour is sensation that is dependent on both light and its properties and observer. In order to quantify it physical properties of light and observers have to be known.

2.1 HUMAN VISION

The eye is an organ used for vision. Frontal part on an eye consisting of iris, pupil and lens acts similarly to the camera lens. Iris limits the amount of light going inside the eye thus protecting it from overexposure and damage. Lens focuses the image on the back, inner surface of an eye—retina. Chemical reactions in rods and cones in the retina produce electrical stimuli for the brain.

HUMAN EYE

Rods and cones are photoreceptor cells in the retina responsible for low and high intensity light vision, respectively. Human eye uses photopic vision when lumi-
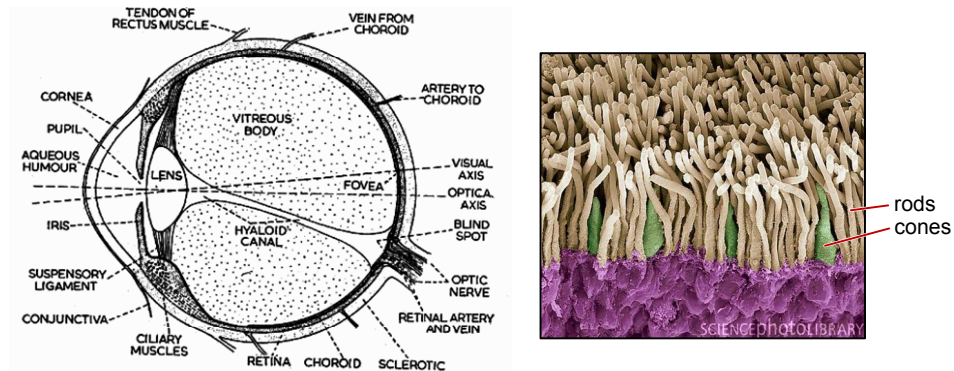
Figure 2.2: Eye cross-section (left) and scanning electron microscope image of human retina (right, source: Science Photo Library, image F001/0041).

nance is above approximately 3 cd/m² and scotopic vision with luminance below approx. 0.03 cd/m². In between, the eye uses mesopic vision, a combination of the above. Rods are sensitive enough to detect a single photon, but they are sensitive only in 400–640 nm wavelength range. Their maximum sensitivity is 1700 lm/W at 507 nm. Because only one type of rod cells exist, under photopic vision regime, there is no colour sensation. Cone cells, on the contrary, are much less sensitive to the light, but their three variants (short, medium and long wavelength) shown in fig. 2.3 allow us to perceive colour through the opponent process of colour vision.

RODS

CONES
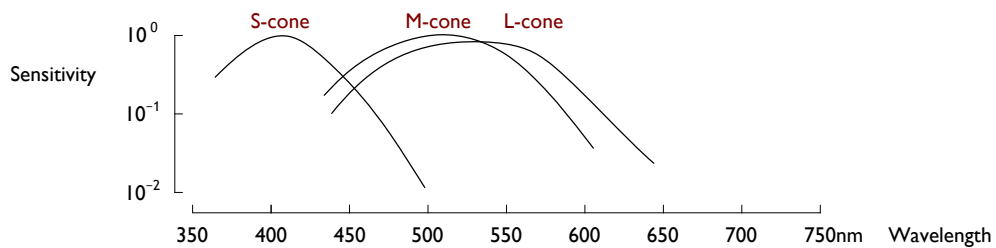
Figure 2.3: Sensitivity of cones after Moses and Hart [45].

The transition between scotopic and photopic vision is a very slow process. The speed depends on the direction of the transition and initial adaptation level. Full adaptation from light to dark conditions may take up to 45 minutes. Reverse transition is faster, but still may take up to few minutes. All calculations in this dissertation assume fully adapted photopic vision regime.

EYE SENSITIVITY

Conversion between radiometric and photometric units is done using the *eye sensitivity function* $V(\lambda)$, also called *luminous efficiency function*, shown in fig. 2.4. The function represents relative eye sensitivity to different wavelengths under photopic vision regime. The maximum eye sensitivity is in green spectral range at 555 nm wavelength. This point corresponds to the sensitivity of 683.002 lm/w. Eye sensi-

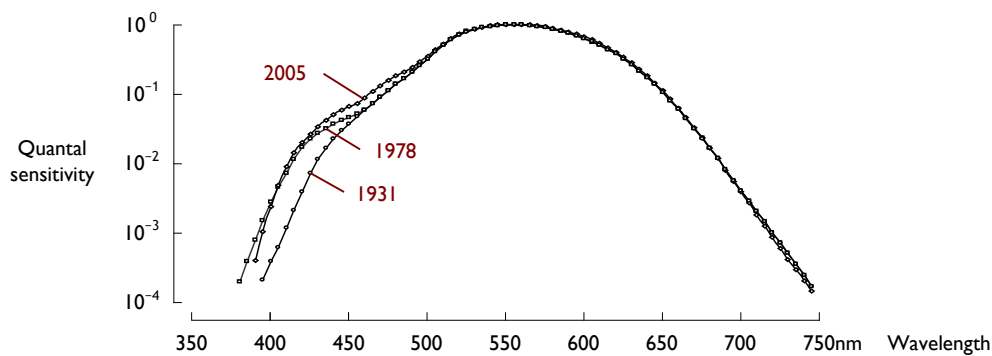Figure 2.4: Eye sensitivity function $V(\lambda)$: 1931 standard, 1978 Vos modification and most recent shape proposed in 2005 by Sharpe, Stockman, Jagla and Jägle.

tivity function was obtained experimentally by the *minimum flicker method*. The stimulus in the experiment was a circular area alternately illuminated by two different colours with 15 Hz frequency. At this frequency the two hues fuse into one colour however the brightnesses does not. By adjusting one light source properties, human subject was to minimise the visible flicker.

There have been several attempts to improve the original 1931 standard function: Judd in 1951, Vos in 1978 [46] and recently, in 2005, Sharpe, Stockman, Jagla and Jägle [47] proposed a modified $V^\star(\lambda)$ function. The blue region of eye sensitivity has been underestimated in the CIE 1931 standard, but this sensitivity function is still commonly used as a basic observer. All measurements and calculations presented in this dissertation will use CIE 1931 standard unless explicitly mentioned otherwise.

2.2 PHOTOMETRIC QUANTITIES

Light can be characterised in two different ways. Radiometric quantities describe physical properties of an electromagnetic wave. Photometric units, on the other hand, characterise light as perceived by human eye. Radiometric measurements are very straightforward, but not useful if one wants to define the sensation that is caused by the light. For example, infra-red and ultra-violet light can be defined in terms of radiometric quantities, but is invisible to the human eye.

Luminous flux is a measure of a perceived power of the light. The unit of luminous flux is *lumen* (lm). A monochromatic light source emitting an radiometric power of 1/683 watt at 555 nm has a luminous flux of 1 lm. LUMINOUS FLUX

Luminous intensity is a measure of a perceived intensity of light per unit solid angle. The unit of luminous intensity is *candela* (cd), which is a base SI unit. The current definition is: a monochromatic light source emitting an optical power of 1/683 W at 555 nm into the solid angle of 1 steradian (sr). In other words, a light LUMINOUS INTENSITY

source with luminous flux of 1 lm emitting into 1 sr has a luminous intensity of 1 cd. An isotropically emitting light source (emitting into 4π sr) with the same luminous flux would have a luminous intensity of $1/4\pi$ cd. The luminous intensity parameter is therefore closely related to light source output geometry. Any lens or other optical aid can greatly influence this parameter.

LUMINANCE   Luminance is a measure of the luminous intensity of light traveling in a given direction per unit area. It describes the amount of light that is emitted from a particular area within a given solid angle. Luminance is typically used to characterise light sources with big emitting surfaces like LCD screens or LEDs with active area greater than 1mm^2.

ILLUMINANCE   The measure of the total luminous flux incident on a given area is called illuminance. A luminous emittance, similarly, is the total luminous flux emitted from a given area. Both are measured in lux (lx) or lumen per square meter (lm/m^2).

The constant $1/683$ is a legacy constant, used to equalise the current definitions of light intensity with the old ones. The "standard candle" (pure spermaceti candle weighing one sixth of a pound and burning at a rate of 120 grains per hour), used as a reference source in England prior to 1948, had roughly $1/683$ watts of power.

2.3   COLOUR SPACES

A colour space is a method of quantifying the sensation of colour. Humans describe the colour sensation by means of brightness, colourfulness and hue. During printing, colour is made by matching cyan, magenta, yellow and black inks (CMYK) on paper. Computer screen or digital photo camera describes the colour by the amounts of red, green and blue. Note that the reds, greens and blues of these devices, are not generally the same. To math the colours of the camera on the screen, a consistent sRGB colour space is used in both devices. Many different colour spaces exist: some are intuitive to use by humans, some are used when working with particular hardware (device dependent). Other may serve particular need, e.g. perceptually uniform colour spaces, but they all describe the colour sensation in a quantitative way.

TRISTIMULUS   Light sources can have a very complex spectral distributions, still a single colour
THEORY OF COLOUR   can be described using only three scalar stimuli parameters. This phenomenon was first postulated in 19th century by Thomas Young and then developed further by Herrman von Helmoltz. The tristimulus theory was experimentally verified in 1930 by the colour matching experiments. The human subjects were to match the colour of a monochromatic light to the light created by mixing three monochromatic lights (primaries). The 1930 experiments used light sources at 700 nm (R), 546.1 nm (G) and 438.1 nm (B). Unfortunately, the colour primaries selection caused some of the colour matching functions' values to be negative. As negative values of light have no physical meaning instead of subtracting one of the tristimulus colours
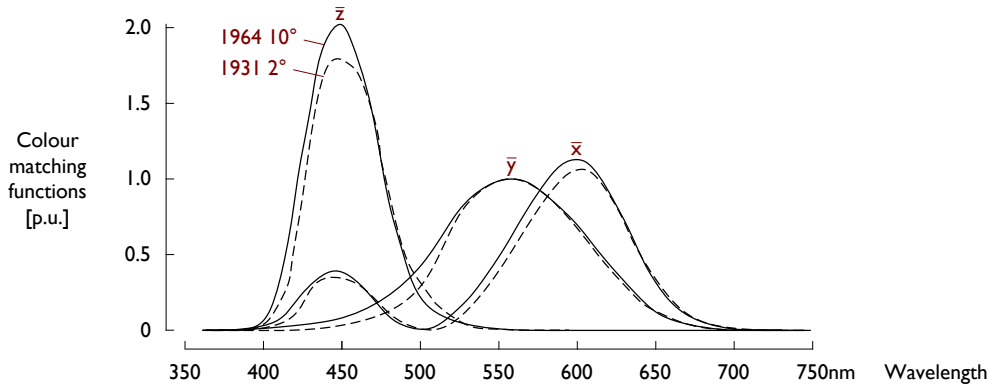
Figure 2.5: CIE 1931 2° and 1964 10° observer $\overline{x}$, $\overline{y}$ and $\overline{z}$ colour matching functions, normalised to the maximum of 1931, 2° observer $\overline{x}$ colour matching function.

from the matching light, the colour was added to the sample monochromatic light.

In 1931 the CIE defined new primaries to overcome the problem with awkward negative weights in colour matching function. New $\overline{x}$, $\overline{y}$ and $\overline{z}$ functions had only positive values and $\overline{y}$ has been chosen to match eye sensitivity function $V(\lambda)$.

Due to the nature of spatial distribution of cones inside the eye, the perception of a colours depends on subject's field of view. To eliminate the influence of this parameter, CIE introduced a 2° standard colorimetric observer. A 10° standard observer has been introduced in 1964 as a result of the work of Stiles and Burch [48] recommended for field of view more than 2°.

In order to calculate tristimulus values X, Y and Z the spectrum of light source needs to be multiplied by respective colour matching functions $\overline{x}$, $\overline{y}$ and $\overline{z}$ and integrated over wavelength.

$$X = \int_{380}^{780} P(\lambda)\overline{x}(\lambda)\mathrm{d}\lambda \qquad Y = \int_{380}^{780} P(\lambda)\overline{y}(\lambda)\mathrm{d}\lambda \qquad Z = \int_{380}^{780} P(\lambda)\overline{z}(\lambda)\mathrm{d}\lambda \qquad (2.1)$$

Because the $\overline{y}$ matches the eye sensitivity function the Y can be used as a measure of luminance of a light. Multiplying all tristimulus values by 683 lm/w gives the values in lumens therefore Y becomes equal to the luminous flux. It is common to describe the colour of the light using CIE xyY colour space. Chromaticity coordinates, that can be represented on 2 dimensional xy-plane (fig. 2.6) are obtained by normalising the tristimulus components.

$$x = \frac{X}{X+Y+Z} \qquad y = \frac{Y}{X+Y+Z} \qquad z = \frac{Z}{X+Y+Z} \qquad (2.2)$$

Because of this normalisation, only two values are needed to represent any possible colour.

$$x + y + z = 1 \qquad \Longrightarrow \qquad z = 1 - x - y \qquad (2.3)$$
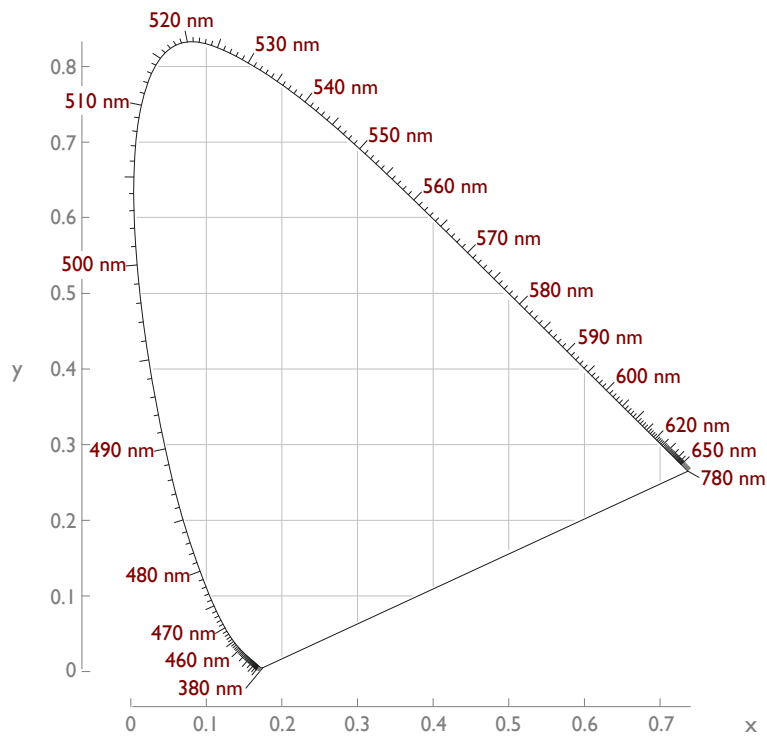
23

Figure 2.6: CIE 1931 *xy* chromaticity diagram.

Intensity of the light is not shown on the *xy*-plane. Any two light sources with the same hues and saturations but different lightness will project on the same point of a diagram. Using *x*, *y* and the stimulus *Y* one can easily calculate back the values of *X* and *Z* stimuli.

$$X = \frac{Y}{y}x \qquad Y = Y \qquad Z = \frac{Y}{y}(1 - x - y) \tag{2.4}$$

When two lights with different spectral power distributions have the same colour chromaticity (same *xy* coordinates) they are called metamers and the property itself METAMERISM is called metamerism. This allows, for example, to mix a white light using blue and yellow (as is in white phosphor converted LEDs) or red, green and blue. This can also lead to big differences between colour rendering of two lights with the same colour chromaticity. For example, white, phosphor based LED does not reproduce well saturated red colours, while white, trichromatic RGB LED can have an excellent red colour rendering.

XY CHROMATICITY   The *xy*-plane is a projection of a linear colour space and therefore colours can
DIAGRAM   be linearly mixed on it. Therefore, every polychromatic source will have a gamut (available colour range) that is a convex hull on all primary colour points inside the horseshoe diagram.
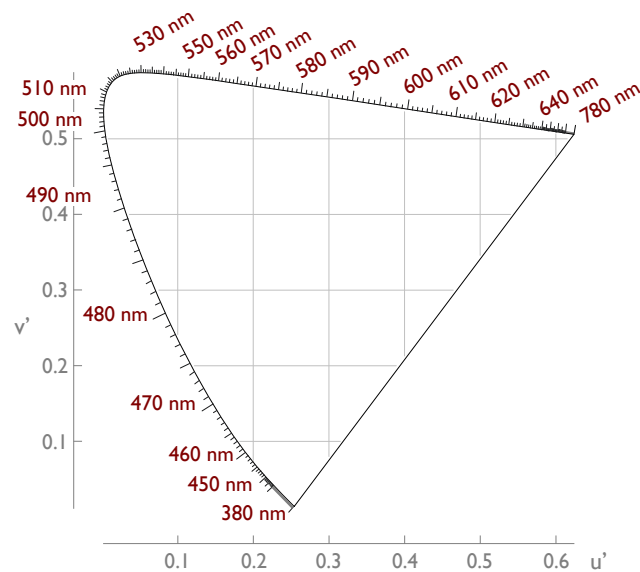
Figure 2.7: CIE 1976 $u'v'$ chromaticity diagram.

Monochromatic light sources (pure colours) lie on the curved boundary of the horseshoe. Straight line between blues and reds is called *purple line*, colours laying on this line cannot be made using a monochromatic light source, they are created by mixing saturated red and blue colours.

Equal energy point or *white point* (x=1/3, y=1/3) corresponds to the white light where all tristimulus values are equal. Any two colours that can be connected by a straight line crossing the white point are called complementary.

This colour space is not perceptually uniform. This means that the difference between colours of two points on the plane does not correspond to the geometrical distance between them. In 1942, MacAdam analysed colour differences of closely spaced points [49]. He noted, that depending on a position in the *xy*-plane, different geometrical distance between two colours yields a noticeable colour difference. Similar colours, that appear identical to human eye, can be grouped on a *xy*-diagram in ellipsis shaped areas (fig. 2.9). Ellipses in the green regions are very big compared to the ellipses in the blue region. This non-uniformity initiated the search for uniform chromaticity diagram. In result, in 1960, the CIE introduced *uv*, and in 1976, $u'v'$ uniform chromaticity diagram [50].

PERCEPTUAL UNIFORMITY

Coordinates for *uv* and $u'v'$ can be calculated from tristimulus values

CIE 1960 *Luv* AND
CIE 1976 $L^*u^*v^*$
COLOUR SPACES

$$u = \frac{4X}{X + 15Y + 3Z} \qquad v = \frac{6Y}{X + 15Y + 3Z} \qquad (2.5)$$

and

$$u' = \frac{4X}{X + 15Y + 3Z} \qquad v' = \frac{9Y}{X + 15Y + 3Z}. \qquad (2.6)$$

These coordinates can also be calculated directly from xy coordinates using equations:

$$u = u' = \frac{4x}{-2x + 12y + 3} \qquad (2.7)$$

and

$$v = \frac{6y}{-2x + 12y + 3} \qquad v' = \frac{9y}{-2x + 12y + 3}. \qquad (2.8)$$

Reverse transformations are also possible, using:

$$x = \frac{3u}{2u - 8v + 4} \qquad y = \frac{2v}{2u - 8v + 4} \qquad (2.9)$$

and

$$x = \frac{9u'}{6u' - 16v' + 12} \qquad y = \frac{2v'}{3u' - 8v + 6}. \qquad (2.10)$$

COLOUR SPACE CONVERSIONS A conversions from one colour space to another requires a choice of a different set of primary stimuli. The only limitation is that the vectors created by the new set of stimuli $R'G'B'$ is linearly independent. Therefore no combination of r, g and b should make

$$rR' + gG' + bB' = 0, \qquad (2.11)$$

except for trivial $r = g = b = 0$. Each primary stimulus of the new set can be matched using the mixture of the old primaries therefore we can write relation between RGB and $R'G'B'$ colour space as:

$$\begin{aligned}
R' &= a_{11}R + a_{12}G + a_{13}B \\
G' &= a_{21}R + a_{22}G + a_{23}B \\
B' &= a_{31}R + a_{32}G + a_{33}B
\end{aligned} \qquad (2.12)$$

A transformation matrix A is formed by the transformation coefficients a_{ij}

$$A = \begin{bmatrix} a_{11} & a_{12} & a_{13} \\ a_{21} & a_{22} & a_{23} \\ a_{31} & a_{32} & a_{33} \end{bmatrix}. \qquad (2.13)$$

Transition from $R'G'B'$ to RGB based colour space requires inverted matrix A^{-1}.

2.4 BLACK BODY RADIATION

BLACK BODY DEFINITION A black body is an idealised physical object that absorbs all electromagnetic radiation that falls on it. The ideal object would appear perfectly black because all the visible light is absorbed. Any light emitted from the object would only be the function of object's temperature.
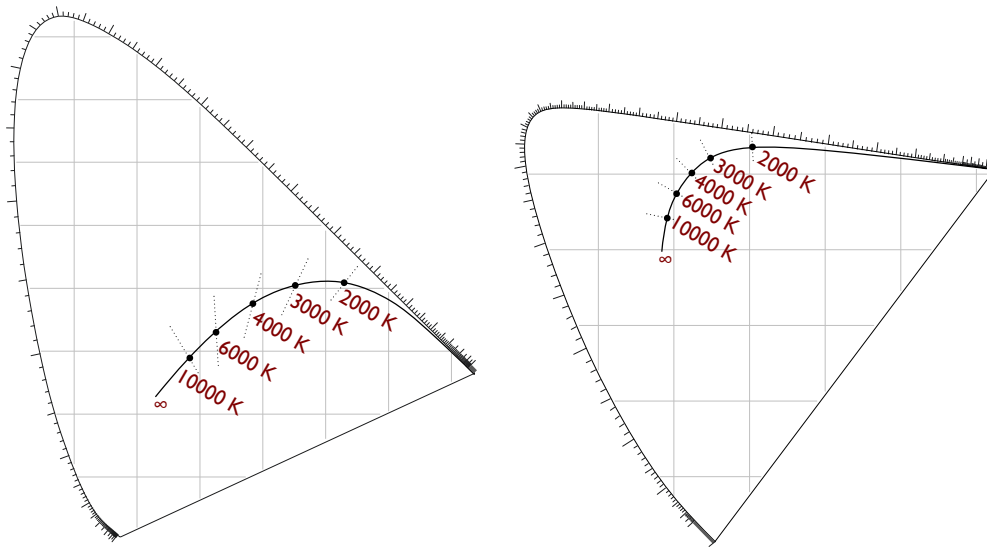
Figure 2.8: Black body colour locus on CIE 1931 *xy* (left) and CIE 1976 *u′v′* (right) diagram. Dotted lines show the position of correlated colour temperature points. Note that CCT lines on *u′v′* diagram are perpendicular to black body locus.

A planckian black body radiation spectrum is a very useful standard for defining white light. It is characterised using only single variable: *colour temperature*. The spectrum is given by equation

$$I(\lambda) = \frac{2hc^2}{\lambda^5 \left[\exp\left(\frac{hc}{\lambda kT} \right) - 1 \right]} \tag{2.14}$$

PLANCKIAN RADIATION SPECTRUM

derived by Max Planck in 1900. The ideal black body object heated up to 6500 K would emit white light with colour temperature of 6500 K. An incandescent light bulb is an example of non ideal black body source. The temperature of the filament has to be kept below melting point and therefore the maximum colour temperature of this kind of light source is around 3500 K. Low luminous efficacy of the classical light bulb approximately 15 lm/w is the effect of the black-body spectrum having its maximum in the infrared part of electromagnetic radiation.

The colour point locus of black body radiator starts in the red corner of CIE 1931 diagram, then moves through the orange and yellow to end in the white region. This corresponds to the colours of a real heated objects. Colour temperatures between 2000 K and 4000 K are commonly referred to as warm white. Colour temperatures above 7000 K are called cool white.

BLACK BODY LOCUS

If the colour coordinates of a light source is not on the black-body locus but in its proximity then the *correlated colour temperature* parameter is used. It is defined as temperature of a black body whose colour is the closest to the source colour.

On a $u'v'$ diagram, the CCT can be determined as a colour temperature of a closest geometrically point on a planckian curve. Correlated colour temperature cannot be determined geometrically on a xy plane, because the plane is non-uniform.

To calculate chromaticity coordinates an cubic interpolation can be used [51]. The x coordinate is calculated for 1666–4000 K and 4000–25000 K temperature ranges respectively as:

$$x = -0.2661239 \cdot 10^9/T^3 - 0.2343580 \cdot 10^6/T^2 + 0.8776956 \cdot 10^3/T + 0.179910$$
$$x = -3.0258469 \cdot 10^9/T^3 + 2.1070379 \cdot 10^6/T^2 + 0.2226347 \cdot 10^3/T + 0.24039$$
$$(2.15)$$

The corresponding y coordinate is calculated for 1666–2222 K, 2222–4000 K and 4000–25000 K temperature ranges respectively as:

$$y = -1.1063814x^3 - 1.34811020x^2 + 2.18555832x - 0.20219683$$
$$y = -0.9549476x^3 - 1.37418593x^2 + 2.09137015x - 0.16748867 \qquad (2.16)$$
$$y = +3.0817580x^3 - 5.87338670x^2 + 3.75112997x - 0.37001483$$

2.5 STANDARD ILLUMINANTS

CIE has standardized several light illuminants: A, B, C, D series, E and F series. Examples of their chromaticities and colour temperatures can be seen in table 2.1. The purpose of standardizing the illuminants is to be able to compare the colour sensation of various objects under typical light sources. The sources include the sun spectra at different times of a day, the direct sunlight, the average incandescent bulb and fluorescent lamps of various composition.

Table 2.1: Selection of standard illuminants introduced by the CIE.

ILLUMINANT	CT/CCT [K]	x	y	DESCRIPTION
A	2856	0.4476	0.4074	incandescent source
B	4874	0.3484	0.3516	direct sunlight at noon
C	6774	0.3101	0.3162	north sky daylight
D$_{65}$	6500	0.3127	0.3290	noon daylight
E	5455	0.3333	0.3333	equal energy

Illuminants from D series were introduced in 1967 to replace the B and C illuminants acting as daylight simulators [52]. Judd et al. analyzed typical daylight spectra and tabulated the results with 10 nm increments. Obtaining higher resolution requires interpolating this data. The D series illuminants are used in calculation of the colour rendering index—the measure of the quality of light.

Although many light sources with different spectra can have the same perceived colour, the appearance of various colour objects under those illuminants can vary significantly.

In order to easily compare the ability to reproduce colours a CRI (colour rendering index) has been developed [53]. Colour rendering is defined as a *measure of the degree of colour shift objects undergo when illuminated by the light source as compared with the colour those same objects when illuminated by a reference source of comparable colour temperature*. This means we compare a test light source to natural light or an ideal source e.g. black-body radiator with the same colour temperature as the test source. COLOUR RENDERING INDEX

A high CRI can be achieved by a broadband spectrum emitters e.g. tungsten halogen lamps (CRI ≈ 100) which has a spectrum comparable to daylight, but its efficacy is only around 25 lm/w. On contrary, the low pressure sodium lamp (CRI ≈ 25) can reach up to 200 lm/w, but they emit only two spectral lines at 589.0 nm and 589.6 nm. Therefore every object illuminated with this lamp will be either yellow either grey or black.

Calculation of CRI starts with defining CCT of a test source. For CCT < 5000 K a black-body radiator with the same temperature is used. Illuminant D is used for sources with CCT ≥ 5000 K. The colour differences ΔE_i on CIE 1964 $u^*v^*w^*$ colour space of 14 selected Munsell samples (see table 2.2) is measured or calculated when illuminated with test source and reference source CRI CALCULATION

$$\Delta E_i = \sqrt{(u^*_{ref} - u^*_{test})^2 + (v^*_{ref} - v^*_{test})^2 + (w^*_{ref} - w^*_{test})^2}. \qquad (2.17)$$

For each colour sample (tab. 2.2) a particular CRI (R_i) can be calculated using

$$R_i = 100 - 4.6\Delta E_i \qquad (i = 1, \ldots, 14). \qquad (2.18)$$

A general CRI R_a is the arithmetic mean of the particular R_i.

Although CRI is widely used for calculating colour quality of light sources, it is known to have some drawbacks [54, 55]. For example only medium saturated colours are taken into account when calculating the colour rendering index, particularly R_9 (saturated red) can be very low while overall CRI can still be quite high. Sometimes a high CRI lamp e.g. 2000 K black-body ($R_a = 100$), can have very poor colour rendering due to its very reddish light. This is also true for lamps with very high values of CCT. White light with slight colour tint to green or purple (laying above or below planckian locus, respectively) can have a very high CRI index but are unacceptable for general lighting purposes. CRI is now being depreciated in favour of measurements based on colour appearance models e.g. CIECAM02 [56]. Commission Internationale de l´Eclairage recommended the development of new COMMENTS ON CRI

colour rendering index that would supplement the current CRI [57]. Freyssinier and Rea proposed a two metric system that would combine the present CRI value with gamut area index forming a two-metric solution [58].

Table 2.2: Test colour samples for CRI calculation. Last seven samples provide supplementary information about colour rendering of strong colours and known objects.

NAME	MUNSELL NOTATION	APPEARANCE UNDER DAYLIGHT
TCS01	7.5 R 6/4	Light grayish red
TCS02	5 Y 6/4	Dark grayish yellow
TCS03	5 GY 6/8	Strong yellow green
TCS04	2.5 G 6/6	Moderate yellowish green
TCS05	10 BG 6/4	Light bluish green
TCS06	5 PB 6/8	Light blue
TCS07	2.5 P 6/8	Light violet
TCS08	10 P 6/8	Light reddish purple
TCS09	4.5 R 4/13	Strong red
TCS10	5 Y 8/10	Strong yellow
TCS11	4.5 G 5/8	Strong green
TCS12	3 PB 3/11	Strong blue
TCS13	5 YR 8/4	Light yellowish pink (skin)
TCS14	5 GY 4/4	Moderate olive green (leaf)
TCS15	1 YR 6/4	Asian skin

2.7 COLOUR DISTANCE

MacAdam's research on the ability of the human eye to notice the difference in chromaticities of two light sources started the search for uniform colour space where the perceived colour difference can be measured geometrically on the colour plane.

CIE defines colour difference as an Euclidean distance between two colour points in a CIE 1976 $L^*a^*b^*$ colour space

$$\Delta E^*_{ab} = \sqrt{(L^*_{ref} - L^*_{test})^2 + (a^*_{ref} - a^*_{test})^2 + (b^*_{ref} - b^*_{test})^2}. \tag{2.19}$$

JUST NOTICEABLE DIFFERENCE A ΔE^*_{ab} value of 2.15 corresponds to just noticeable difference between two colour points [59]. Colour distance between the colour command and generated colour is a good measure of the colour control loop accuracy.

Some previous work use CIE 1976 colour space to define the colour distance.

$$\Delta u'v' = \sqrt{(u'_{ref} - u'_{test})^2 + (v'_{ref} - v'_{test})^2}. \tag{2.20}$$

Equation does not take into account the difference in light intensity therefore it is only a measure of chromaticity difference. Colour distance equal to 0.0035 is a just noticeable difference between two colour points [50].
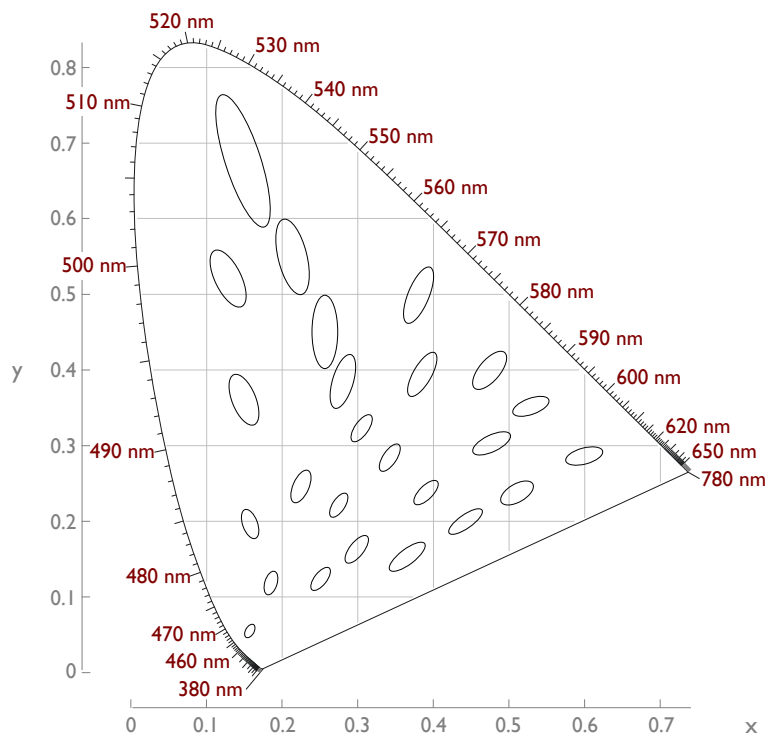
Figure 2.9: MacAdam ellipses on CIE 1931 *xy* chromaticity diagram. Ellipses magnified 10×. A light source with colour coordinates laying inside the ellipse is indistinguishable frmm a light source with the coordinates in the centre of the ellipse. As seen from the various sizes of the ellipses the CIE 1931 colour space is not perceptually uniform.

3 Light-emitting diodes

A Note on Carborundum.

To the Editors of Electrical World:

SIRS:—During an investigation of the unsymmetrical passage of current through a contact of carborundum and other substances a curious phenomenon was noted. On applying a potential of 10 volts between two points on a crystal of carborundum, the crystal gave out a yellowish light. Only one or two specimens could be found which gave a bright glow on such a low voltage, but with 110 volts a large number could be found to glow. In some crystals only edges gave the light and others gave instead of a yellow light green, orange or blue. In all cases tested the glow appears to come from the negative pole. a bright blue-green spark appearing at the positive pole. In a single crystal, if contact is made near the center with the negative pole, and the positive pole is put in contact at any other place, only one section of the crystal will glow and that the same section wherever the positive pole is placed.

There seems to be some connection between the above effect and the e.m.f. produced by a junction of carborundum and another conductor when heated by a direct or alternating current; but the connection may be only secondary as an obvious explanation of the e.m.f. effect is the thermoelectric one. The writer would be glad of references to any published account of an investigation of this or any allied phenomena.

NEW YORK, N. Y.   H. J. ROUND.

LED is a solid-state device that emits light by means of electroluminescence. First observations of light emission from SiC (carborundum) crystals were made in 1907 by Henry Joseph Round. The first observed LED was a Schottky diode. The light was produced on metal-semiconductor junction. Under normal, forward bias conditions, the current flowing through the Schottky diode consists only of majority carriers. The minority carriers can be injected under strong forward bias conditions (or through avalanche effect) thus making the light emission possible.

In semiconductor materials, valence and conduction energy bands do not overlap. The energy difference between the highest point in the valence band and the lowest point in conduction band is called a bandgap. The energy levels in the bandgap are forbidden for the electrons. Transition between two bands is possible only when electron has enough surplus energy or looses enough energy—the minimal amount of energy for transition equals the bandgap energy. In direct bandgap semiconductors, the electrons from the conduction band minima recombine with holes at the valence band maxima with preservation of momentum. Contrary, in indirect bandgap semiconductors, the respective extrema of conduction and valence bands do not have the same value of quantum-mechanical wave vector. Electrons have very little momentum (in the range of $2\pi/a$, where a is lattice constant) therefore every transition is almost vertical. Emission of a *phonon*, a quantised mode of vibration of a crystal lattice with $2\pi/\lambda$ wave vector, is essential to preserve the momentum [60]). This transition is less likely to happen than direct transition. Moreover, the temperature in the active area increases, therefore the indirect bandgap semiconductors, like silicon, are very inefficient at generating light.
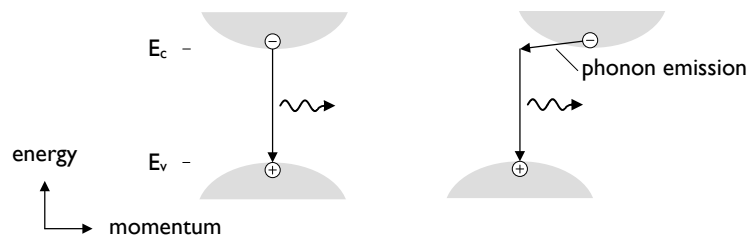

Figure 3.1: Photon generation in direct (left) and indirect (right) bandgap semiconductors. In indirect bandgap semiconductors, emission of phonon must assist the radiative recombination in order to preserve the momentum [61].

3.2 RECOMBINATION

A pair of excess carriers—free electron and hole—can recombine producing a photon. This process is called *radiative recombination*. However, the recombination can also occur in a non-radiative way where no light is generated. The result of radiative recombination is the transition of an electron from higher energy state to lower energy state with emission of radiative energy. In a non-radiative recombination process, the excess energy from electron transition is converted into thermal energy in form of crystal lattice vibrations. Maximising the radiative and minimising the non-radiative processes are the goal for maximising the efficiency of LEDs.

In light emitting diodes almost all of the radiative recombination rate is contributed by the bimolecular recombination rate [61]. The net recombination rate is given by

$$R_{net} = Bnp - Bn_0p_0 \tag{3.1}$$

where B is a bimolecular recombination coefficient, n and p are electron and hole concentrations and n_0 and p_0 are electron and hole concentration under equilibrium conditions.

Under high excess carrier density, when $N \gg n_0, p_0$ ($N = n - n_0, p - p_0$) the radiative recombination rate can be expressed as
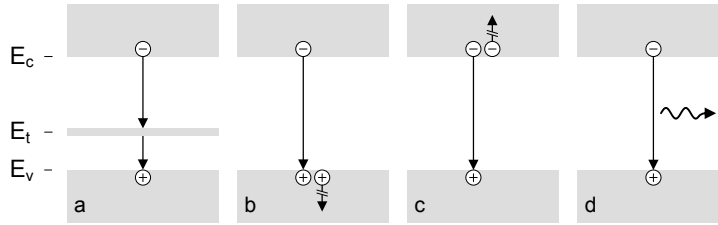
$$R = BN^2. \tag{3.2}$$

Figure 3.2: Band diagram showing possible recombinations mechanisms: deep level Shockley-Read-Hall (a), Auger (b,c), Bimolecular (d) band to band radiative [61].

With the presence of e.g. a defect of the crystal lattice a non-radiative recombination can occur (fig. 3.2a). These defects act as a very efficient non-radiative recombination centres, especially if the energy level is located close to the middle of the bandgap [62]. An electron or hole is trapped in a forbidden region of an energy band by a defect in crystal lattice. These defects can be either unintentionally introduced or engineered to produce a, so called, deep-level LED.

The statistics of the process were described by Shockley and Read and, independently, by Hall. Net recombination rate is described by

$$R_{net} = \frac{np - n_i^2}{\tau_p(n + n_1) + \tau_n(p + p_1)}. \tag{3.3}$$

In doped semiconductors, equation 3.3 simplifies to

$$R_{net} \approx \frac{n - n_0}{\tau_n} \text{ for } p \gg n \tag{3.4}$$

$$R_{net} \approx \frac{p - p_0}{\tau_p} \text{ for } n \gg p \tag{3.5}$$

there τ_n and τ_p are recombination lifetimes of electrons and holes, respectively. It can be seen that recombination rate becomes proportional to the excess carrier density

$$R = AN. \tag{3.6}$$

During Auger transition (fig. 3.2b and c), the energy created in a recombination process between an electron and a hole is transferred to third carrier. No light is generated and the surplus energy pushes either the second electron higher in conduction band or the second hole downward in valence band. The energy passed on to the third carrier is then dissipated by emission of phonons. The process requires three carriers to be in the same place during recombination therefore the recombination rate is proportional to the third power of carrier density

$$R_A = CN^3, \tag{3.7}$$

where C is the *Auger coefficient*.

Auger recombination mechanism has been proposed as one of the possible reasons for efficiency droop under high current injection in InGaN structures [63]. Although the efficiency droop is similar to Auger recombination, some argue [64, 65] that the numerical values of Auger coefficient are not high enough for this process to dominate i the total power losses and other loss mechanism like electron current leakage and non uniform hole distribution may be responsible.

Taking into account equation 3.3, 3.6 and 3.7 we can write the stationary balance equation for LEDs as

$$j/e = AN + BN^2 + CN^3 + DN^m \tag{3.8}$$

where j is the injected current density, e is the elementary charge, N is 2D excess carrier density in the active area and coefficients A, B, C and D are describing non-radiative Shockley-Read-Hall recombination, bimolecular radiative process, Auger recombination and other non-radiative processes respectively. It is beneficial to supply LEDs with a current level, at which the bimolecular radiative process dominates.

3.3 MATERIALS

Nowadays, elemental semiconductors for solid-state lighting (LEDs and laser diodes) are the III-V compounds (Al, Ga and In can be found in group III of periodic table, N and P in group V). In order to create a light generating structure a heteroepitaxy growth technology is used.

AlGaInP The compound crystal is grown on a substrate. The $(Al_xGa_{1-x})_{1-y}In_yP$ is lattice matched to GaAs (lattice constant 5.65 Å) for $y = 0.48$. The semiconductor has a

direct bandgap for emission wavelength higher than 555 nm therefore it is used to create red, orange, amber and yellow LEDs [66].

$In_xGa_{1-x}N$ nitrides lack a native bulk substrate. InGaN high power structures INGAN are typically grown on lattice mismatched sapphire (lattice constant 2.75 Å, 15 % mismatch) or SiC substrates (lattice constant 3.08 Å, 3.5 % mismatch) [67].

Lattice mismatch between compound and grown crystal yields in very high dislocation densities which act as non-radiative, deep-level recombination centres. Theses centres contribute to decreased optical output [68]. The III-V phosphide materials used for red, orange, amber and yellow diodes are strongly affected by the crystal defects. The III-V nitride compounds are less affected by the crystal defects due to carrier localisation that prevents from non-radiative recombination. Therefore it is possible to create high power blue LED even with high number of dislocations present in a diode.

3.4 STRUCTURES

Three levels of LED structure will be discussed. Starting from the active region that generates light in chapter 3.4.1, through the LED chip that is responsible for supplying the active region with free carriers and extracting the generated light in chapter 3.4.2 to the highest level structure of LED packaging in chapter 3.4.3.

3.4.1 *Active region*

Homojunction is a basic structure for all diodes. A connection between two differ- HOMOJUNCTION ently doped semiconductors with the same bandgap forms a p-n junction. Under forward bias, free carriers from both semiconductors are forced into the regions of opposite conductivity type.
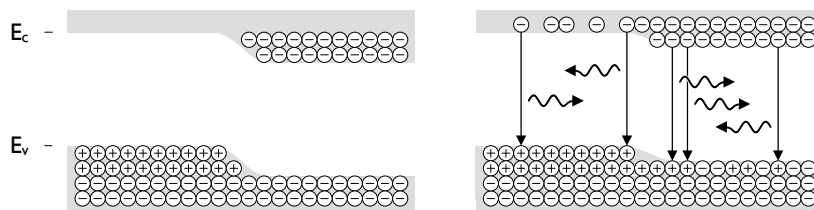

Figure 3.3: Band diagram showing p-n junction under no bias (left) and forward bias (right) conditions. Under forward bias, the recombination occurs in the area around the junction defined by diffusion lengths.

Diffusion lengths (L_n and L_p) of minority carriers depends on carrier mobility.

$$L_n = \sqrt{D_n\tau_n}, \qquad L_p = \sqrt{D_p\tau_p}, \qquad (3.9)$$

where τ_n and τ_p are electron and hole minority carrier lifetimes. D_n and D_p are the diffusion constants

$$D_n = \frac{kT}{e}\mu_n, \qquad D_p = \frac{kT}{e}\mu_p \qquad (3.10)$$

where μ_n and μ_n are electron and hole mobility dependent on the semiconductor.

Free carriers recombine radiatively around the junction area within the diffusion distance. As recombination rate is given by the bimolecular recombination equation $R = Bnp$, where n and p are the electron and hole carrier concentrations and B is bimolecular recombination coefficient. The light generation is limited in this structure by the low excess carrier density. The width of the p region is critical for obtaining higher efficiencies. When the region is too shallow, the electrons can escape and recombine non-radiatively through crystal defects. Too thick region will easily reabsorb emitted photons thus reducing the overall efficiency. A heterojunction can be used to overcome both this problems at the same time.

DOUBLE HETEROSTRUCTURE
    A third semiconductor is added between two, differently doped, semiconductors to form a confinement area for free carriers. This third semiconductor has lower bandgap than surrounding materials. As a result, the excess carriers get trapped between two barriers. Width of this barrier can be controlled during manufacturing process. Barrier width is much lower than diffusion lengths in the particular semiconductor therefore free carriers are confined in much smaller area as compared to homojunction structure. Increased carrier densities yield in highly increased light generation.
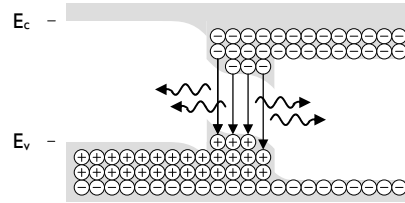

Figure 3.4: Band diagram showing double heterostructure under forward bias conditions. Free carriers are confined between two barriers.

Free carriers are distributed within active region with Fermi-Dirac distribution. Therefore carriers with energy levels higher than barrier height can escape from the confinement area. Concentration of these carriers can be calculated as

$$n_B = \int_{E_B}^{\infty} \rho_{dos} f_{FD} \mathrm{d}E \qquad (3.11)$$

where ρ_{dos} is the density of states, f_{FD} is the Fermi-Dirac distribution and E_B is the height of the heterojunction barrier. This leakage contributes to decreased ef-
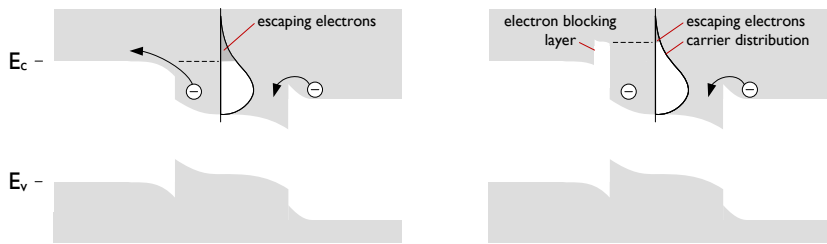
Figure 3.5: Band diagram showing double heterostructure without (left) and with (right) electron blocking layer. Additional layer prevents the electrons escaping from the active region, decreasing the leakage current thus increasing the diode efficiency [68].

ficiency, especially at high temperatures. An electron blocking layer can be introduced into the structure to help confine free carriers.

Bigger width of an active area width than in quantum well structures makes the carrier density lower and therefore decreases the impact of Auger recombination on diode efficiency at higher currents.

QUANTUM WELL STRUCTURES

When additional, thin (in the range of tens of angstroms) layer of semiconductor with smaller bandgap than the cladding layers is added a quantum well is formed. A quantum well structure confines the excess carriers to a very narrow area in order to increase the carrier concentration and therefore increase the recombination rate. Narrow width of the active area also reduces the self absorption effects in some LED structures [69].

ALLOWED ENERGY LEVELS

When the thickness of the well is close to the de Broglie wavelength, the quantum effects appear. Solving the Schrödinger equation for a finite potential well produces the allowed energy levels values within the quantum well. The energy states are finite and are dependent on the well width. Therefore by varying the width of the well one can change the colour of an LED.

SATURATION EFFECT

One of the implication of using quantum wells is that they have limited capacity and, at high current injection, a carrier overflow may occur. When carrier concentration in the active area reaches certain level the Fermi energy rises above the top of quantum well. The carrier overflow the structure and further increase of carrier density in the active area is impossible. The light output becomes saturated. In order to overcome this problem multiple quantum well structures are used [68] as shown in figure 3.5.

MQW STRUCTURES

Carrier density on each of available energy states depends on the injection current density. At low values mostly the lowest energy states are occupied by electrons in conduction band well and the highest states in valence band.
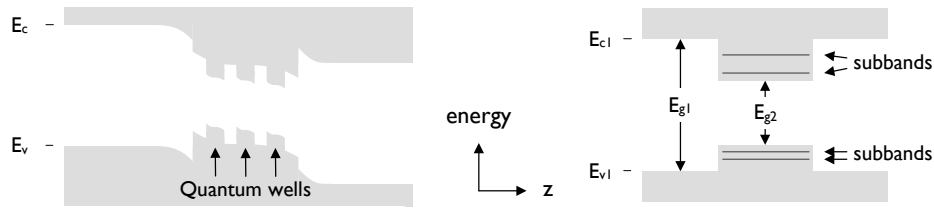
Figure 3.6: Band diagram showing multiple quantum wells structure under forward bias conditions (left) and details of single quantum well (right). A thick semiconductor layer with energy gap E_{g2} is surrounded by a semiconductor with a higher bandgap E_{g2} forming a quantum well. Allowable carrier energy values, subbands, shown inside the potential well [68].

3.4.2 LED *chip*

Due to low efficiency of homojunction structure, high power LEDs use either double heterostructure or MQW structures for active regions. These active structures are embedded in a LED chip, whose task is to supply active region with free carriers, extract the generated light as efficiently as possible.
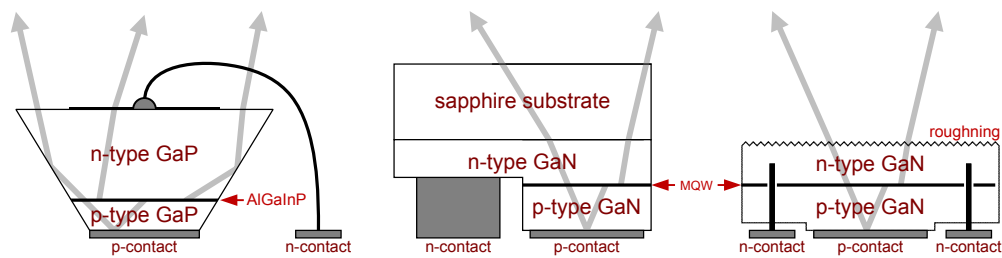

Figure 3.7: Common structures of high power LEDs: truncated-inverted pyramid (left) for phosphide diodes [70], flip-chip (middle) gallium nitride structure [71] and thin-film flip-chip (right) GaN structure [72].

Supplying the current to the active region is done utilising metallic contacts and conductive layers of semiconductors acting as current spreading layers.

LIGHT EXTRACTION   Light extraction is a very difficult task as the LED chips are built using materials with high refractive index causing total internal reflection phenomenon trapping the light inside the chip. Generated photons can be reabsorbed by the active area or by metallic contacts therefore they should be extracted from the chip as fast as possible. Special geometric shapes (fig. 3.7) of the LED chip as well as micro patterning of edges allow the light to escape the structure [44]. Bottom contacts are made reflective to maximise the light output. For example, the thin-film flip-chip structure is made by growing the GaN structure on a sapphire substrate, flipping it and chemically removing the transparent substrate for increased optical transmittance.

The revealed n-type GaN lager is then roughened through photochemical etching to increase light extraction [72, 68].

3.4.3   Packaging

LED packages very often include a lens that shape the light beam. The lens and plastic body of the diode is not thermally conductive, therefore the packaging must provide good thermal contact between LED chip and mounting surface. Some LED chips must be electrically isolated from the heatsink. This provides a big challenge as good electrical isolators are typically also good thermal isolators.

3.5   ELECTRICAL CHARACTERISTICS

Light in the LED structures is created by electroluminescence—this means that the energy created during electron-hole recombination is directly converted to photons. Therefore forward voltage of an LED must be at least equal to the bandgap energy in the active region divided by the elementary charge.

$$V_f \geq \frac{h\nu}{e} \approx \frac{E_g}{e} \tag{3.12}$$

The value of forward voltage can be increased by few phenomena. The series resistance will increase the diode drive voltage linearly with the current. Total diode series resistance is a sum of contact resistance, resistance caused by abrupt band structure and bulk resistance of LED materials. Additionally, carriers injected into quantum well loose some energy because discrete energy levels inside the well will be always smaller than the cladding layer energy. Therefore difference between free carrier energy in confinement layer and inside a well has to be dissipated by a phonon emission. The forward voltage of an LED can be expressed as

$$V_f = \frac{E_g}{e} + IR_s + \frac{\Delta E_C - E_0}{e} + \frac{\Delta E_V - E_0}{e} \tag{3.13}$$

where $\Delta E_C - E_0$ and $\Delta E_V - E_0$ represent differences in energy levels between quantum well and conduction and valence confinement layers, respectively [69]. Electrical characteristics of a p-n junction are described by Shockley equation [61]   SHOCKLEY EQUATION

$$I = I_S\big(\exp(V/nV_T) - 1\big) \tag{3.14}$$

where I and V are diodes current and voltage respectively and n is the ideality factor. I_S and V_T are the reverse bias saturation current and thermal voltage described by

$$I_S = eA\left(\sqrt{\frac{D_p}{\tau_p}} \cdot \frac{n_i^2}{N_D} + \sqrt{\frac{D_n}{\tau_n}} \cdot \frac{n_i^2}{N_A}\right), \qquad V_T = \frac{kT}{e}. \tag{3.15}$$
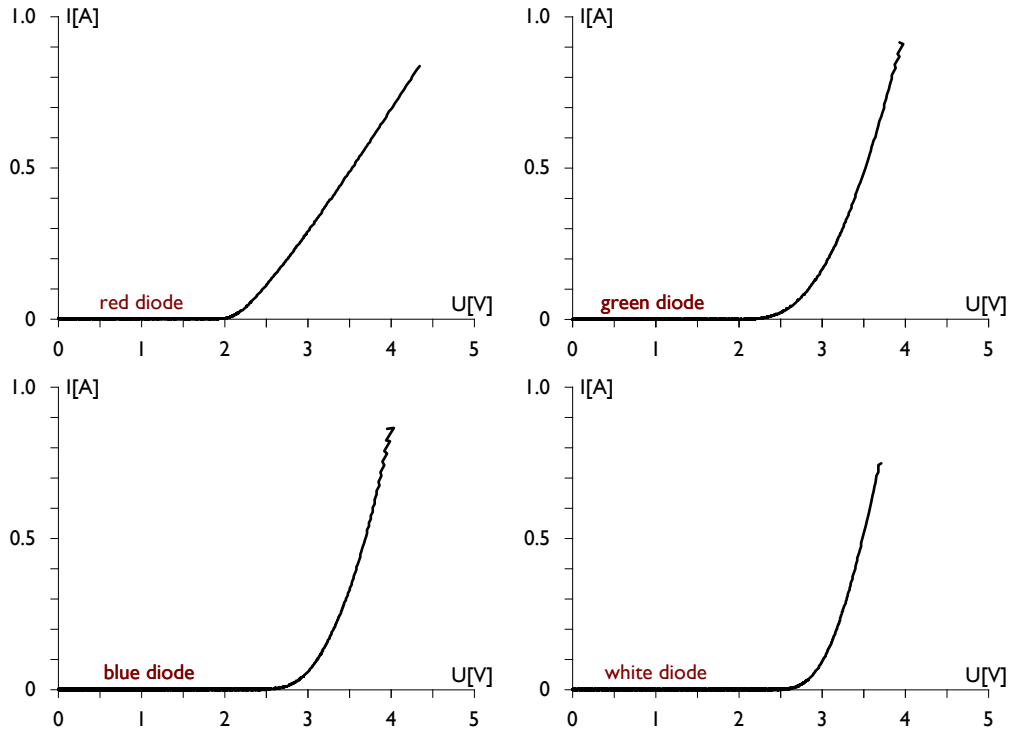
Figure 3.8: Measured current-voltage characteristics of red, green, blue and white Luxeon K2 diodes at 20°C.

Including parasitic series resistance and assuming forward-bias conditions, when $V \gg kT/e$ the IV characteristics can be rewritten as

$$I = I_S\Big(\exp\big(e(V - IR_s)/nkT\big)\Big). \tag{3.16}$$

Schockley's equations does not include the presence of quantum well(s) in the diode structure and tunneling injection. Despite this, it is a common practice to fit measurement data to Shockley equation even though it does not reflect all physical phenomena in the diode [73].

In order to compare the theoretical electrical model for a single p-n junction with structures used in high intensity light-emitting diodes available on the market the characteristics of basic red, green, blue and white colour diodes were measured using equipment described in chapter 1.4.1. Diodes were placed on a thermally controlled cold plate and charged capacitor was connected to their terminals. The capacitor was discharged through the diode providing short, low energy pulse (thus minimising the heating of the junction).

Figure 3.8 shows the current-voltage characteristics of four high power Luxeon K2 diodes. The data was fitted to theoretical model described by equation 3.16.

Identified values of ideality factor and series resistance are gathered in table 3.1. Expected values of ideality factor are in the 1–2 range. However, measured values of the ideality factor are much higher, in the range of 3–7. This is attributed to tunneling injection.

Table 3.1: Measured values of ideality factor and series resistance of Luxeon K2 diodes.

DIODE	n	R_s
LXK2-PD12-R00 (red)	3.166	2.334 Ω
LXK2-PM14-U00 (green)	7.349	0.898 Ω
LXK2-PB12-K00 (blue)	6.014	0.775 Ω
LXK2-PW12-U00 (white)	4.563	0.718 Ω

3.6 OPTICAL CHARACTERISTICS

Typical emission spectra of AlGaInP and InGaN diodes are shown in figures 3.9 and 3.10. Green gallium nitride diodes have the widest emission spectra due to high fluctuations of chemical composition in indium rich semiconductor [74].
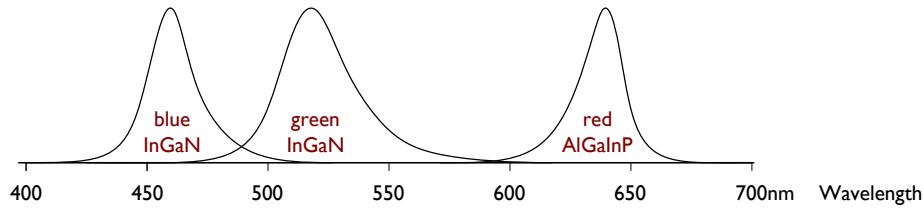

Figure 3.9: Measured emission spectra of red AlGaInP and green and blue InGaN diodes with normalised intensities. FWHM is equal to 20, 33 and 21.3 nm for red green and blue diode respectively.
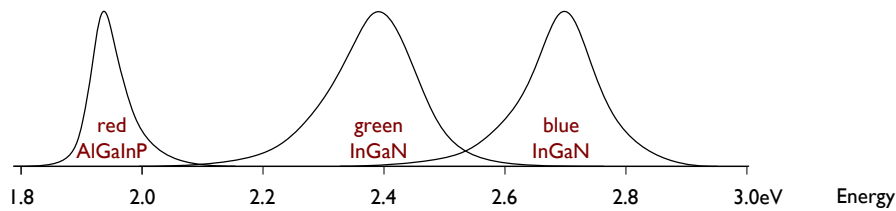

Figure 3.10: LED emission spectra (fig. 3.9) shown in energy scale. FWHM is equal to 2.41, 6.00 and 4.93 kT for red green and blue diode respectively. Theoretical FWHM value for LEDs is equal to 1.8 kT.

Theoretical emission spectrum of a bulk semiconductor LED is a product of the density of states and the distribution of carriers in the allowed bands characterised by a Boltzmann distribution [68].

$$I(E) = \rho(E) \cdot f_B(E) \propto \sqrt{E - E_g} \cdot e^{-E/kT} \tag{3.17}$$

This equation is to be used with care for InGaN diodes, since Boltzmann distribution is not applicable to localised carriers.
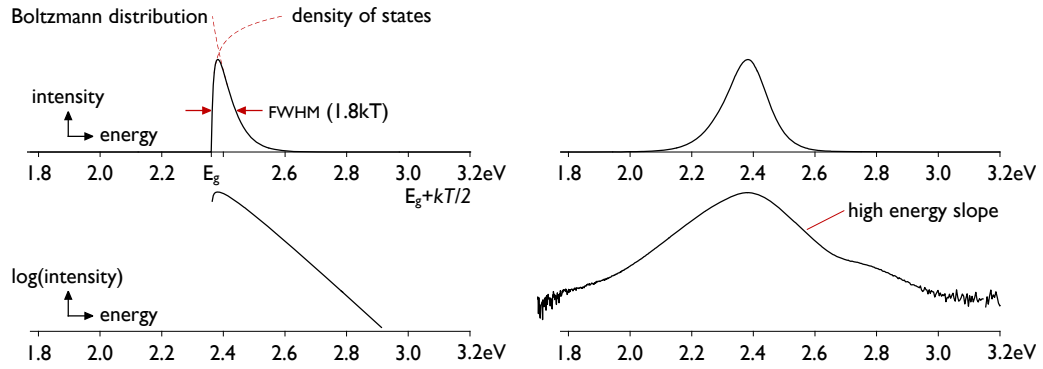

Figure 3.11: Theoretical emission spectrum as a product of Boltzmann distribution and the density of states [68] (left) and measured spectrum of a green LED (right), both plotted in linear (top) and log-lin scales (bottom).

The theoretical maximum of emission occurs at $E = E_g + kT/2$ and the value of the full width at half maximum is $1.8\,kT$ (figure 3.11). Practically, the spectral width of transitions in LED is wider, in the range of 2–$4\,kT$ due to alloy broadening [68]. This is clearly visible when comparing theoretical spectrum with a measured one (fig. 3.11). Practical diodes exhibit photon emission with energy much lower than predicted by the theory. Particularly, in InGaN diodes, where the bandgap energy is dependent on the indium composition and any fluctuations in its doping can cause broadening of the spectrum.

Plotting the theoretical emission spectrum on a semi logarithmic plot shows that the high energy side of the spectrum is linear and dependent on the junction temperature.

The shape of emission spectra is sometimes approximated by a gaussian distribution for modelling purposes [12]

$$I(\lambda) \propto \frac{1}{\sigma\sqrt{2\pi}}\exp\left(-\frac{(\lambda - \lambda_{peak})^2}{2\sigma^2}\right) \tag{3.18}$$

where standard deviation relates to FWHM as [68, p. 335]

$$\sigma = \frac{\Delta\lambda}{2\sqrt{2ln2}} \approx \frac{\Delta\lambda}{2.335}. \tag{3.19}$$

Any mismatch between the model of the spectrum and the actual LED spectrum may introduce significant colour point difference. The actual spectrum of an LED is not symmetrical therefore gaussian model can introduce significant errors. To overcome this problem, Man and Ashdown [13] proposed a double gaussian model: a sum of two gaussian curves that provide much better empirical model than a single curve.

3.7   Thermal characteristics

LEDs show a very high temperature dependency. Because the junction temperature can vary significantly during normal operation (thermal cycling during low frequency PWM, dimming of the diode, heatsink and ambient temperature change) it is necessary to investigate the phenomena thoroughly. Not only the efficiency drops with increased temperature, but the colour point can move far outside the MacAdam ellipsis from the original position. Colour point shift occurs due to the change in spectrum shape. In order to quantify the spectral shift, four basic colour diodes were measured at different heatsink temperatures. The resulting spectra are gathered in figure 3.12. The results show AlGaInP red diode experiences the biggest spectrum change while the spectrum shape of InGaN diodes is not affected by the change of temperature.
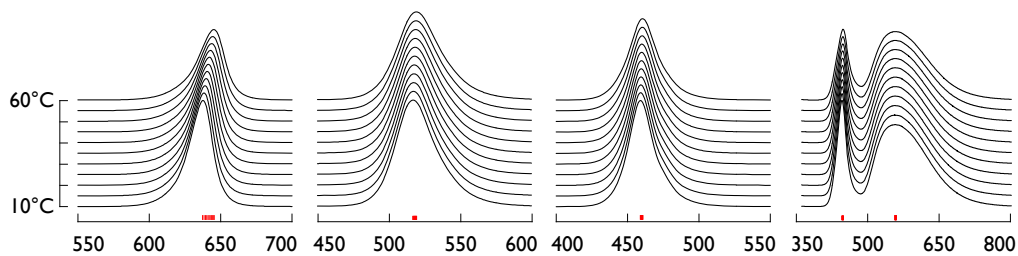

Figure 3.12: Measured change in spectral shape for Luxeon Rebel red (left), green, blue and white (right) diodes for varying heatsink temperature.

The decrease in luminous output is connected to several mechanisms: increase of non-radiative recombinations (deep level and surface) and carrier losses due to leakage over heterostructure barriers. InGaN diodes, however, experience high efficiency droop at high current value. The physical origin of the droop is not yet known [75]. Electron leakage, lack of hole injection, carrier delocalisation, Auger recombination, defects, and junction heating were suggested as explanations for this phenomenon [65, 76].

The rise of heatsink temperature corresponds to the rise of junction temperature. The relationship between junction and heatsink temperatures is not linear because the losses in the diode depend on the junction temperature. Because of the com-
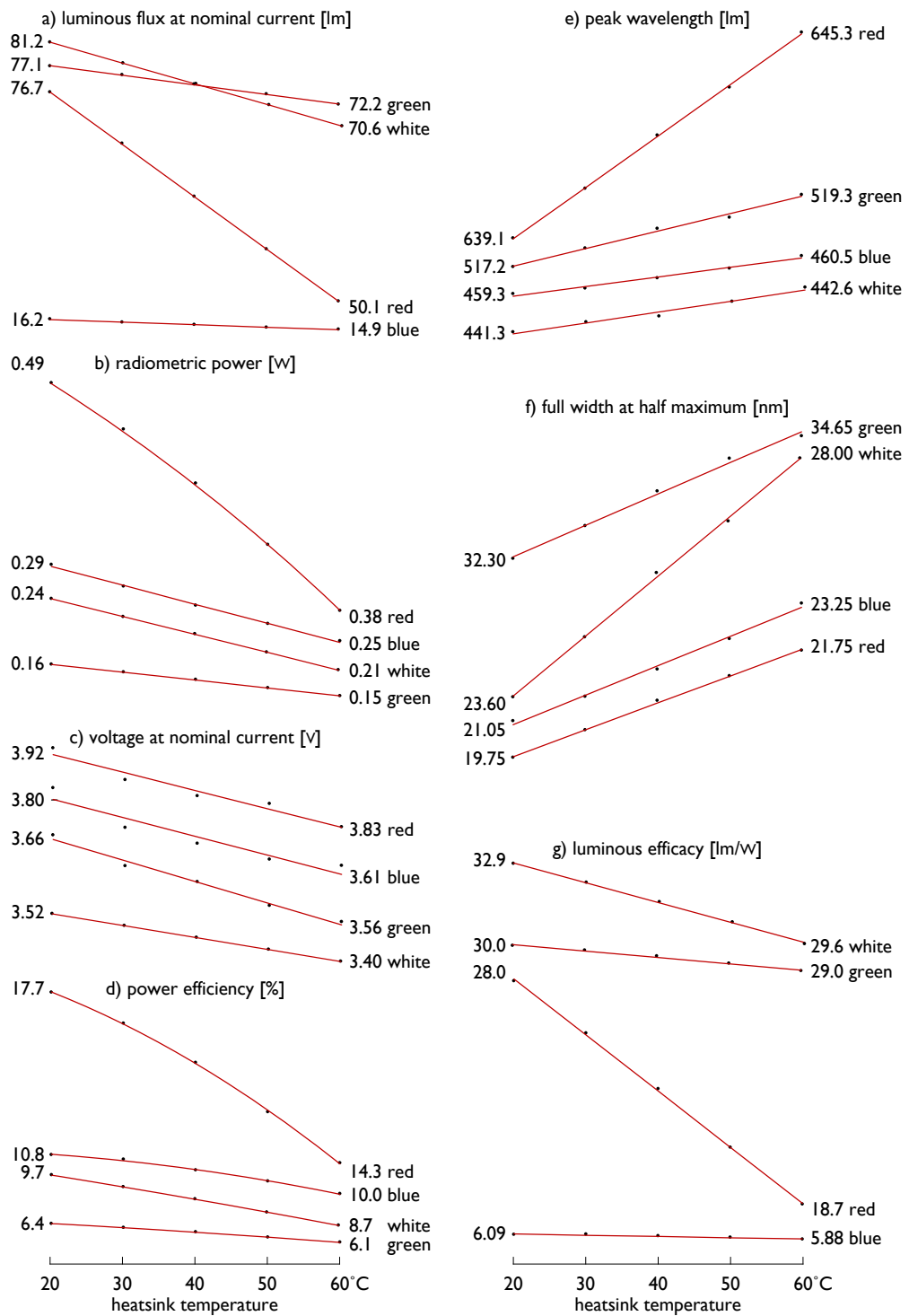
Figure 3.13: Measured Luxeon κ2 diodes' parameters with varying heatsink temperature.
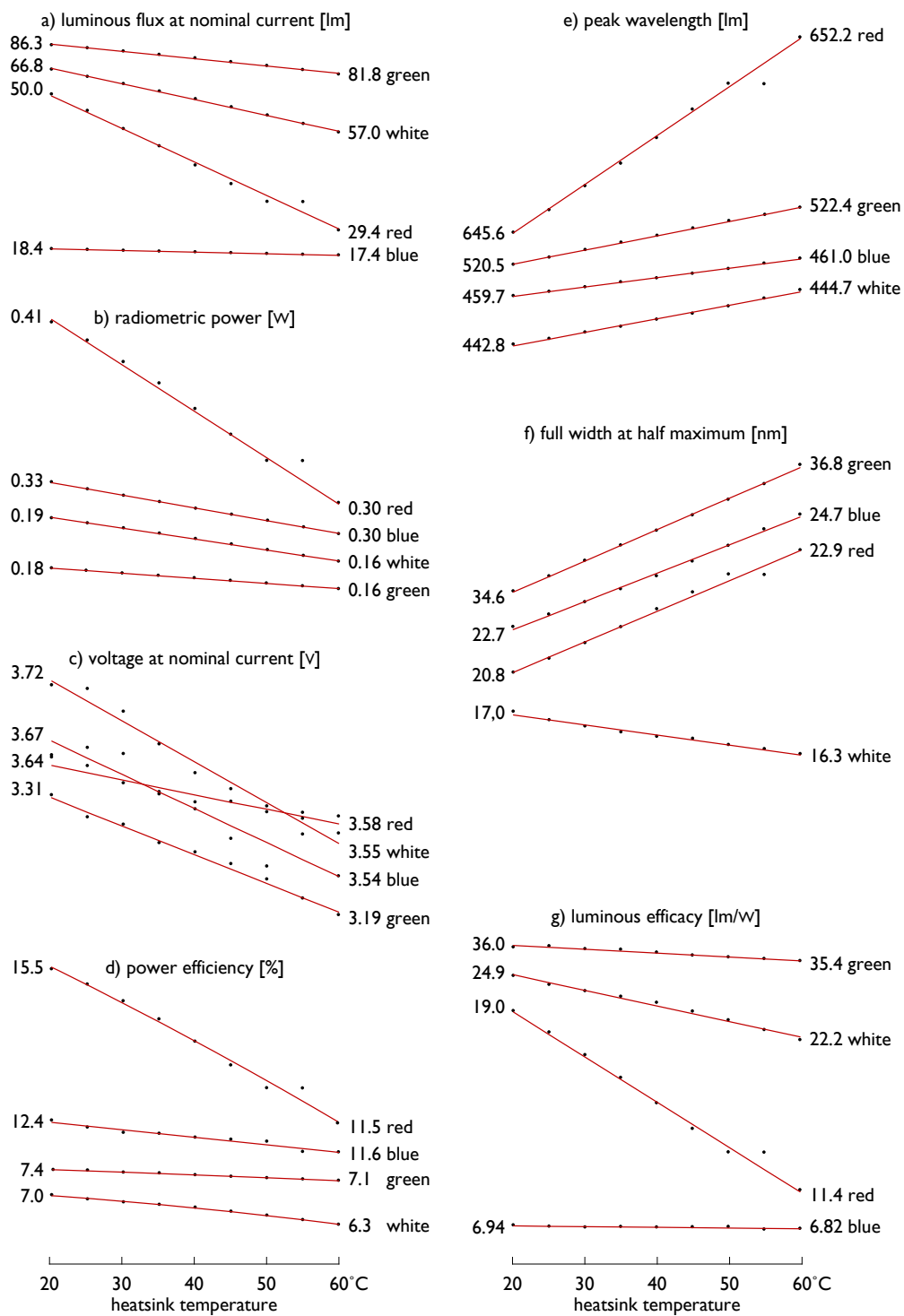
Figure 3.14: Measured Luxeon Rebel diodes' parameters with varying heatsink temperature.

plexity of junction temperature measurement, the properties of various LEDs have been analysed with respect to the heatsink temperature. Diodes' properties are plotted in figures 3.13 and 3.14 for Luxeon K2 and Luxeon Rebel diodes, respectively. The rate of change of these parameters can be approximated with a linear temperature dependencies. Temperature coefficients are gathered in table 3.2. In order to collect the necessary data the diodes were placed on thermally controlled plate and mounted to the integrating sphere. The current was set to 700 mA using a DC regulated current source. The heatsink temperature was regulated in 20–60°C range. After each change in temperature the system was allowed to reach thermal steady state after which diode's parameters were recorded.

The emissivity of the diode depends strongly on the junction temperature. Figures 3.13 b and 3.14 b show the drop of radiometric power with the increase of heatsink temperature.

The spectrum of all diode shifts towards longer wavelengths (fig. 3.13 e and 3.14 e). Both these phenomenon will influence the perceived flux (fig. 3.13 a and 3.14 a). Shift towards longer wavelengths will increase the luminous flux in blue and green diodes but will decrease it in case of red diodes. This is because the peak of eye sensitivity is at 555 nm (fig. 2.4) and moving the spectrum towards this wavelength will increase the flux and moving away from it will decrease the flux.

Luminous flux figures show that the red AlGaInP diodes are mostly affected by the temperature change because of the aforementioned phenomena. Ca. 40 % of the flux is lost with the heatsink temperature increase by 40°C for both diode families. Nitride diodes show little temperature dependence: less than 8 % of the flux is lost. Phosphor converted white diodes experience bigger loss of intensity than pure GaN diodes. With the 40°C temperature rise around 13 % was lost for both diode families.

Table 3.2: Temperature coefficients of forward voltage, luminous flux, radiometric power, peak wavelength and FWHM for the measured Luxeon diodes.

DIODE	dV_f/dT [mV/K]	dF/dT [lm/K]	dP_{rad}/dT [mW/K]	$dpeak/dT$ [nm/K]	$dFWHM/dT$ [nm/K]
Luxeon K2 red	−2.29	−0.665	−2.57	0.154	0.050
Luxeon K2 green	−2.68	−0.122	−0.35	0.052	0.059
Luxeon K2 blue	−4.71	−0.033	−0.86	0.028	0.055
Luxeon K2 white	−3.00	−0.266	−0.80	0.034	0.111
Luxeon Rebel red	−1.49	−0.516	−2.76	0.166	0.054
Luxeon Rebel green	−2.90	−0.113	−0.32	0.050	0.055
Luxeon Rebel blue	−3.44	−0.024	−0.79	0.032	0.050
Luxeon Rebel blue	−4.12	−0.243	−0.68	0.047	0.018

Many techniques may be used to obtain junction temperature on LED. Most common methods utilise forward voltage V_f, high energy slope and peak wavelength temperature dependency. High energy slope method requires knowledge of emission spectra of the diode (figure 3.11).

3.7.1 Forward voltage

The basic equation describing the temperature dependence of the forward voltage [68, 7, 8] consists of three summands.

$$\frac{\mathrm{d}V_f}{\mathrm{d}T} = \frac{eV_f/E_g}{eT} + \frac{1}{e}\frac{\mathrm{d}E_g}{\mathrm{d}T} - \frac{3k}{e} \tag{3.20}$$

First describes the influence of intrinsic carrier concentration. Second applies to the temperature dependency of the bandgap. Last summand a temperature dependency of effective densities of states N_C and N_V in conduction and valence bands, respectively and acceptor and donor concentrations, N_A and N_D, respectively [77]

$$eV_f - E_g \approx kT \ln \frac{N_D N_A}{N_C N_V}. \tag{3.21}$$

The bandgap energy can be approximated in certain temperature region by the Varnshi parameters [78, 79]. The linear-quadratic relation describing temperature dependence of the bandgap uses two empirical parameters α, β and the width of a bandgap at absolute zero temperature E_0 (table 3.3)

$$E_g = E_0 - \frac{\alpha^2}{\beta + T}. \tag{3.22}$$

To obtain the temperature dependence of the energy gap in ternary semiconductor diodes (eg. $In_xGa_{1-x}N$) a quadratic fitting is used

$$E_g(A_{1-x}B_x) = (1 - x)E_g(A) + xE_g(B) - x(1 - x)C. \tag{3.23}$$

Table 3.3: Varnshi parameters for semiconductor alloys compiled by Vurgaftman, et al. [80].

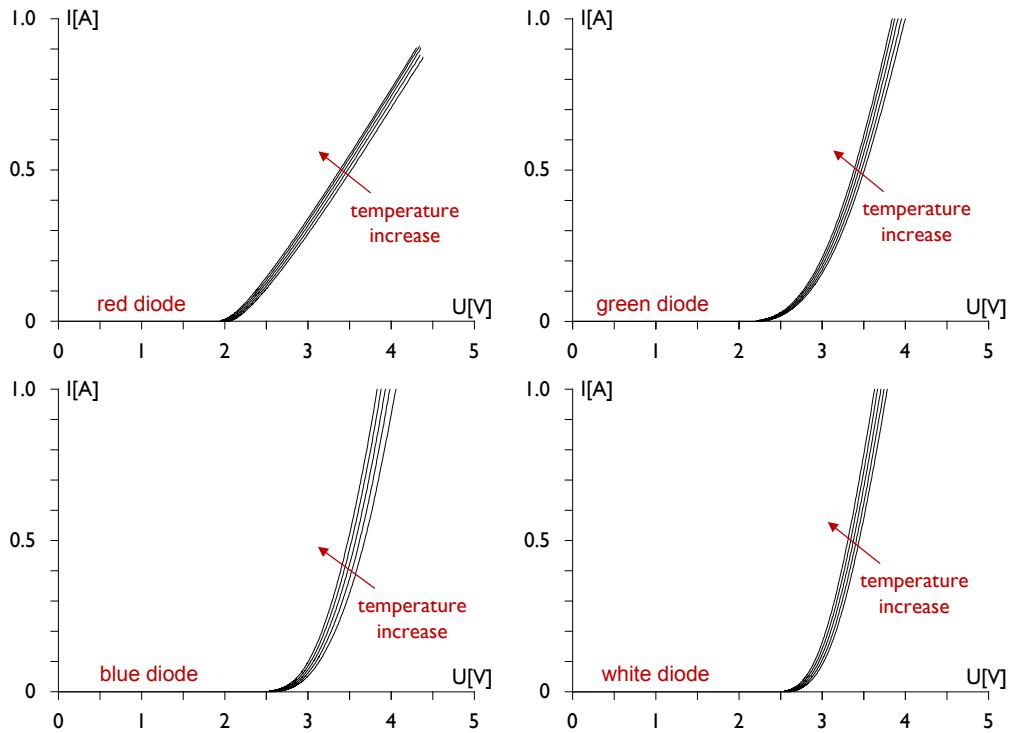| ALLOY	E_0	α [meV/K]	β [K]
GaP	2.86–2.87	0.5771	372
AlP	3.62–3.63	0.5771	372
InP	1.423	0.363	162
GaN	3.507	0.909	830
AlN	6.28	1.799	1462
InN	1.994	0.245	624

Figure 3.15: Current-voltage characteristics of red, green, blue and white diodes under varying heatsink temperature from 20°C to 50°C, every ten degrees.

Similarly, the bandgap energy of quaternary $(\mathrm{Al}_x\mathrm{Ga}_{1-x})_{0.52}\mathrm{In}_{0.48}\mathrm{P}$ barrier layers can be expressed as

$$E_g(x) = xE_g(\mathrm{Al}_{0.52}\mathrm{In}_{0.48}\mathrm{P}) + (1-x)E_g(\mathrm{Ga}_{0.52}\mathrm{In}_{0.48}\mathrm{P}) - x(1-x)C, \qquad (3.24)$$

where $C = 0.18$ eV is a bowing parameter.

Because of the forward voltage temperature dependency LEDs cannot be controlled easily with a voltage source. Self heating effect causes the drop in forward voltage moving the operating point to a higher current. Increased current yields an increase of temperature. This positive feedback may lead to thermal runaway and the destruction of the diode.

3.7.2 Thermal model

In order to estimate junction temperature of LED manufacturers provide a junction to case thermal resistance. Based on its value and power dissipated in the device as heat one may calculate temperature difference between junction and diode's case. Assuming the thermal resistance of case to heatsink interface to be negligible or known the junction temperature can be calculated with the reference to measured

heatsink temperature. However, the calculated temperature will only be valid in thermal equilibrium.

Poppe et al. [81, 82, 83, 84] analysed transient response of a diode during a cool down process. By analysing this response, the thermal impedance of the LED thermal structure can be revealed.
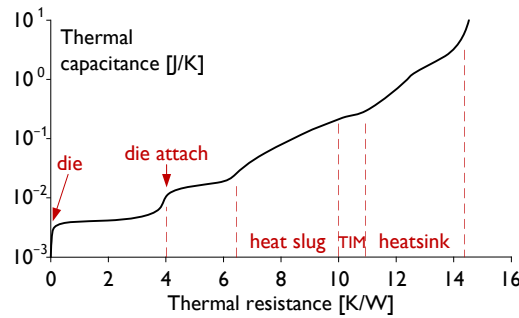
Figure 3.16: Thermal impedance curves for Luminus Rebel InGaN diode, after Parry and Rose.

Each element of LED structure represents certain thermal resistance and capacitance on the heat flow path and is connected to a time constant in thermal system response. Overall thermal system response is a sum of individual element responses [11]. Both thermal models presented in figure 3.17 are equivalent but the
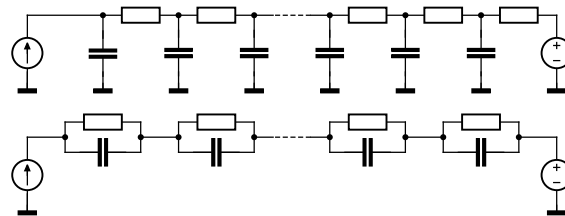

Figure 3.17: Cauer (top) and Foster (bottom) RC network models of heat flow path. Current sources represent heat generation. Voltage source represents reference temperature e.g. ambient or heatsink temperature.

Cauer structure represents physical heat flow. By reducing the number of elements in the RC ladder, the physical structure of the diode can be modelled using thermal capacitances of the LED die, die attach and heat slug and thermal resistances of the interfaces between them. High power LEDs are mounted on heatsinks using a thermal interface material that, due to its thin layer, can be modelled using only thermal resistance [15]. The heatsink itself typically has big thermal capacitance and resistance compared to LED structure.

The value of junction to case thermal resistance has been found to be nonlinearly dependent on the ambient temperature and power dissipated in the junction area [85].
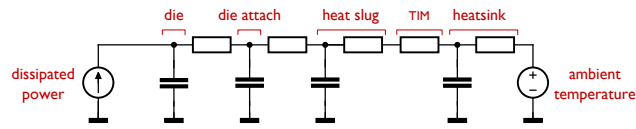
Figure 3.18: Simplified thermal model of Luminus Rebel diodes. Component values can be
derived from thermal impedance curves (fig. 3.16).

The magnitude and the direction of thermal resistance change depends on the
structure of diode [86]. This change is attributed to changing properties of ther-
mal interface material and varying thermal properties of semiconductors [85].

The heat flow path is partially determined by the internal structure of the diode
and partially by the accompanying heatsink. In order to test the influence of the
heatsink properties on the static properties of the diode a simulation was set up.
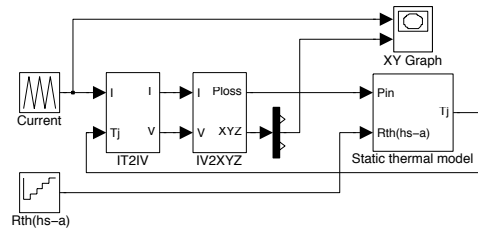The static thermal model in the simulation shown in figure 3.19 contains only

Figure 3.19: Simulation model for quantifying the effect of heatsink-to-ambient thermal
resistance on maximum luminous flux in steady-state conditions.

thermal resistances shown in figure 3.18. The capacitances are omitted as they con-
tribute only to dynamic properties of the thermal system. Junction temperature
and driving current are used to determine the forward voltage of the diode. Next,
the current-voltage information is converted into flux and dissipated power using
LED model described in detail in chapter 3.11. The flux is plotted with respect to
the driving current for different values of heatsink-to-ambient thermal resistance.
As seen in figure 3.20, the InGaN diodes are not as sensitive to the thermal re-
sistance as AlGaInP diodes. Therefore the heatsink thermal resistance and TIM
thermal resistance will limit the amount of luminous flux in steady-state condi-
tions [15]. In case of AlGaInP diodes too high thermal resistance value causes the
dF/dI to become negative. This creates dangerous effect where increasing the driv-
ing current lowers the luminous flux. In a colour control system that regulates the
diode's flux this phenomenon can lead to thermal runaway and destruction of the
luminaire. Results of the simulation show the behaviour of changing the thermal
resistance of the heat flow path. This resistance can change as an effect of curing or
ageing of TIM materials [87], airborne contaminants that cover the surface of the
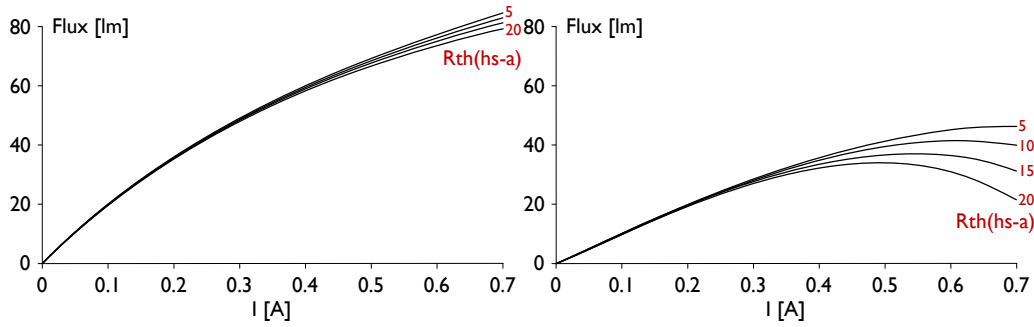
Figure 3.20: Effect of changing heatsink-to-ambient thermal resistance on luminous flux in steady-state conditions for InGaN (left) and AlGaInP (right) diode.

heatsink [88], change of fan speed in forced cooling or change of efficiency of convection cooling (increases at higher heatsink temperatures). All aforementioned processes will influence the junction temperature of the diodes therefore a proper safety margin in designing the cooling system should be incorporated.

3.8 EFFICIENCY

An ideal source of light would produce one photon for every electron injected. Because of non-radiative recombination phenomenon, not every electron-hole pair produce a quantum of light. Therefore we can define *internal quantum efficiency* as a ratio of the number of photons emitted from the active region of a LED per quantum of time to the number of electrons injected into active region per quantum of time

$$\eta_{int} = \frac{n_{created\ photons}}{n_{electrons}} = \frac{P_{int}/h\nu}{I/e} \qquad (3.25)$$

where P_{int} is the optical power emitted from the active region and I is the injection current.

The photons created in the active region have to be extracted into free space. This can be very challenging as the photons are being created in III-V crystals with high refractive indices ($n \approx 3.5$ for AlGaInP and $n \approx 2.4$ for InGaN materials). Some light extracting features like texturing of a crystal surface has to be incorporated into LED design. At the same time, the light radiation characteristic has to meet the demands of the market. Therefore development of a LED packages with high light extraction efficiency C_{ext} is still an ongoing process. Currently (January 2009) C_{ext} reaches up to 60% in AlGaInP and 80% in InGaN high power devices.

The *external quantum efficiency* is designed as a ratio of the number of photons emitted into the free space per quantum of time to the number of electrons injected

into active region per quantum of time

$$\eta_{ext} = \frac{n_{extracted\ photons}}{n_{electrons}} = \frac{P/h\nu}{I/e} = C_{ext} \cdot \eta_{int} \qquad (3.26)$$

A *power efficiency*, often refereed to as *wall plug efficiency* is defined as

$$\eta_{power} = \frac{P_{optical}}{P_{electrical}} \qquad (3.27)$$

where $P_{electrical}$ is electric power supplied to the diode and $P_{optical}$ is the optical power of light extracted from the structure.

A *luminous efficacy* is a measure of how well the electromagnetic radiation is converted into luminous flux.

$$\eta_{lum} = \frac{F_{lum}}{P_{optical}} = \frac{683 \int V(\lambda) P(\lambda) \mathrm{d}\lambda}{\int P(\lambda) \mathrm{d}\lambda} \qquad (3.28)$$

The highest possible luminous efficacy is defined by the eye sensitivity curve [fig. 2.4] and is equal to 683 lm/w when the light is a monochromatic source emitting at 555 nm.

In lighting applications it is necessary to know how well the input electrical power is converted into visible light. This is called *luminous efficacy of a source* or *wall plug efficacy*.

$$\eta_{lum,wp} = \frac{F_{lum}}{P_{electrical}} = \eta_{lum} \cdot \eta_{power} = \frac{683 \int V(\lambda) P(\lambda) \mathrm{d}\lambda}{IV} \qquad (3.29)$$

Highest practically achievable wall-plug efficacies, for various light sources, has been collected in table 3.4.

When carriers are trapped inside a quantum well a part of their energy has to be dissipated by phonon emission in order to match the carriers' energy to one of the available states inside a well.

Table 3.4: Efficacies of common light sources compared to state of the art LEDs.

LIGHT SOURCE	LUMINOUS EFFICACY	COMMENTS
incandescent	12.6 lm/w	40 w tungsten incandescent
incandescent	17.5 lm/w	100 w tungsten incandescent
fluorescent	90 lm/w	
gas discharge	200 lm/w	low pressure sodium lamp
white LED	138 lm/w	Narukawa et al., 2008 $I_f = 350$mA
red LED	119 lm/w	Osram, 2010, $I_f = 350$mA
green LED	181 lm/w	3M, 2009, phosphor converted, $I_f = 350$mA

A white LED can be produced by using a phosphor down-conversion of a blue or UV light (pump) e.g. mixing blue InGaN light with yellow light from YAG:Ce phosphor. Phosphor has to convert blue photons ($\approx 460\,\text{nm}$) into yellow photons ($\approx 570\,\text{nm}$) so their energy has to drop. It is impossible to do the down-conversion without losing a part of the energy [12]. The Stokes energy loss is given by

$$\Delta E = h\nu_1 - h\nu_2 = \frac{hc}{\lambda_1} - \frac{hc}{\lambda_2} \tag{3.30}$$

thus the efficiency of down-convertion is

$$\eta = 1 - \frac{h\nu_1 - h\nu_2}{h\nu_1} = \frac{\lambda_1}{\lambda_2}. \tag{3.31}$$

3.9 LIFETIME

In contrast to traditional, incandescent and fluorescent light sources, LEDs do not tend to fail catastrophically. Instead, the output flux decreases with time and operating junction temperature. The degradation mechanisms were the subject for many lifetime studies. The cause and the magnitude of the lumen change differs depending on the structure and materials of the diode and its driving conditions: shape of the driving current (pulsed or direct) and the temperature. Solder join failures and change in thermal properties of the thermal interface materials used for mounting the diodes can also influence diodes' properties.

For white LEDs, a colour shift towards lower colour temperatures can be seen due to the yellowing of the die [89]. Studies show that mechanisms of LED structure and package deterioration like generation of threading dislocations and yellowing and cracking of encapsulating lenses are connected to the structure temperature [17, 90, 89]. The increase of the leakage current results in a decreasing photon generation and the deterioration of LED encapsulant lens lowers the structure extraction efficiency. In extreme cases, the defects may short the device rendering it unable to generate light [91].

NITRIDE DIODES

According to a 60000 hour study presented by Grillot et al. the main cause of lumen degradation in AlGaInP diodes are the increase in defects concentration and in leakage current [20]. The overall degradation, defined as the relative change of the luminous flux with respect to the flux at the beginning of the test, was found to behave according to equation

PHOSPHIDE DIODES

$$D = D_1 + D_2\,j + (D_3 + D_4\,j)\ln(t) \tag{3.32}$$

where D_{1-4} are diode dependent coefficients, j is the current concentration and t is the time.

As LED do not tend to fail catastrophically, instead their light output slowly decreases over time, the LED lifetime if defined as the time to some predefined intensity drop. Manufacturers use this measure together with driving current and junction temperature to quickly asses the lifetime of the devices they are using (fig. 3.21).

The ASSIST alliance recommends using two metrics B50 and L70 to approximate the useful lifetime [92]. B50 corresponds to the time where 50 % of the device population fails. L70 denotes the time in which LEDs lose 30 % of the initial luminous flux. Therefore combined B50/L70 metric predicts when more than 50 % of the diodes will drop below 70 % of the initial flux [93]. Depending on the application other sets can be used, e.g. B10/L70 or B10/L70.
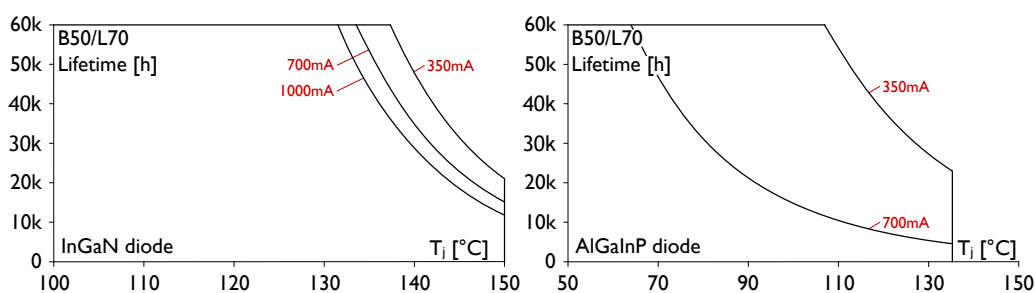

Figure 3.21: B50/L70 lifetime predictions for InGaN (left) and AlGaInP (right) Luxeon Rebel diodes [94].

3.10 DIMMING

Intensity of an LED can be controlled in many different ways. Because of the small dynamic resistance and the temperature dependency of forward voltage LEDs are typically current controlled. All dimming techniques vary the mean current supplied to the diode changing the diode's intensity. Different current waveforms with the same average value can have different effect on LED output light. The peak wavelength can change creating a colour shift in the mixed light. Flux, and therefore efficiency, can change depending on a dimming method. Gu et al. [2] report changes up to 100% in efficiency depending on the dimming method, diode colour and the operating point.

Following chapters describe four different control schemes and analyse their effect on light-emitting diodes: two basic control schemes used commonly—pulse width modulation and amplitude modulation; a hybrid AM/PWM dimming technique proposed by the author and a pulse code modulation technique.

3.10.1   Pulse width modulation

Because LEDs are semiconductor-based devices they can be turned on and off very quickly. The minimum frequency at which pulsed light sources are perceived as constant is predicted by Ferry-Porter law

$$critical\ flicker\ frequency = k(\log L - \log L_0) \tag{3.33}$$

where L is the luminous intensity, L_0 is the threshold intensity and k is a constant having a typical value of 12 Hz/decade. The CFF is furthermore dependent on the size of the stimuli and its position relative to the eye [95]. Minimum modulation frequency value used in the industry is 60 Hz, but for high intensity, fast moving light sources this frequency should be increased to 300–1000Hz range to avoid flicker [4].

Brightness control is achieved by modulating current pulse width ⎍. A duty cycle d is a ratio of a on pulse time to the period of modulation frequency. Average luminous intensity is a product of the duty cycle and the constant luminous intensity during the on pulse.

$$I_{f,avg} = d \cdot I_{f,max} \tag{3.34}$$

Light output can be dimmed down to 0% and linear control can be easily obtained. However, peak emission shifts and bandwidth narrowing occur during PWM dimming and have to be taken into account when designing control strategy for light mixing [1, 3].
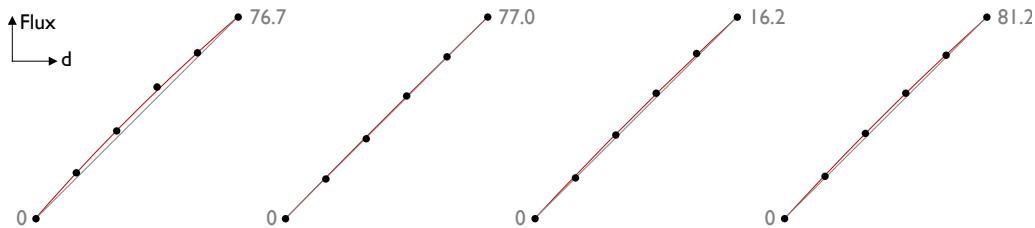

Figure 3.22: Measured luminous flux for PWM dimming of red, green, blue and white (left to right) diodes as a function of duty cycle. Data points correspond to the duty cycle equal to: 0, 0.2, 0.3, 0.6, 0.8 and 1.0. PWM experiences almost ideal dimming linearity.

Under decreasing duty cycle the peak wavelengths shifts towards shorter wavelengths for AlGaInP [2, 3] and InGaN [2] diodes. The shift is explained by cooling of the active area in the chip with decreased duty cycle and, as a result, broadening of the bandgap energy [68].
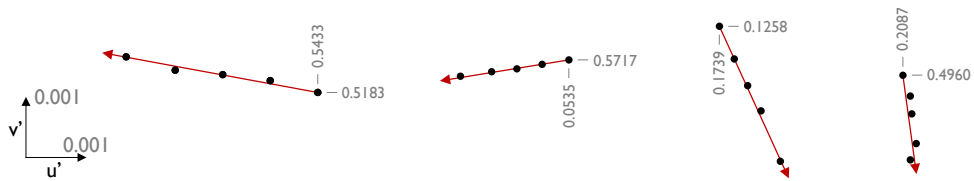
Figure 3.23: Measured colour shifts for the PWM dimming of red, green, blue and white (left to right) diodes. Arrow shows the direction of decreasing flux. Data points correspond to the duty cycle equal to: 1.0 (marked with CIE 1976 colour coordinates), 0.8, 0.6, 0.4 and 0.2.

Because of small colour shifts and very good linearity this dimming method is the most widely used in industrial applications. LED driver operates in a pulsed mode either with maximal forward current of the diode or no current. Therefore it can be easily optimised for a single operating point.

3.10.2 Amplitude modulation

Amplitude modulation, sometimes referred to as continuous current reduction (CCR), uses variable DC current to control the intensity of the diode. Because the efficiency of LEDs increases with decreasing current concentration in the active area, the AM dimming scheme is inherently nonlinear. The increase of luminous efficiency over pulse width modulation can be as high as 100% for low intensities for green InGaN diodes [2].
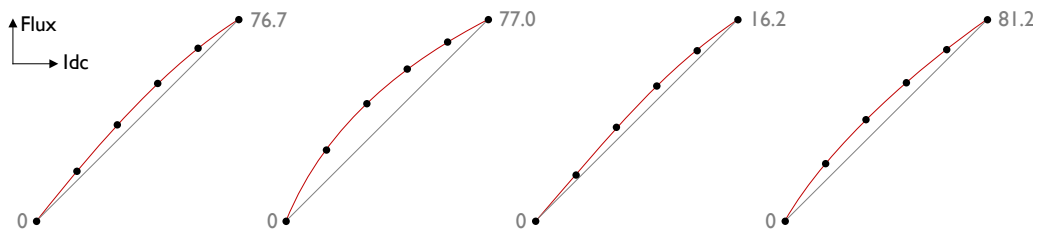
Figure 3.24: Measured luminous flux for AM dimming of red, green, blue and white (left to right) diodes as a function of forward current. Data points correspond to following currents: 0, 0.14, 0.28, 0.42, 0.56 and 0.7 A.

The dimming range for amplitude modulation is typically limited to 10–100% range. This is because at very low current levels the SNR is low therefore the accuracy of the current control is limited.

Very big colour shifts occur when using AM in both pure colour diodes and phosphor converted white diodes [1]. Typically, AlGaInP diodes experience peak wavelength shift towards shorter wavelengths and InGaN LEDs towards longer wavelengths.

Figure 3.25: Measured colour shifts for AM dimming of red, green, blue and white (left to right) diodes. Arrow shows the direction of decreasing flux. Data points correspond to following currents: 0.7 (marked with CIE 1976 colour coordinates), 0.56, 0.42, 0.28 and 0.14 A. Note the 10× increase of scale compared to fig. 3.23.

Due to big spectral shifts and output flux to driving current nonlinearity, use of AM dimming technique in colour crucial applications is limited. Although if these problems would be solved, amplitude modulation would provide much more efficient dimming scheme than pulse width modulation.

LED driver has to provide power with varying voltage and current therefore the driver cannot be optimised for single operating point. On the other hand the luminous efficacy of the diode increases significantly with decreased current and the efficacy of the driver-LED system can be much higher than in PWM dimmed luminaires.

3.10.3   Hybrid modulation

Tse et al. [96, 5, 97, 98] proposed a general driving technique that is somewhere between the PWM and AM. Their technique bases on the possibility to control the high and low peak current that is simultaneously dimmed with PWM. Changing the peak currents would influence the efficiency of the LED and PWM signal would control the brightness without big colour shifts. A variation of this technique was studied where low peak current is set to zero and the intensity of the diode is controlled by varying the peak current and duty cycle ⎓⎓. The LED driver is off during $1 - d$ part of the dimming period therefore losses in the converter are reduced. LED is controlled by varying both duty cycle and peak current.

$$I_{f,avg} = d \cdot I_{f,peak} \tag{3.35}$$

It is always possible to roll back to either PWM or AM control by setting either current or duty cycle, respectively, to their maximum value.

Hybrid PWM/AM modulation creates a degree of freedom in diode control. This gives an opportunity to optimise colorimetric and radiometric properties of an LED.
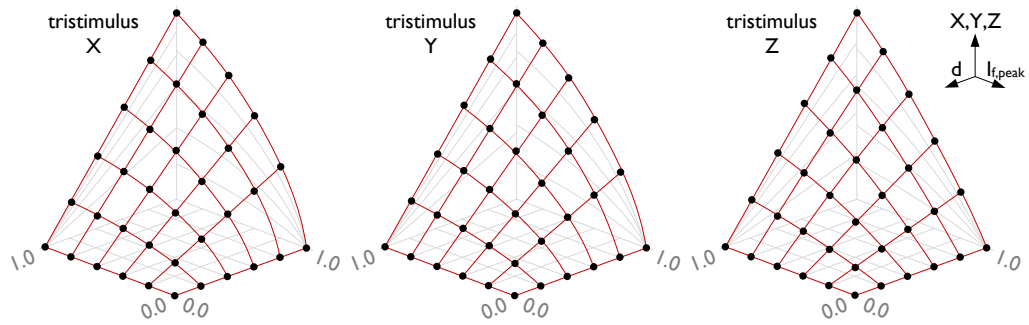
59

Figure 3.26: Measured, normalised tristimulus values for PWM/AM hybrid dimming as a function of relative peak current and duty cycle. Data gathered at constant heatsink temperature.

Noticing the fact that for white phosphor converted diode PWM and AM dimming methods create opposite colour shifts (figures 3.23 and 3.25) and the direction of this shift is almost parallel to the shift caused by the temperature change (fig ref needed) one can use hybrid AM/PWM to stabilise both colour point of a diode and luminous flux over a range of temperatures.
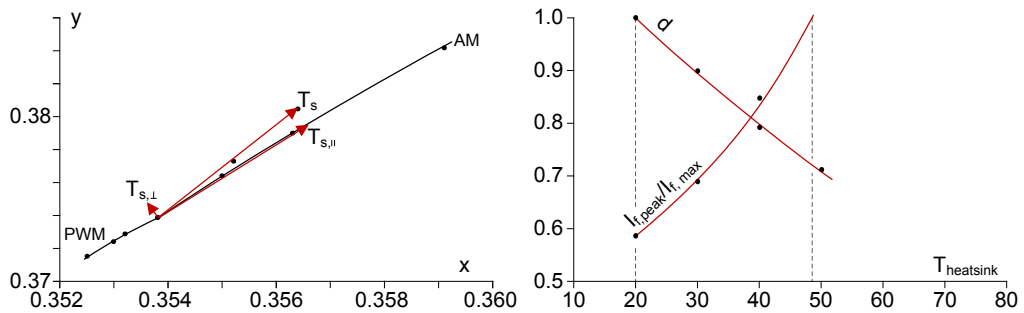
Figure 3.27: Colour shifts of white PC LED caused by PWM and AM dimming mechanisms and the directions of shift caused by increasing the heatsink temperatures (left). Relative driving current and duty cycle for obtaining stable colour point.

Figure 3.27 shows the directions of colour shift caused by two dimming schemes and the shift caused by the changing heatsink temperature. Shift caused by the temperature can be subdivided into two vectors: parallel and perpendicular to the shifts caused by dimming. The perpendicular part cannot be controlled using hybrid dimming technique but is very small in magnitude.

An experiment was set up to prove the hypothesis. A white, phosphor converted diode was placed in the test adapter. The heatsink temperature was set to 20°C and the diode was energised with nominal current. Colour coordinates and luminous flux were recorded when the diode reached thermal steady state. After increasing

the heatsink temperature to 30°c the duty cycle and driving current were manually adjusted to bring the colour point as close to the starting colour point without changing the flux value. It was only possible if the current was increased over the nominal current value. Although the average current value did not exceed the nominal driving current diode's lifetime may be affected, which may not be recommended in some applications. In order not to exceed the maximum forward current, the experiment was repeated with lower initial driving current equal to around 60 % of nominal current (which corresponds to 70 % of the nominal flux value). The flux was kept constant in the heatsink temperature range of 20–48°c while maintaining very low colour shift without overdriving the diode.

Decreasing the initial current (at $d = 1$) or allowing for overdriving increases the range at which the colour point is kept stable.

Table 3.5: Current and voltage values needed to obtain stable colour point with the change of the heatsink temperature. Colour coordinates and the distance from initial colour point given in the CIE 1976 colour space.

$T_{hs}[°C]$	d [p.u.]	I_{peak} [A]	F [lm]	u'	v'	$\Delta u'v'$
20	1.000	0.411	53.3	0.2085	0.4981	0.00000
30	0.905	0.485	53.3	0.2085	0.4981	0.00000
40	0.796	0.597	53.3	0.2084	0.4982	0.00011
50	0.716	0.712	53.3	0.2083	0.4982	0.00021

Measured data points with the colour distance from the initial colour point are presented in table 3.5. Plotting the required current and duty cycle values (fig. 3.27) reveals that the relationship between the controlled values and heatsink temperature is almost linear and can be expressed using following formulas:

$$I_{f,peak} = 0.0001 \cdot T_{hs}^2 + 0.0030 \cdot T_{hs} + 0.3088$$
$$d = 0.0004 \cdot T_{hs}^2 - 0.0122 \cdot T_{hs} + 1.2309 \tag{3.36}$$

Another application of hybrid dimming can be at stabilising peak wavelength position during dimming. Colour sensors used in luminaires as a colour feedback are very sensitive to the change of spectral shape [99]. This phenomenon is caused by the very narrow shape of LED spectra. The spectra can shift towards shorter and longer wavelengths during dimming and as a result of heatsink temperature change. If one of this mechanisms of colour shifts could be eliminated, the accuracy of the colour sensors could in theory be improved.

InGaN diodes exhibit opposite peak wavelength shifts under PWM and AM. A hybrid modulation could therefore fix the peak wavelength position (fig. 3.28).

The initial peak wavelength position was recorded at nominal driving conditions at 20°c heatsink temperature. The duty cycle was then lowered by 10 % and, by adjusting the peak current, the peak wavelength was moved to initial value. The
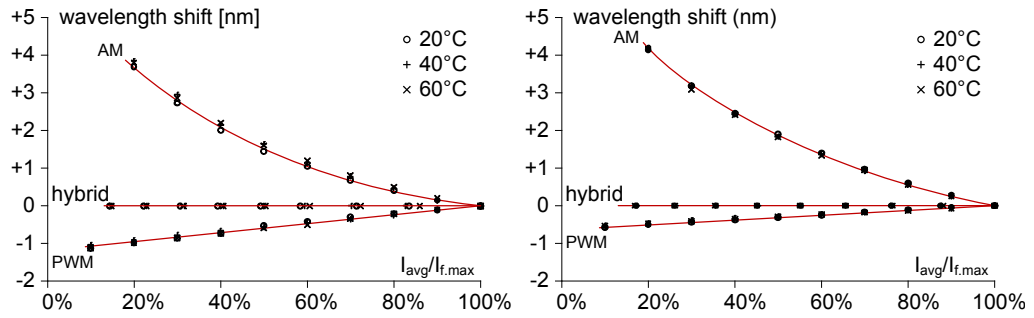
61

Figure 3.28: Peak wavelength shift with respect to the nominal position at 20°C for green (left) and blue (right) diodes under different dimming techniques.

process was repeated for duty cycles down to 20 %. Pairs of peak current and duty cycle that satisfied the constant peak wavelength conditions were recorded also for 40 and 60°C to examine if the relationship is temperature dependent.
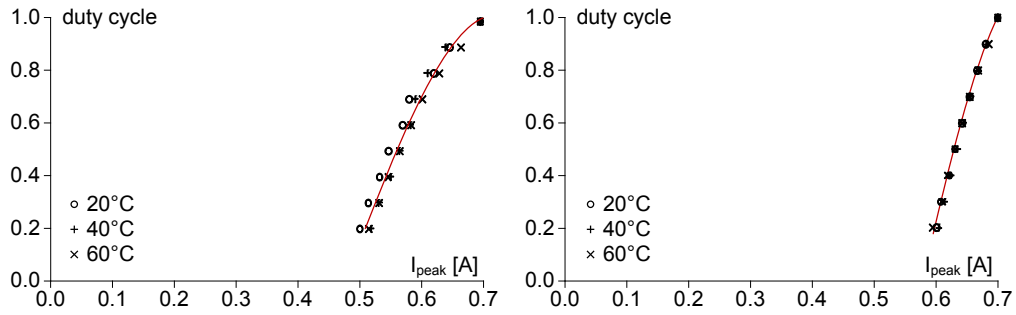

Figure 3.29: Driving conditions for green (left) and blue (right) diodes necessary to obtain stable peak wavelength position as shown in figure 3.28.

Results (fig. 3.29) show that the relationship between peak current and duty cycle needed to obtain stable peak wavelength is not dependent on heatsink temperature and can be described be the following equations

$$I_{f,peak,green} = 0.1739 \cdot d^2 + 0.0079 \cdot d + 0.5109$$
$$I_{f,peak,blue} = 0.0410 \cdot d^2 + 0.0727 \cdot d + 0.5851 \tag{3.37}$$

For both green and blue InGaN diodes colour point resulting from hybrid dimming moves towards the border of CIE 1931 diagram thus the colour of the light becomes purer. As seen in figure 3.30 the colour shift is confined to a one step MacAdam ellipse.
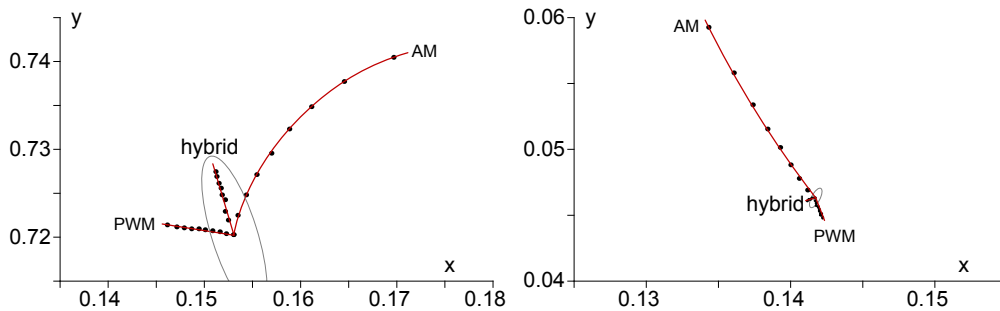
Figure 3.30: Colour point shift for green (left) and blue (right) diodes under different dimming techniques. Heatsink temperature fixed to 20°C.

3.10.4 Pulse code modulation

A pulse code modulation uses a current pattern that resembles the binary representation of the desired dimming value, e.g. 0.33 can be written as 01010100_b and the corresponding current pattern looks like this ⌐⌐⌐. The dimming value is therefore encoded in the light pattern and can be decoded by other devices [100]. The first pulse in the pattern has a duration of T and corresponds to the most important bit of the binary dimming value. The next pulse is two times shorter and corresponds to the next bit. Last pulse has the width of $T/2^{n-1}$, where n is the resolution of the dimming signal. The total pulse pattern period has to be lower than 300 Hz to avoid visual flicker and therefore the dimming resolution is limited by the timing properties of the microcontroller and the length of the shortest pulse. Ashdown [4] proposed the use of temporal dithering in order to increase the dimming resolution in PCM.

Figure 3.31: Spectra of PWM (left) and PCM (right) current shape. Base frequency, marked with red bar, is 200 Hz in both cases. The DC value for both signals is the same. The PCM signal contains more high frequency components in the spectrum.

The biggest advantage of PCM over PWM is that the driving pattern can be generated for many channels using only a single timer in a microcontroller thus there is no need for hardware PWM generators. The current spectra contains more high frequency components than under a PWM driving scheme (figure 3.31) therefore this dimming method is mostly suitable for driving high number of low power diodes like in a matrix displays.

Recalling the fact that forward voltage of a diode is proportional to both junction temperature and forward current and diode colorimetric properties are dependent on junction temperature and forward current one can construct a model that estimates colorimetric properties basing only on instantaneous values of diode's current and voltage.

Diodes' tristimulus properties and forward voltage have to be measured at various junction temperatures and, if AM or hybrid dimming is to be used, various current levels in order to create a model.

DATA ACQUISITION   A green InGaN test diode was placed on thermally controlled heatsink. Temperature was set in increments of 10°C in the 5–55°C range. The current was controlled in the 10–100% of nominal current range allowing the diode to reach thermal steady state after each change. At that point current, voltage and tristimulus values were measured. Four wire setup was used to gather electrical parameters in order to avoid voltage drop on terminals and cables.

SURFACE FITTING   Collected data was fitted to a polynomial. Three separate functions were created for each of the tristimulus values and one function was created for the radiometric power. The higher order of polynomial used to represent the data the more computational power is required to use the model. Also the model may be overfitted in which case the measurement error would be visible in the model. By a trial and error approach the lowest order of polynomial still representing measured data accurately was found to be in a form of:

$$a_0 + a_1 I + a_2 I^2 + a_3 I^3 + a_4 V + a_5 V^2 \tag{3.38}$$

Table 3.6: Model coefficients a_n for the measured diode model.

	a_0	a_1	a_2	a_3	a_4	a_5	R^2
X	-21.5417	49.8094	-38.8920	16.1661	17.3677	-3.4374	0.99997
Y	30.7711	150.6126	-119.9930	45.0165	-38.8748	11.2224	0.99991
Z	33.1338	14.2156	-6.8995	2.0560	-28.7647	6.2476	0.99986
P_{rad}	120.6807	189.0981	-145.9986	52.2570	-118.7007	28.9492	0.99989

MODEL VERIFICATION AT DC CURRENT   In order to test the model and the data fitting, six measurement points were taken at random heatsink temperatures and driving currents. Measured current, voltage and tristimulus values are compared to estimated tristimulus values in table 3.7 and the corresponding colour points for the measured and modelled data are shown in figure 3.33. For all measured data points the colour distance between the measured and estimated colour points is much lower than the just noticeable colour distance. This implies that the model predicts the chromaticity and intensity of LEDs with high enough accuracy.
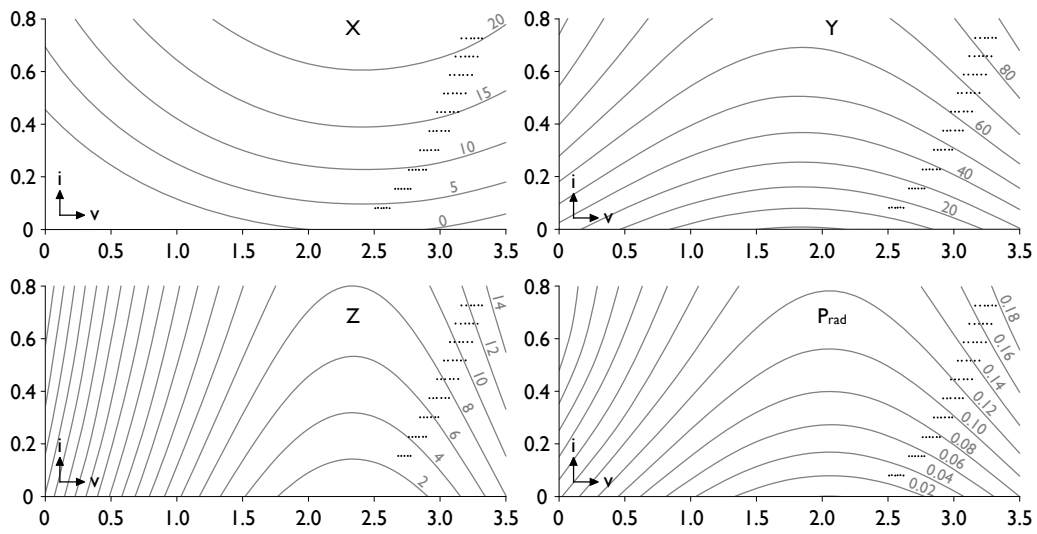
Figure 3.32: Model surfaces of *X*, *Y* and *Z* tristimulus values and optical power of the measured LED. Model is only valid in the vicinity to the measured data points.
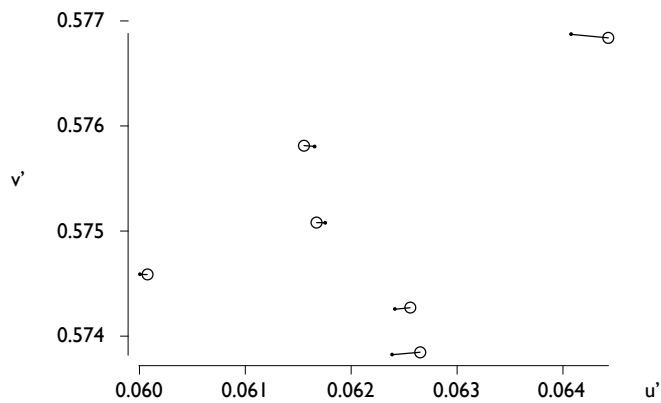
Figure 3.33: Measured (○) and modelled (·) colour points on CIE 1976 chromaticity diagram for various combinations of driving current and heatsink temperature.

To test the accuracy of the model the test diode was driven with 200 Hz pulsed current with various duty cycles (fig. 3.34) at constant heatsink temperature. Before each measurement the diode was allowed to reach thermal steady state. Optical parameters were integrated over multiple PWM periods. Current and voltage waveforms were recorded with 250 kS/s speed with 12 bit ADC. Few periods were extracted from the waveforms and instantaneous current and voltage values were converted to tristimulus values using the previously created model. Resulting data was integrated and divided by the measured time period to obtain average tristimulus values and the resulting colour point.

Table 3.7: Measured current, voltage and tristimulus values compared to corresponding modelled tristimuls values. Error in model is visible as colour distance between estimated and measured colour points.

		MEASURED			MODELLED			
v	i	X	Y	Z	X	Y	Z	ΔE_{ab}^*
3.1388	0.5253	16.917	71.915	10.266	16.883	71.847	10.261	0.0049
2.9731	0.3523	13.142	54.639	7.097	13.138	54.528	7.080	0.0661
3.0566	0.4648	15.820	65.558	8.933	15.801	65.394	8.904	0.0738
3.1348	0.6151	18.846	76.887	10.942	18.809	76.911	10.970	0.0596
3.1809	0.6949	20.216	82.294	12.013	20.180	82.488	12.087	0.3098
2.8123	0.2355	9.935	39.530	4.628	9.899	39.604	4.643	0.2676
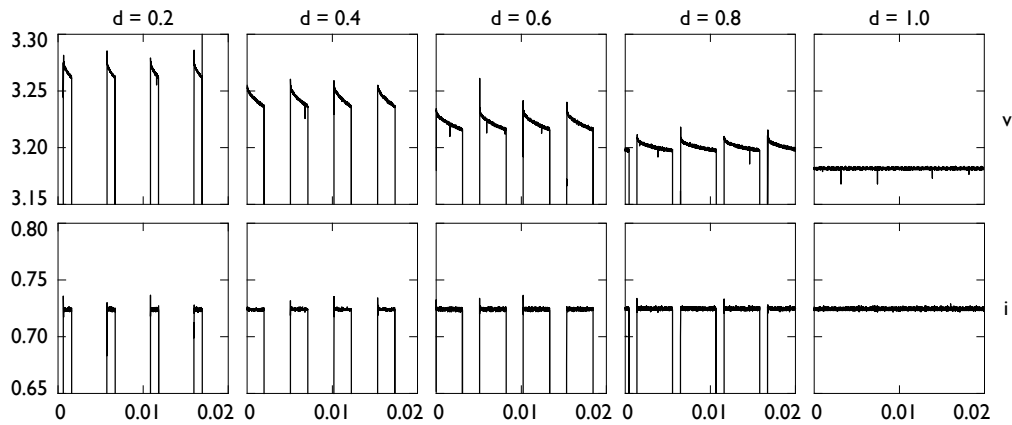
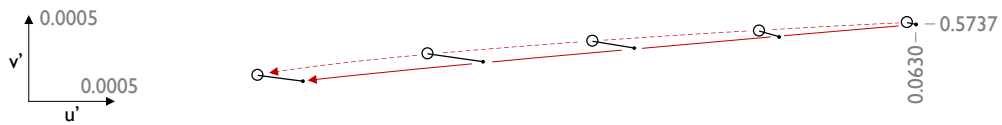Figure 3.34: Measured current and voltage waveforms for the modelled diode at various duty cycles.

Figure 3.35: Difference between measured colour shift for PWM dimming (dashed line) and colour shift obtained using current-voltage model (solid line). Arrow shows the direction of decreasing duty cycle. Colour point at nominal driving current ($d = 1$) marked with $u'v'$ coordinates.

Results, summarised in table 3.8, show that the model accurately predicts the colour shift of the diode. It is therefore possible to use this model, as a colour feedback regardless of the dimming scheme used in the luminaire. The accuracy of this method lower with lowering duty cycle. This may be attributed to fast thermal and electrical transients that tend to dominate at very low duty cycle values. In order to measure these transients precisely, much higher voltage and current sampling would

be required. Also lower number of samples are used to estimate the colorimetric properties therefore noise in the measurement may influence the accuracy of the model.

Table 3.8: Measured and modelled tristimulus values of the test diode and the colour distance between the corresponding colour points.

	MEASURED			MODELLED			
d	X	Y	Z	X	Y	Z	ΔE_{ab}^*
0.2	4.0447	17.3423	2.6773	3.8695	16.6655	2.5735	2.4091
0.4	8.1630	34.4009	5.2286	8.1669	34.6032	5.2597	0.4614
0.6	12.5078	51.9626	7.8009	12.5364	52.2906	7.8480	0.4869
0.8	16.8984	69.2601	10.2805	16.9262	69.5062	10.3069	0.1671
1.0	20.7419	83.9519	12.3199	20.7569	84.0777	12.3363	0.0319

The number of measurement points needed to describe diode's behaviour depends on the complexity of the model and the desired operating point. If the diode is to be dimmed using PWM scheme, it is sufficient to measure the parameters at single forward current with varying heatsink temperature. COMMENTS

If the radiometric power of the emitted light is also modelled, it may be used together with the thermal model of the system to completely describe luminaire's behaviour. Subtracting the optical power from input electrical power gives the power losses in the diode structure. This loss will create a temperature rise with respect to heatsink temperature according to the thermal description of the heat flow path 3.17. Resulting temperature increase in the junction can be translated into forward voltage change resulting a new operating point to be fed back to the current-voltage model.

Very often luminaire consists of strings of series connected light-emitting diodes. It is possible to model each diode in the string measuring separately individual diode voltages and string current but this approach is not practical. A single model created for the whole string would therefore be beneficial. Some restrictions in thermal design exist when using the current-voltage model with multiple LEDs. Model is created with only two external stimuli changing: current and heatsink temperature. MODELLING LED STRINGS

4 Luminaire control

Polychromatic solid-state luminaires need a control system in order to keep the desired luminance and colour level stable. Diodes' parameters will change during normal operation due to self heating, ambient temperature variations and during ageing and these changes should be compensated by a proper control mechanism.

Firstly, the open loop control is discussed. The methods of choosing an appropriate operating point, depending on the number of primaries used in the luminaire, are given. For luminaires containing more than three primaries optimisation techniques may be used to optimise some of the lamp parameters like luminous flux or efficacy.

A review of existing colour control methods is presented, where the main control mechanisms: temperature feed forward, flux feedback and colour coordinates feedback are discussed. A colour control loop basing on the current-voltage diode model, presented in chapter 3.11 is shown.

Various optimisation possibilities are discussed. From optimally choosing a working point of a polychromatic luminaire to optimisation benefits for trichromatic luminaire using the hybrid dimming mechanism, presented in chapter 3.10.3.

4.1 COLOUR CONTROL STRATEGIES

Control scheme will differ depending on the number of available colours in luminaire. For polychromatic luminaires (three or more basic colours) control of colour point and luminance is possible by adjusting intensities of individual diodes. In trichromatic luminaires there is only one solution for the colour equations that yields the desired colour point. If the luminaire consists of four or more diodes the number of possible solutions may be infinite therefore the lamp operation can be optimised by choosing the operating point.

4.1.1 Open loop

Open loop system uses only the calibration matrix 4.1 to calculate required duty cycle. The accuracy of this control method is limited by the self-heating of the diodes and the changes of ambient temperature because the values in calibration matrix are measured at a single temperature value. However this type of control can still be used in luminaires where colour accuracy is not important. Because the system is modelled as a set of linear equations and linear algebra principles are used to find the operating point the PWM dimming mechanism should be used in the luminaires controlled with this method.
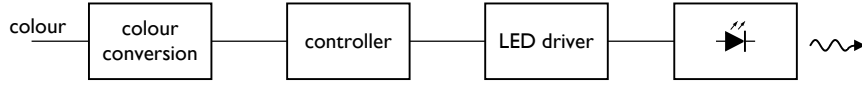
Figure 4.1: Open loop luminaire control system.

The optical characteristics of a trichromatic luminaire are characterised by a calibration matrix C containing diodes' tristimulus values at nominal conditions.

$$C = \begin{bmatrix} X_1 & X_2 & X_3 \\ Y_1 & Y_2 & Y_3 \\ Z_1 & Z_2 & Z_3 \end{bmatrix} \tag{4.1}$$

The calibration matrix is strongly temperature dependent as the diode experience peak wavelength shift and flux change with the change of the temperature.

Duty cycle needed to obtain desired color point and luminance level can be calculated by using inverse of the calibration matrix.

$$d = \begin{bmatrix} d_1 \\ d_2 \\ d_3 \end{bmatrix} = C^{-1} \cdot \begin{bmatrix} X \\ Y \\ Z \end{bmatrix} \tag{4.2}$$

If any of the calculated duty cycle values is negative then the desired colour point lays outside the gamut of the device. If, on the other hand, any of the values is above 1 then the desired luminance level cannot be reached without overdriving the diode.

UNDERDETERMINED SYSTEM When using more than three different diode colours, the system becomes underdetermined as there are three equations for each of the tristimuli value and $n > 3$ unknowns—the diodes' relative output. The calibration matrix expands to a $3 \times n$ matrix composed of the diodes' tristimulus values.

$$C = \begin{bmatrix} X_1 & X_2 & \cdots & X_n \\ Y_1 & Y_2 & \cdots & Y_n \\ Z_1 & Z_2 & \cdots & Z_n \end{bmatrix} \tag{4.3}$$

For an underdetermined system, there are typically infinitely many solutions of the problem. Every solution to underdetermined will have the form $d + c \cdot s$ where x is a particular solution of $Cx = b$ and $c \cdot s$ is a linear combination of solution to ROW REDUCTION $Cs = 0$. As an example a system composed of four diodes: red, green, blue and white, defined by calibration matrix

$$C = \begin{bmatrix} 60 & 6 & 17 & 22 \\ 25 & 26 & 5 & 20 \\ 0 & 4 & 100 & 20 \end{bmatrix} \tag{4.4}$$

70

generating $X = 20$, $Y = 40$ and $Z = 20$ will be investigated. In order to solve the system equations an augmented matrix $(C|b)$ is composed.

$$(C|b) = \begin{bmatrix} 60 & 6 & 17 & 22 & | & 20 \\ 25 & 26 & 5 & 20 & | & 40 \\ 0 & 4 & 100 & 20 & | & 20 \end{bmatrix} \quad (4.5)$$

Using Gauss-Jordan elimination matrix 4.5 is transformed into following form

$$(C|b) = \begin{bmatrix} 1 & 0 & 0 & 0.2677 & | & 0.1560 \\ 0 & 1 & 0 & 0.4770 & | & 1.3604 \\ 0 & 0 & 1 & 0.1809 & | & 0.1456 \end{bmatrix} \quad (4.6)$$

The corresponding system equations are given by

$$\begin{aligned} d_1 + 0.2677 \cdot d_4 &= 0.1560 \\ d_2 + 0.4770 \cdot d_4 &= 1.3604 \\ d_3 + 0.1809 \cdot d_4 &= 0.1456 \end{aligned} \quad (4.7)$$

Introducing $c = d_4$ and rewriting equations in matrix form yields

$$\boldsymbol{d} = \boldsymbol{d}_{re} + c \cdot \boldsymbol{s}_{re} = \begin{bmatrix} d_1 \\ d_2 \\ d_3 \\ d_4 \end{bmatrix} = \begin{bmatrix} 0.1560 \\ 1.3604 \\ 0.1456 \\ 0 \end{bmatrix} + c \begin{bmatrix} -0.2677 \\ -0.4770 \\ -0.1809 \\ 1 \end{bmatrix} \quad (4.8)$$

Green diode in the initial solution $\boldsymbol{d}_{re}$ has to be overdriven by 36%, therefore by varying the value of c another solution has to be found.

By analogy to equation 4.2 solution to the underdetermined system can also be calculated using an inverted matrix. As inversion of the non-square matrix is not possible therefore in order to find an algebraic solution to the problem a pseudoinverted matrix $\boldsymbol{C}^+$ can be used [101].

$$\boldsymbol{d}_{pinv} = \begin{bmatrix} d_1 \\ d_2 \\ \vdots \\ d_n \end{bmatrix} = \boldsymbol{C}^+ \cdot \begin{bmatrix} X \\ Y \\ Z \end{bmatrix} \quad (4.9)$$

Pseudoinversion yields the solution that has the smallest Euclidean norm $||d||_2$. This solution may or may not lay within the feasible solution space, where all duty cycles are in range of $0 \leq d_n \leq 1$. Luminaire described by calibration matrix 4.4 and pseudoinverted matrix

$$\boldsymbol{C}^+ = \begin{bmatrix} 0.0189 & -0.0076 & -0.0032 \\ -0.0164 & 0.0356 & 0.0004 \\ 0.0012 & -0.0043 & 0.0098 \\ -0.0026 & 0.0142 & 0.0011 \end{bmatrix} \quad (4.10)$$

generating $X = 20$, $Y = 40$ and $Z = 20$, according to eq. 4.9 should be driven as follows

$$d_{pinv} = C^+ \cdot \begin{bmatrix} 20 \\ 40 \\ 20 \end{bmatrix} = \begin{bmatrix} 0.0226 \\ 1.0350 \\ 0.0413 \\ 0.5866 \end{bmatrix} \tag{4.11}$$

This particular solution lays outside available duty cycle values. In order to find other possible solutions a linear combination of the basis vectors for the kernel (null space) for calibration matrix C can be added to solution vector d. The null space for matrix C is defined as set of vectors s for which $C \cdot s = 0$

$$s = \begin{bmatrix} -0.1929 \\ -0.4704 \\ -0.1508 \\ 0.8478 \end{bmatrix} \tag{4.12}$$

A feasible solution can be calculated by adding a linear combination of the basis vector s. In this case e.g. $c = 1/10$ will yield a feasible solution:

$$d = d_{pinv} + c \cdot s = \begin{bmatrix} 0.0226 \\ 1.0350 \\ 0.0413 \\ 0.5866 \end{bmatrix} + \frac{1}{10} \begin{bmatrix} -0.1929 \\ -0.4704 \\ -0.1508 \\ 0.8478 \end{bmatrix} = \begin{bmatrix} 0.0033 \\ 0.9880 \\ 0.0262 \\ 0.6714 \end{bmatrix} \tag{4.13}$$

In general, finding a feasible solution by means of algebraic calculation will require finding an initial point and moving to the feasible range.

CONCLUSIONS   Both techniques described above, pseudoinversion and row reduction, find the solution in form of initial solution plus a way to move the solution within the solution space. Graphical representation (fig. 4.2) of the solution space shows for system described by calibration matrix 4.4 shows both initial solutions. The advantage of using row elimination is that initial solution will always yield a vector with $3 - n$ zeroes and searching through solution space is limited by searching within $c_{re} \in [0, 1]$. The performance of the two algorithms was measured in MATLAB and the results are summed up in table 4.1.

Table 4.1: Initial answer calculation time using pseudoinversion and row reduction.

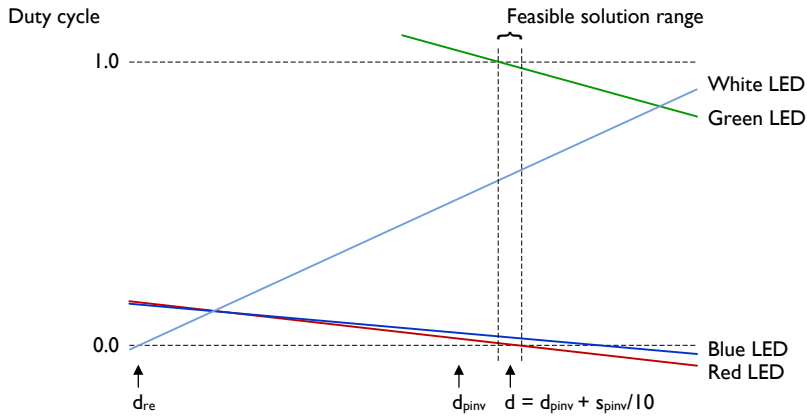| NUMBER OF DIODES	PSEUDOINVERSION	ROW REDUCTION
3	0.234 ms	0.617 ms
4	0.251 ms	0.836 ms
5	0.249 ms	0.983 ms
6	0.233 ms	1.166 ms

Figure 4.2: Graphical solution for four diode underdetermined system. Feasible solution range is a subset of all solutions where all relative intensities are in the range of [0,1]. Initial solutions d_{re} and d_{pinv} described by equations 4.8 and 4.11, respectively, shown in the solution space.

To test the accuracy of the open loop control system, a luminaire consisting of three, control accuracy red green and blue, diodes was set up to deliver 50 lumen of white light ($x = 1/3$ and $y = 1/3$). Required tristimulus values calculated by eq. 2.4 are: $X = 50$, $Y = 50$ and $Z = 50$. The luminaire was placed in the input port of the integrating sphere. Diodes' properties were measured using small duty cycle ($d = 0.1\%$) pulsed current so that the junction temperatures and heatsink temperature are almost equal to ambient temperature. Required duty cycles were calculated using equation 4.2 and previously measured calibration data.
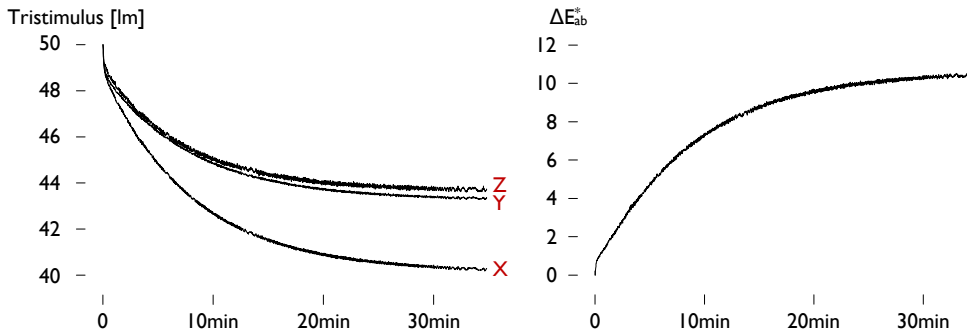
Figure 4.3: Measured tristimulus values of the open loop luminaire control system (left) and corresponding colour difference from the initial colour point (right). Self-heating of the LEDs decreases their luminous flux therefore their tristimulus values decrease. The X value experiences the biggest drop because of the high red diode temperature dependency.

The self-heating of the diodes yields a drop of the tristimulus values (fig. 4.3). After ca. two minutes, the colour point moved past the just noticeable difference level. The colour shift is dependent on the junction temperature therefore it is affected by the thermal properties of the heat flow path and the variations of the ambient temperature. Transient response of the luminaire is connected with the thermal capacities of the system components. Fast transient (time constant less than one min.) in the beginning of the experiment is connected with the heating of the diode structure and the aluminum PCB, the diodes are mounted on. Slow transient (time constant ca. ten minutes) is the result of the heatsink thermal mass.
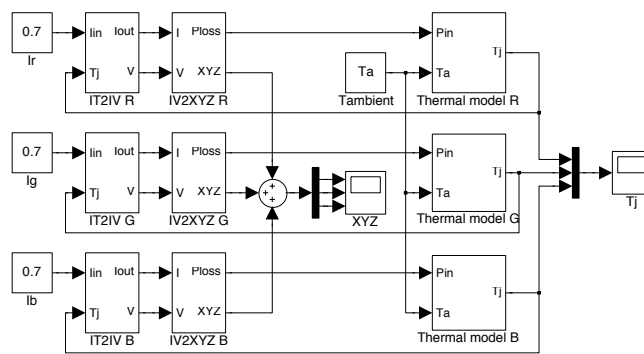
Figure 4.4: Simulation model of RGB luminaire using a current-voltage diode model.
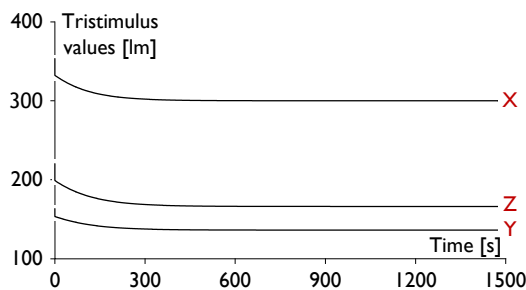
Figure 4.5: Tristimulus values of the simulated RGB luminaire. Diodes driven with nominal 0.7 A current.

4.1.2 Temperature feed forward

LED characteristics are mostly affected by the junction temperature. Therefore a control scheme basing on temperature measurements is most convenient. The LEDs junction (active, light-emitting region) temperature cannot however be measured directly. The practical approach is to measure heatsink or ambient temperature and approximate the junction temperature by means of LED thermal model. Garcia et al.

[14, 102] designed a flux estimator to control the output flux during steady state and transients conditions.
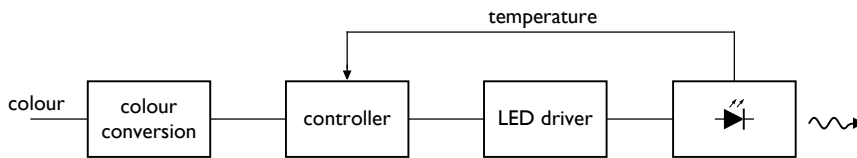

Figure 4.6: Temperature feed forward luminaire control system.

In the TFF control loop controller adjusts the calibration matrix based on the measured or estimated junction temperature. The drawback of this method is that the light output (colour, intensity) is not the directly controlled variable. Every variation in LED model will result in long-time error [24].

4.1.3 Flux feedback

Flux feedback control scheme can maintain constant flux output for each of the colours. This can be done by placing photodiodes near each LED colour or by using one photodiode and a time sequence measurement of mixed light. This can easily overcome flux variations with ageing but cannot compensate for peak wavelength shifts.
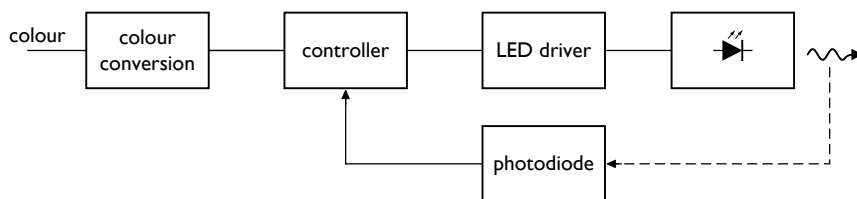

Figure 4.7: Flux feedback luminaire control system.

Special care must be taken with placement of the sensor. Ambient light can distort flux measurement therefore either the placement of the sensor should minimise its influence or the ambient light can be measured independently and the subtracted from the measured LED flux.

4.1.4 Flux feedback with temperature feed forward

A combination of temperature feed forward and flux feedback methods can produce a very accurate control scheme because it can compensate for both wavelength shift and flux change due to ageing and temperature variations. However,

the method relies on model data describing relation between wavelength shift and temperature ($d\lambda/dT$).
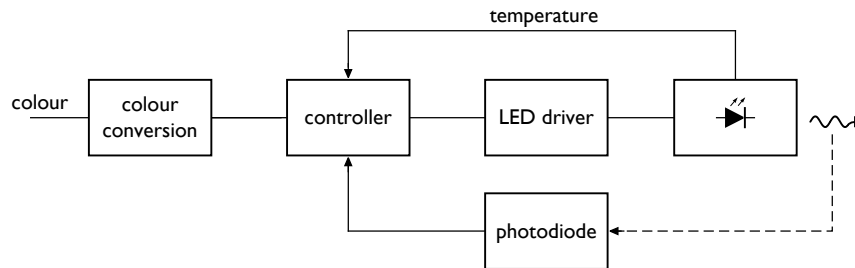

Figure 4.8: Flux feedback with temperature feed forward luminaire control system.

4.1.5 Colour coordinates feedback

A very high accuracy of colour reproduction can be achieved using colour coordinates feedback because the mixed light is a directly controlled variable. No model parameter variation or temperature difference can influence steady state output.
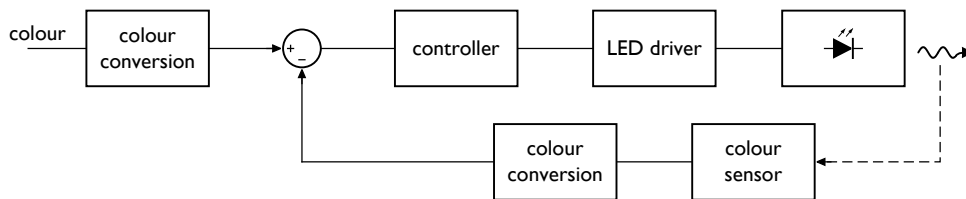

Figure 4.9: Colour coordinates feedback luminaire control system.

The challenge in designing such converter is choosing an appropriate sensor. There are many colour sensors available on the market. General trichromatic sensors consist of three photodiodes with spectral responses in red, green and blue color spectrum. Sometimes colour sensors cover also IR and UV parts of the spectrum.

The temperature and ageing problems are not entirely solved by using a colour sensor, because this problems can affect the sensor itself. The expected sensor lifetime should match the expected lifetime of the whole lamp.

In general case of n-chromaticity filter, the response of the filter has to be transformed from its colour space into working colour space of the luminaire. At least three measurements are necessary in order to calibrate the sensor. Typically, the calibration procedure includes more than three points to increase the accuracy of
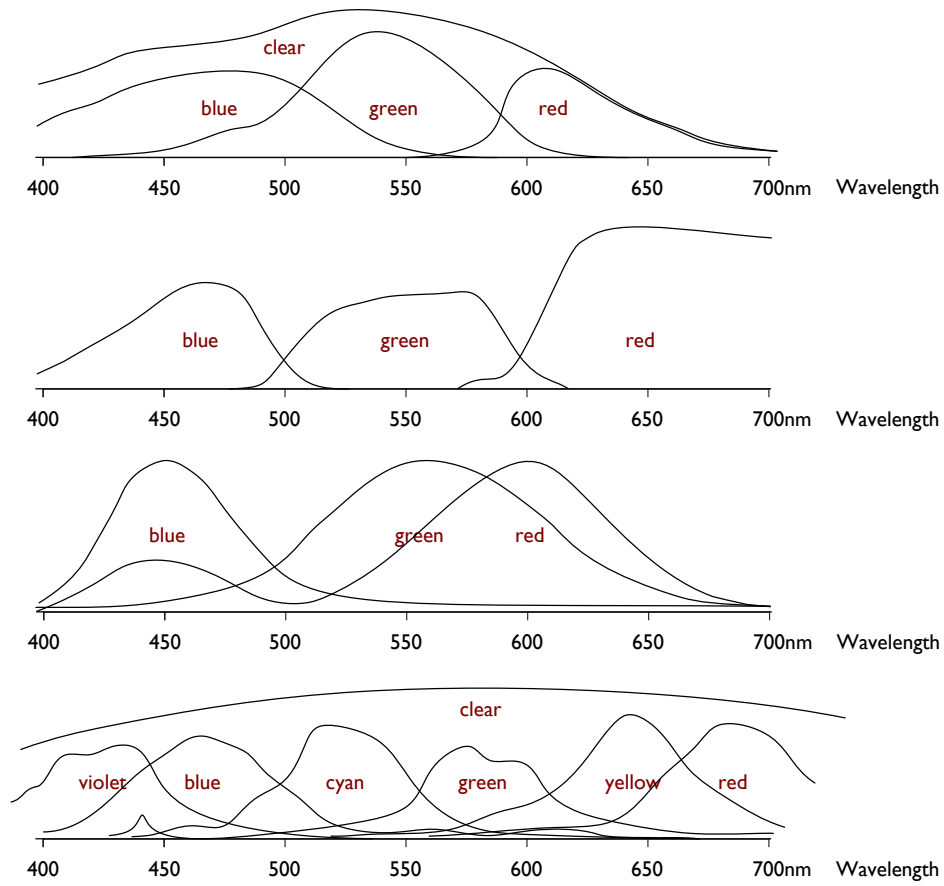
76

Figure 4.10: Spectral responses of colour sensors: Taos TCS 230, MaZeT MCS3AS, MaZeT MTCSICT and MaZeT MMCS6 (top to bottom). Data taken from individual sensor datasheets.

the calibration. Calibration matrix for n-chromaticity luminaire is a $3{\times}n$ matrix

$$C = \begin{bmatrix} c_{11} & \ldots & c_{n1} \\ c_{12} & \ldots & c_{n2} \\ c_{13} & \ldots & c_{n3} \end{bmatrix} \tag{4.14}$$

Taking m sensor measurements and comparing them to X, Y and Z measured values yields two matrices

$$S = \begin{bmatrix} s_{11} & \ldots & s_{m1} \\ \vdots & \ddots & \vdots \\ s_{1n} & \ldots & s_{mn} \end{bmatrix} \qquad XYZ = \begin{bmatrix} X_1 & \ldots & X_m \\ Y_1 & \ldots & Y_m \\ Z_1 & \ldots & Z_m \end{bmatrix} \tag{4.15}$$

Because of the finite resolution and accuracy of the measurement, the system can

be approximated by equation

$$XYZ \approx C \cdot S \tag{4.16}$$

Calibration matrix C can be approximated using least square method. First eq. 4.16 is transposed yielding

$$S^T \cdot C^T \approx XYZ^T \tag{4.17}$$

and the least square solution is calculated

$$\widehat{C}^T = \left(S \cdot S^T\right)^{-1} S \cdot XYZ^T$$

$$\widehat{C} = \left(S \cdot XYZ^T\right)^T \cdot \left(\left(S \cdot S^T\right)^{-1}\right)^T$$

$$\widehat{C} = XYZ \cdot S^T \cdot \left(S \cdot S^T\right)^{-1} \tag{4.18}$$

A generic trichromatic colour sensor was calibrated with RGB and RGBW luminaire using random operating points (varying x and y colour coordinates and intensity values) and equation 4.18. Results (fig. 4.11) show that the RGB system can be accurately measured using trichromatic sensor for RGBW luminaire measurement yields high colour variations.
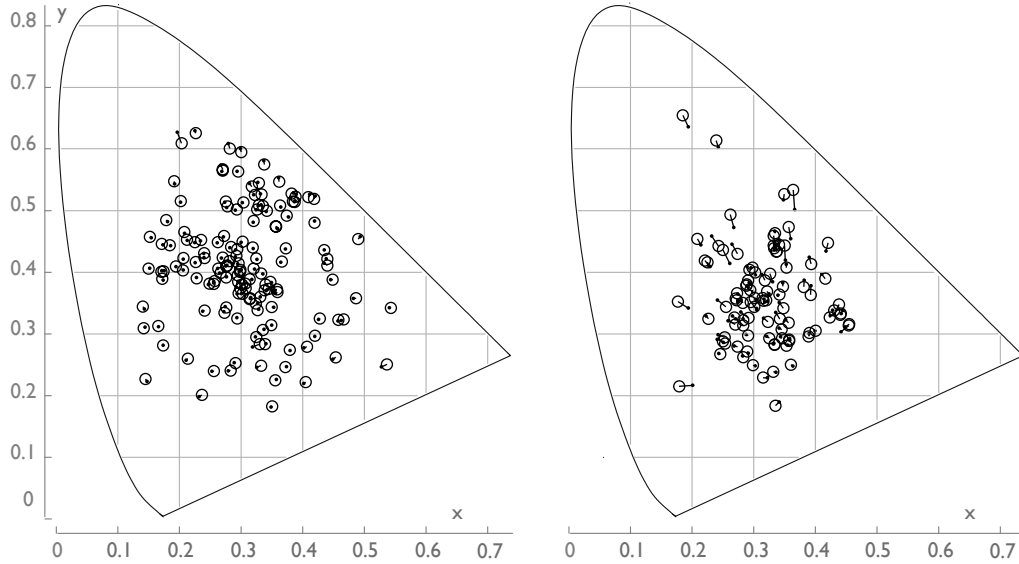

Figure 4.11: Colour sensor calibration points for RGB luminaire (left) and RGBW luminaire (right). Circles show colour points measured by spectrometer. Dots show colour points measured by the sensor transformed using least square solution matrix $\widehat{C}$.
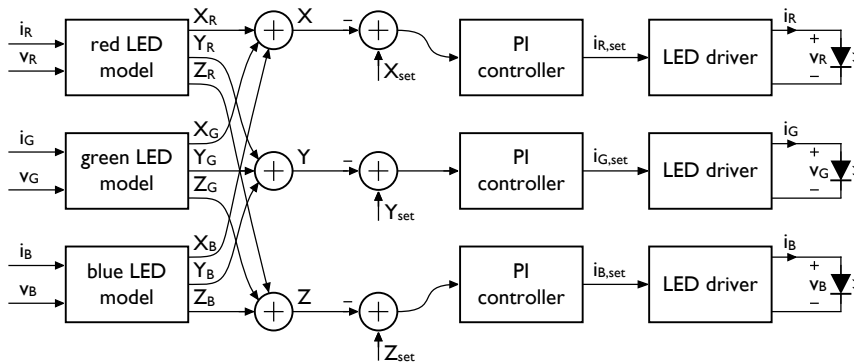
Figure 4.12: Colour control loop utilising ɪᴠxʏᴢ models. Measured current and voltage of three diode strings are converted into instantaneous tristimulus values. These values are used as a feedback for three current controllers.

4.1.6 *Current-voltage model based colour control*

A current-voltage model described in chapter 3.11 can be used in a ʀɢʙ luminaire colour control loop instead of optical feedback (fig. 4.12). Voltages and currents of all colour strings present in the luminaire need to be measured. Electrical parameters are converted into tristimulus values using a model created during calibration. Respective tristimulus values are summed and subtracted from the command values. Resulting errors are fed into three ᴘɪ controllers which control red, green and blue diode strings. The bandwidth of these controllers can be limited to few hundred hertz as human eye cannot see light changes above circa 100 Hz. ʟᴇᴅ colorimetric properties are dependent on the forward current and the junction temperature. The active area and internal ʟᴇᴅ structure heats up in the millisecond time range and is too fast for the human eye to perceive. ʟᴇᴅ junction will be also affected by the heatsink temperature. The time constant of a heatsink can be in the range of few seconds to few minutes and colour control loop should compensate for this change.

The current information is present in the colour control loop in the form of current command. This information can be fed back to ʟᴇᴅ model to decrease the number of sensors needed, as shown in fig. 4.13. Current command differs from actual current only during transients therefore this control scheme is best used with ᴀᴍ dimmed luminaires.

4.2 OPTIMISATIONS

There are two possibilities for optimising ʟᴇᴅ based luminaires' colorimetric properties. The number of different colours present in the luminaire will affect achiev-
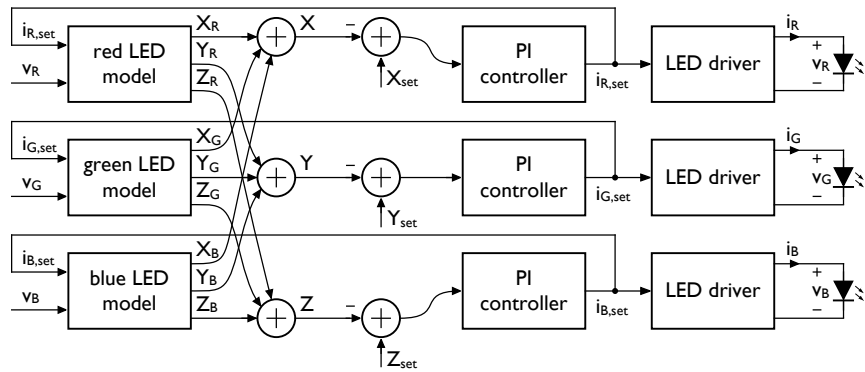
Figure 4.13: Colour control loop where the current feedback is taken from the current controller.
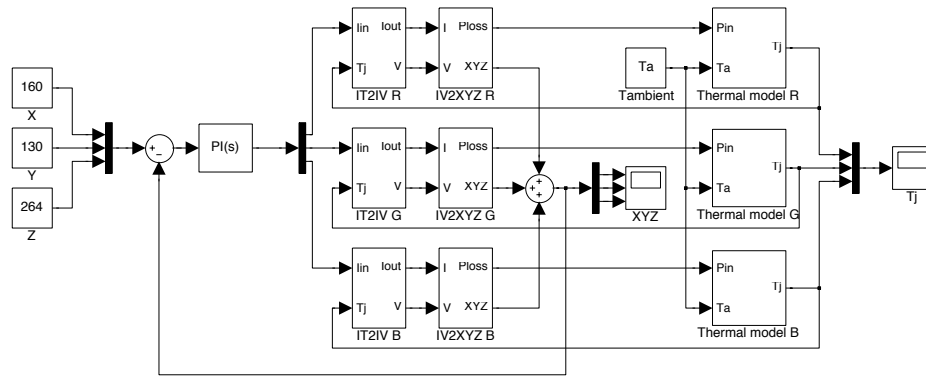

Figure 4.14: Simulation model of a trichromatic RGB luminaire controlled by three PI controllers and using current-voltage diode model.

able gamut, luminous flux and the light quality of the luminaire. Žukauskas et al. analysed the properties of polychromatic LED luminaires [33, 103]. By increasing the number of different colours present in the luminaire from three to four the maximum colour rendering index can be increased from approximately 90 to approximately 98. Also the choice of the peak wavelengths of the particular diode colour will influence both the CRI and efficacy of the luminaire [103, 104]. Chapter 4.2.1 shows an example how an optimisation procedure can influence the luminaire design.

Another possibility for optimising colorimetric properties is by the diode control. Optimisation is generally possible when a system is underdetermined systems. In polychromatic luminaires consisting of at least four different colours, like RGBA or RGBW luminaires, one colour point can be reached by many different combinations of the diode intensities (figure 4.2). However, a RGB luminaire has three control variables (intensity of each diode colour) and three colour equation therefore there

is no possibilities to optimise the control as there is exactly one solution to the system. A hybrid diode control described in chapter 3.10.3 can be used to increase the number of variables in the system. Each diode is controlled with both duty cycle and peak current therefore the number of variables present in the system doubles. Chapter 4.2.2 shows the benefits of using hybrid dimming in a trichromatic RGB luminaire.

It is worth noting that even though the optimisation procedures will find many operating points that yield the same tristimulus values, the spectrum at these operating points will vary. It means that the direct light seen by the observer will not change with changing operating point but the light reflected from various objects may change due to metamerism. This creates a practical limit of how fast should the operating point change so that the observer will not notice the change created by the optimisation procedure. Also multiple lamps, each running an optimisation routine, generating light wi the same tristimulus values may produce different spectra.

4.2.1 Linear programming

Linear programming is a technique of finding the optimum (maximum or minimum) of a objective function given a set of constrains on the function variables. Linear programs are typically solved by simplex algorithms or interior point methods. Simplex algorithms search the corners of the feasible solution area (limited by the constrains) as the solution, if exists, lays on one or more corner points. Interior point methods are more suitable to big optimisation problems and therefore will not be discussed.

Given a luminaire consisting of four: red, green, blue and white colour diodes described by calibration matrix EXAMPLE

$$C = \begin{bmatrix} 60 & 6 & 17 & 74 \\ 25 & 26 & 5 & 77 \\ 0 & 4 & 100 & 92 \end{bmatrix} \tag{4.19}$$

find the maximum luminous flux at $x = 0.25$, $y = 0.25$ colour point. This problem can be solved by linear programming by maximising objective function OBJECTIVE FUNCTION

$$max : F = 25d_1 + 26d_2 + 5d_3 + 77d_4 \tag{4.20}$$

where $d_1 d_4$ are relative intensities of the diodes with respect to their nominal intensities. The coefficients for equation 4.20 are taken from the second row of calibration matrix containing the Y tristimulus values in lumens, and therefore, the luminous flux of the diodes. The solution should be constrained by the feasible CONSTRAINS

relative fluxes of the diodes $0 < d_i < 1$ and the desired output colour point.

$$x = \frac{\sum_i d_i X_i}{\sum_i d_i (X_i + Y_i + Z_i)} \qquad y = \frac{\sum_i d_i Y_i}{\sum_i d_i (X_i + Y_i + Z_i)} \qquad (4.21)$$

Computing first equation yields

$$0.25 = \frac{60d_1 + 6d_2 + 17d_3 + 77d_4}{d_1(60 + 25) + d_2(6 + 26 + 4) + d_3(17 + 5 + 100) + d_4(74 + 77 + 92)}$$

$$0.25 = \frac{60d_1 + 6d_2 + 17d_3 + 77d_4}{85d_1 + 36d_2 + 122d_3 + 243d_4}$$

$$85d_1 + 36d_2 + 122d_3 + 243d_4 = 240d_1 + 24d_2 + 68d_3 + 296d_4$$
$$-155d_1 + 12d_2 + 54d_3 - 53d_4 = 0 \qquad (4.22)$$

and similarly for the second equation

$$-15d_1 - 68d_2 + 102d_3 - 65d_4 = 0 \qquad (4.23)$$

Objective function 4.20 together with the equality constrains eq. 4.22, eq. 4.23 and duty cycle constrains $0 < d_i < 1$ form a linear problem. The solution for this problem is 99.1 lm at $d_1 = 0.0477$, $d_2 = 0.5336$ and $d_3 = d_4 = 1$.

Using linear programming to find the maximum output flux of the luminaire at given colour coordinates can be applied to find the limits of the device inside its gamut. Figure 4.15 compares the performance of two luminaires. Considering first system, white diode's colour point lays on the Planckian locus and the point corresponding to red, green and blue diode driven at maximal current lays below black-body locus. Therefore when all diodes are driven with maximum current the colour point will lay between these two points, under the Planckian locus. When generation of white light needs to be optimised, the colour point of summary of red, green and blue diodes should be as close to the locus as possible. In order to do this, the number of green diodes has been increased by a factor of 2.5× to form a second system.

The cross section of maximum flux plots across black-body locus is shown in figure 4.16. In the case of first system, the green diodes are clearly the limiting factor, as they are driven at their maximum luminance across all colour temperatures of the output light. Increased number of green diodes yields increased maximal flux in colour temperature range from around 2000 K to 10000 K while increasing the number of blue diodes would not change anything.
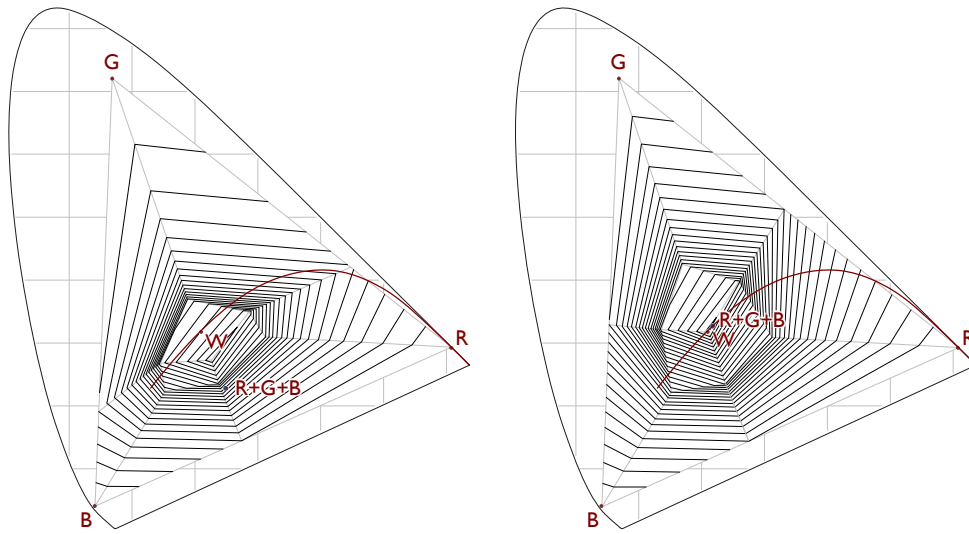
Figure 4.15: Comparison of maximum flux achievable by luminaires. Contour plotted every 5 lm. Left lumanaire described by calibration matrix 4.19. Right luminaire has increased number of green diodes.
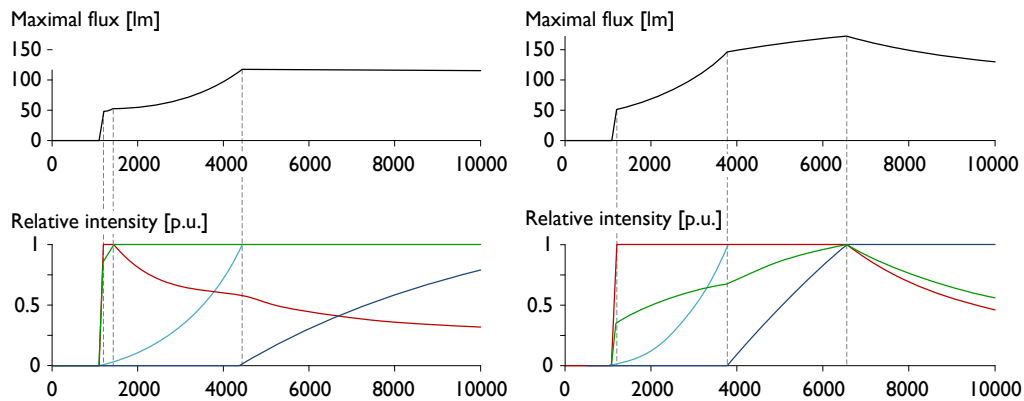

Figure 4.16: Maximum luminous flux for white light with various colour temperatures [K]. Left graphs show the system defined by calibration matrix 4.19. Maximum flux for 6500 K white light is 115.2 lm. By increasing the number of green diodes by the factor of 2.5× (right graphs) the flux at the same colour point increases to 171.6 lm. Zero luminous flux indicates that the desired colour point lays outside gamut of the luminaire.

4.2.2 Optimal control using hybrid dimming

Increasing the number of control variable yields a possibility of increased control of a trichromatic LED luminaire. An experiment was conducted in order to test

83

the gains from hybrid dimming. A red, green and blue diode were chosen as this combination is most commonly present in trichromatic luminaires. Diodes' tristimulus values and electrical quantities were measured and fitted to a polynomial (figure 3.26). This data represents every achievable colour point for each of the diodes. For simplicity constant heatsink temperature was used during data acquisition.

Maximising luminous efficacy (lm/w) means minimising the input power for given flux level.

$$\text{maximise:} f(d_n, I_{peak,n}) = \sum_n P_n, \qquad n = \{\text{r, g, b}\} \qquad (4.24)$$

subject to

$$X = \sum_n X_n, \qquad Y = \sum_n Y_n, \qquad Z = \sum_n Z_n$$
$$0 < I_{peak,min} < I_{peak,n} < I_{f,n,max} \qquad\qquad (4.25)$$
$$0 < d_{min} < d_n < 1$$

Simulations (figure 4.17) show an increase in luminous efficacy in hybrid case compared to both PWM and AM. The increase depends on the value of the flux. The lower the flux value the more gain from the hybrid dimming approach.
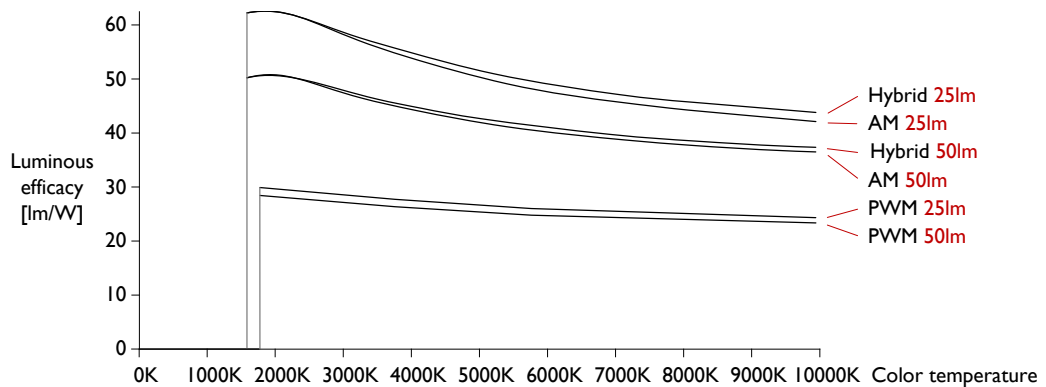

Figure 4.17: Luminous efficacy of hybrid, PWM and AM dimmed luminaires. Efficacies calculated for colour point laying on a blackbody locus for 25 and 50 lumens. Zero efficacy means that this the colour point of this colour temperature cannot be generated by this luminaire.

Another possibility of optimisation is the maximisation of the luminous flux. An interior-point search algorithm was used to find a maximum flux value for a given x, y pairs. Using the same model three dimming approaches were compared. By setting the bounds on duty cycle to be equal to 100 % an AM dimmed luminaire was simulated. Similarly when the peak current was forced to nominal current value for these diodes a PWM dimmed luminaire was simulated. The optimisation procedure was run for each dimming technique. The optimisation problem was formulated as a maximisation of luminous flux

$$\text{maximise: } f(d_n, I_{peak,n}) = \sum_n Y_n, \qquad n = \{r, g, b\} \tag{4.26}$$

subject to

$$x = \frac{\sum_n X_n}{\sum_n (X_n + Y_n + Z_n)}, \qquad y = \frac{\sum_n Y_n}{\sum_n (X_n + Y_n + Z_n)}$$

$$0 < I_{peak,min} < I_{peak,n} < I_{f,n,max} \tag{4.27}$$

$$0 < d_{min} < d_n < 1$$

where the $I_{f,n,max}$ is the maximum forward current of the n-th diode. The value of $I_{peak,min}$ is set to 0 or $I_{f,n,max}$ for AM and PWM dimming, respectively. Similarly, the d_{min} variable is set to 0 or 1 for PWM and AM dimming, respectively. For hybrid dimming both variables are set to zero.

Results (fig. 4.18 and 4.19) are plotted as an increase of luminous flux in hybrid dimmed luminaire compared to PWM and AM dimmed luminaire. An increased luminaire gamut the blue-cyan colours is observed in both cases.

Hybrid PWM/AM dimming technique presented in this dissertation is only one variation of current shape that may be used to drive LEDs. Tse et al. [96, 5, 97, 98] proposed using two levels of DC current and alternating between them. Colorimetric benefits of using such a current shape has not yet been studied.
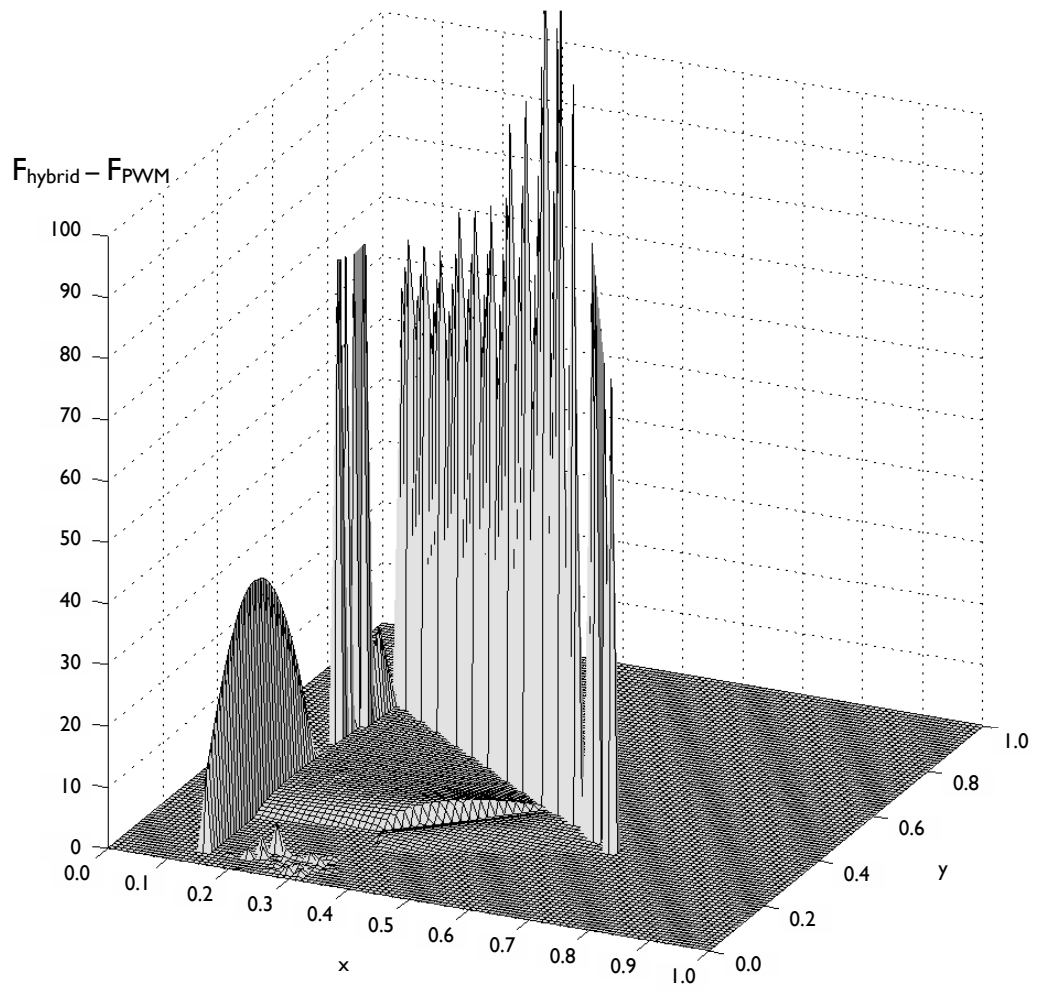
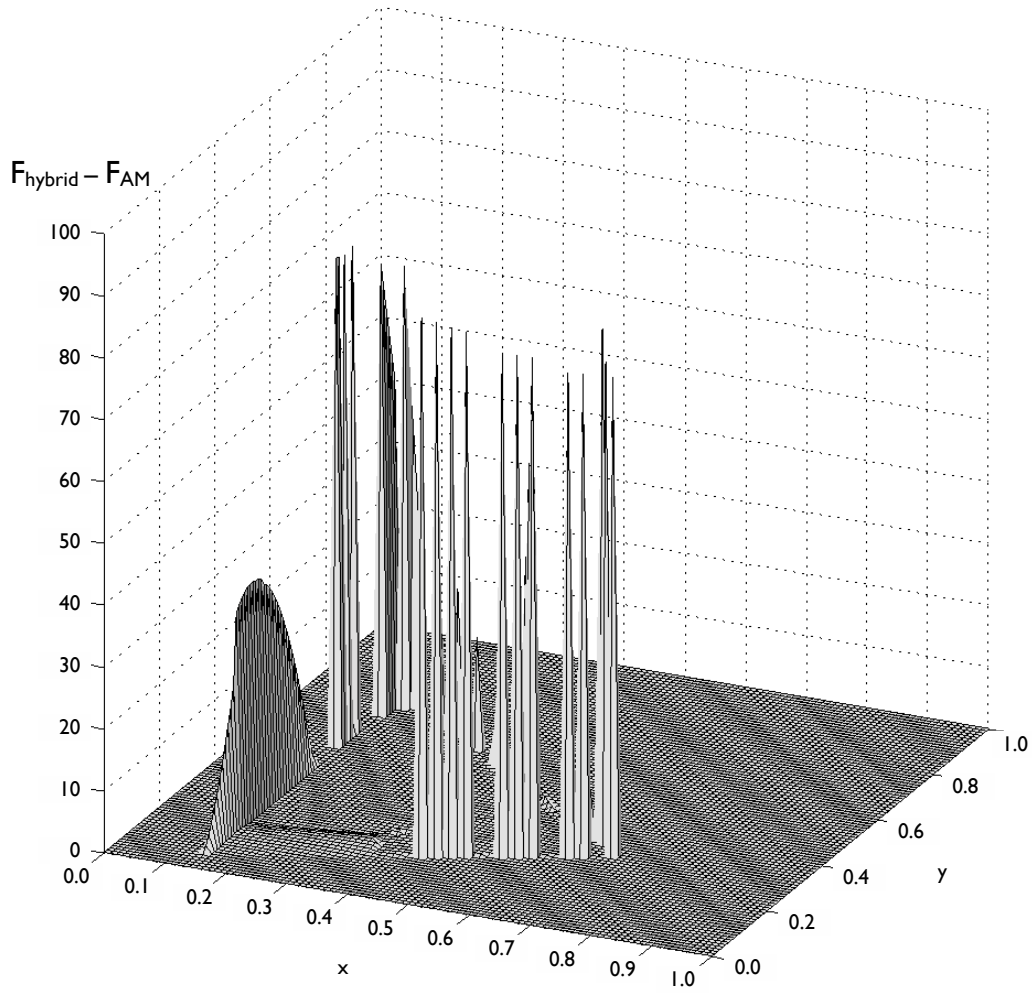Figure 4.18: Increase of the luminous flux in hybrid dimmed luminaire compared to PWM dimmed luminaire.

Figure 4.19: Increase of the luminous flux in hybrid dimmed luminaire compared to AM dimmed luminaire.

5 Power converter

Existing AC diodes that can be directly connected to the electric grid are not powerful enough for projectors and moving head applications. Power electronics circuitry is necessary to convert AC grid power into the form applicable to high power DC LEDs. The structure and complexity of the power electronics converter depends on the power level of installed LEDs and type of the colour control.

All electronic circuitry connected to the utility grid have to meet strict demand on the drawn and injected current. EN 61000-3-2 standard classifies the device by its application and based on this appropriate limits are imposed. EN 61000-3-3 puts a limits on observable light flicker and voltage fluctuations.

In simplest low power applications all diodes can be driven with a single-stage power converter. This ensures low cost of the electronics and simplicity of the design. The drawback of a single stage converter is that the diode control is not fully decoupled from the grid current control. Any disturbance in the grid may be observable in the output light. Therefore this kind of converters are limited to applications where precise light control is not important e.g. street lighting.

Power converters for driving high power, polychromatic luminaires are typically composed of a multi-stage converter, each specialised in its own function. In the simplest form one converter (called a power factor correction stage) is controlling the grid current and keeping the input current spectra within defined standards while a second converter drives the light-emitting diodes.
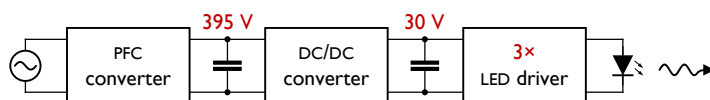

Figure 5.1: Three stages of power conversion from AC grid source to LED load. The DC/DC converter provides galvanic isolation between the grid and the load. Three LED drivers provides power to three: red, green and blue diode strings.

The approach chosen for this project is a three stage power converter (fig. 5.1) where the first PFC stage is an interleaved buck converter with output voltage of 395 V. The role of the second stage, a phase shifted full bridge converter, is to lower the high voltage from the previous stage to a safe 30 V level and to provide galvanic isolation between its input and output. The third stage, described in this chapter, drives the LEDs.

In design process of the LED driver, the two first stages of the power converter are modelled as an ideal voltage source.

The output voltages and currents of the converter are determined by the load. In case of LEDs the current-voltage characteristics is well defined and does not vary much. Also, when using a PWM dimming method, there are only two operating points: when the diode is turned off and when the diode is supplied with nominal current value.
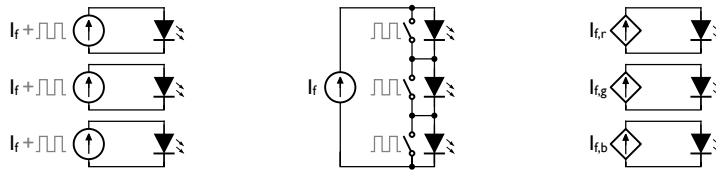

Figure 5.2: Three approaches to dimming of individual diodes in the luminaire. Each colour has a separate driver which has a fixed current value and is controlled by an external PWM intensity control (left). One driver supplies power to all diodes and individual diodes are shorted to create individual intensity control (middle). Each colour of the diodes is driven by a separate driver with an adjustable current (right).

Different dimming schemes may influence the driver design (fig. 5.2). The driver may operate with a fixed current and nearly constant voltage if one driver supplies only one colour string. This if very beneficial because the driver may be optimised only for a single operating point.

If one driver supplies power to all, serial connected diodes in the luminaire, and the diodes are controlled individually by shorting their terminals, the current is fixed to a single value but the voltage changes significantly from zero to the sum of all forward voltages.

Finally, each of the colours in the luminaire can be controlled by a separate DC current source with variable current magnitude. This limits the operating points of the converter to the current-voltage curves of the connected diodes (e.g. fig. 3.8). This approach gives the biggest control opportunities as the current in each diode can be adjusted individually allowing the use of AM, PWM and hybrid dimming schemes.

The last scheme was chosen for implementing in a test luminaire. The highest degree of current control gives the opportunity to test the behaviour of hybrid dimming as well as current-voltage LED model.

The test luminaire was chosen to have three: red, green and blue colour strings, each consisting of four CBT-90 diodes. The typical voltage of a string, at 13.5 A nominal current, had a value of 9.6, 17.2 and 15.6 V for red, green and blue string, respectively. The forward voltage of a single colour diode may vary significantly therefore

the converter should be designed with higher maximum power than predicted with typical forward voltages. The total nominal power of installed LEDs is 572.4 w with string powers: 129.6 w for red, 210.6 w for blue to 232.2 w for green string.

5.2 CONVERTER TOPOLOGIES

Different topologies of power converters may be used to power light-emitting diodes. The difference between topologies include the complexity, control methods, input and output voltages and the shape of input and output waveforms. [37, 105]
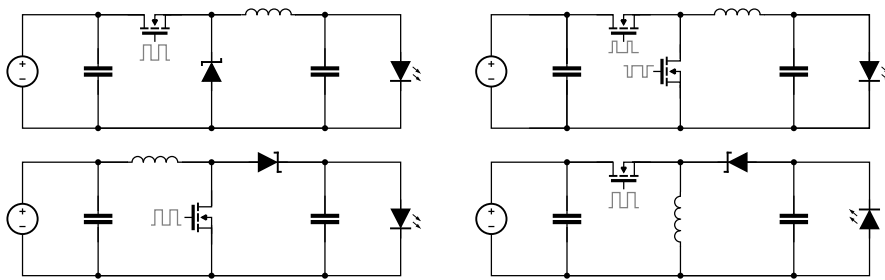

Figure 5.3: Basic DC-DC converters. Buck (top left), synchronous buck (top right), boost (bottom left) and buck-boost (bottom right).

Three basic topologies of DC-DC converters (fig. 5.3) can be created by manipulating a switch cell composed of a transistor, inductor and recirculation diode: buck, boost and buck-boost. The application of one of these converters depends on the input to output voltage ratio of the converter. If output voltage is always lower than input voltage a buck topology can be used, if otherwise, a boost converter can be implemented. Buck-boost topology can be applied to both of the above cases.

For increased efficiency at high current levels, the recirculation diode present in a converter can be replaced with a transistor which is driven opposite to the other transistor. This reduces conduction power losses in the recirculation loop at the expense on increased complexity of the driving circuitry.

Boost topologies require lower voltage on input port than on the load. If the lowest string voltage in the luminaire is 9.6 V, the boost-derived LED drivers would require more than 61 A of current when all diodes are driven with nominal current, not including driver losses.

One of the most important factors when designing a converter for solid-state light sources is the lifetime. Current state of the art diodes can operate for dozen thousands hours maintaining more than 70 % of initial flux. Power converter driving these light sources should have similar lifetime. Electrolytic capacitors are often the cause of failures in switch-mode power converters [106]. It is beneficial therefore, to implement a topology that minimises their use.

High current electrolytic capacitors are used in power converters as filters and energy storage. Typical DC-DC power converter has at least two: input and output capacitors limiting current ripples and providing energy during transients.
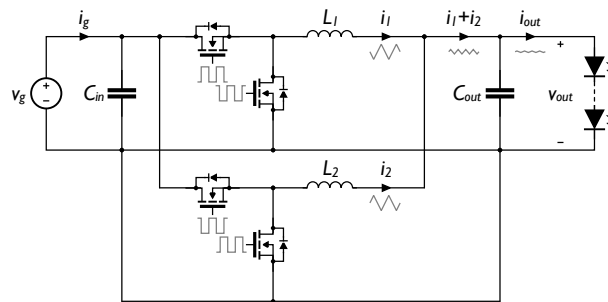
5.3   DUAL INTERLEAVED BUCK TOPOLOGY

Figure 5.4: Schematic of dual interleaved buck topology. 180° phase shift in control signal creates a ripple cancellation effect.

An interleaved buck topology (fig. 5.4) was investigated due to its ripple cancelling properties. When introduced, interleaved buck topology was used extensively in voltage regulation modules (VRMs) for driving CPUs. Benefits of using this topology were: increased dynamic performance, cancellation of output ripple current and spreading the current between multiple phases for easier thermal design [107]. CPUs change the current demand often and require stable supply voltage for stable operation and this requires big values of output capacitances. LEDs on the other hand operate in the working point set by the driver and do not require fast dynamics. It is therefore possible to reduce the output capacitance value to the point where film capacitors can be used instead of electrolytic capacitors.
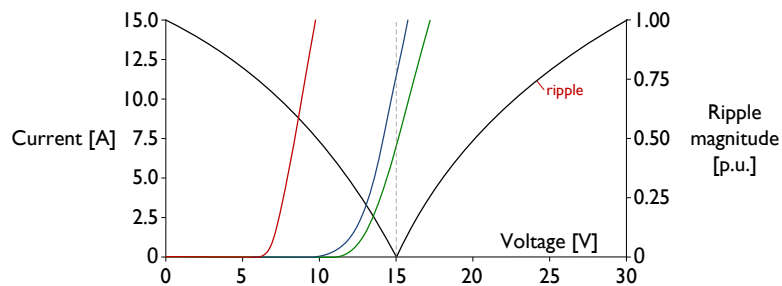

Figure 5.5: Current ripple magnitude with respect to output voltage ($V_g = 30$ V) superimposed on current-voltage characteristics of red, green and blue strings of four, series connected CBT-90 diodes.

Ripple cancellation effect is strongest at duty cycle equal to 0.5 as shown in figure 5.4 [108]. The input voltage for the converter was fixed to 30 v so that the working point for the converter lays close to the half of the input voltage.

5.4 SMALL-SIGNAL MODEL

In order to design a controller, first a small-signal model of the converter is created. Small-signal model averages the signals over the switching period and models the change of electrical quantities disregarding switching ripple [105]. This way the dynamics of signal variations can be easily modelled.

Two buck structures can be modelled independently and, using a superposition principle, connected together. When the upper switch is turned on, the inductor current is equal to the current drawn from the input source. When the top switch of the converter phase is off, the input source current is equal to zero.

$$i_g(t) = i_1 \text{ during } d_1 \tag{5.1}$$

$$i_g(t) = 0 \text{ during } 1 - d_1 \tag{5.2}$$

Applying small-ripple approximation we obtain

$$i_g(t) \approx \langle i_1 \rangle_{T_s} \text{ during } d_1 \tag{5.3}$$

$$i_g(t) = 0 \text{ during } 1 - d_1 \tag{5.4}$$

Similarly, for the other phase

$$i_g(t) = i_2 \text{ during } d_2 \tag{5.5}$$

$$i_g(t) = 0 \text{ during } 1 - d_2 \tag{5.6}$$

Small-ripple approximation yields

$$i_g(t) \approx \langle i_2 \rangle_{T_s} \text{ during } d_2 \tag{5.7}$$

$$i_g(t) = 0 \text{ during } 1 - d_2 \tag{5.8}$$

Equations 5.3, 5.4, 5.7 and 5.8 yield, on average over switching period, input current equal to

$$\langle i_g \rangle_{T_s} = d_1 \langle i_1 \rangle_{T_s} + d_2 \langle i_2 \rangle_{T_s} \tag{5.9}$$

Similar procedure can be applied to output capacitor voltage and inductor currents

yielding following equations

$$C\frac{\mathrm{d}\langle v_c\rangle_{T_s}}{\mathrm{d}t} = \langle i_1\rangle_{T_s} + \langle i_2\rangle_{T_s} - \frac{\langle v_c\rangle_{T_s} - \langle v_f\rangle_{T_s}}{R_d} \tag{5.10}$$

$$L_1\frac{\mathrm{d}\langle i_1\rangle_{T_s}}{\mathrm{d}t} = d_1(t)\langle v_g\rangle_{T_s} - \langle v_c\rangle_{T_s} \tag{5.11}$$

$$L_2\frac{\mathrm{d}\langle i_2\rangle_{T_s}}{\mathrm{d}t} = d_2(t)\langle v_g\rangle_{T_s} - \langle v_c\rangle_{T_s} \tag{5.12}$$

The nonlinear equations describing the converter have to be perturbed and linearised in order to extract the small-signal AC equations. All state variables and inputs to the converter are expressed as quiescent values with superimposed AC variation.

$$\begin{aligned}
\langle v_g\rangle_{T_s} &= V_g + \widetilde{v}_1(t) \\
\langle v_f\rangle_{T_s} &= V_f + \widetilde{v}_f(t) \\
d_1(t) &= D_1 + \widetilde{d}_1(t) \\
d_2(t) &= D_2 + \widetilde{d}_2(t) \\
\langle v_c\rangle_{T_s} &= V_c + \widetilde{v}_c(t) \\
\langle i_1\rangle_{T_s} &= I_1 + \widetilde{i}_1(t) \\
\langle i_2\rangle_{T_s} &= I_2 + \widetilde{i}_2(t)
\end{aligned} \tag{5.13}$$

Substituting above equations into input gate equation yields

$$I_g + \widetilde{i}_g(t) = \left(D_1 + \widetilde{d}_1(t)\right)\left(I_1 + \widetilde{i}_1(t)\right) + \left(D_2 + \widetilde{d}_2(t)\right)\left(I_2 + \widetilde{i}_2(t)\right)$$

$$I_g + \widetilde{i}_g(t) = \underbrace{D_1 I_1 + D_2 I_2}_{\text{DC terms}} + \underbrace{D_1\widetilde{i}_1(t) + D_2\widetilde{i}_2(t) + I_i\widetilde{d}_1(t) + I_2\widetilde{d}_2(t)}_{\text{I-order linear terms}} +$$

$$+ \underbrace{\widetilde{d}_1(t)\widetilde{i}_1(t) + \widetilde{d}_2(t)\widetilde{i}_2(t)}_{\text{II-order nonlinear terms}} \tag{5.14}$$

This equation contains three types of terms: DC, time-invariant terms, first order AC terms and second order AC terms. If small signal assumptions are satisfied then the magnitude of second order terms is much lower than other terms and can be therefore neglected. Separation of DC and AC terms yields two set of equations

$$I_g = D_1 I_1 + D_2 I_2 \tag{5.15}$$

$$\widetilde{i}_g(t) = D_1\widetilde{i}_1(t) + D_2\widetilde{i}_2(t) + I_i\widetilde{d}_1(t) + I_2\widetilde{d}_2(t) \tag{5.16}$$

Applying perturbations to L_1 inductor equation one obtains

$$L_1 \frac{\mathrm{d}\left(I_1 + \widetilde{i_1}(t)\right)}{\mathrm{d}t} = \left(D_1 + \widetilde{d_1}(t)\right)\left(V_g + \widetilde{v_1}(t)\right) - \left(V_c + \widetilde{v_c}(t)\right)$$

$$L_1 \left(\frac{\mathrm{d}I_1}{\mathrm{d}t} + \frac{\mathrm{d}\widetilde{i_1}(t)}{\mathrm{d}t}\right) = D_1 V_g + D_1 \widetilde{v_g}(t) + V_g \widetilde{d_1}(t) + \widetilde{d_1}(t)\widetilde{v_g}(t) - V_c - \widetilde{v_c}(t)$$

$$L_1 \frac{\mathrm{d}I_1}{\mathrm{d}t} + L_1 \frac{\mathrm{d}\widetilde{i_1}(t)}{\mathrm{d}t} = \underbrace{D_1 V_g - V_c}_{\text{DC terms}} + \underbrace{D_1 \widetilde{v_g}(t) + V_g \widetilde{d_1}(t) - \widetilde{v_c}(t)}_{\text{I-order linear terms}} + \underbrace{\widetilde{d_1}(t)\widetilde{v_g}(t)}_{\text{II-order nonlinear terms}}$$

$$\text{(5.17)}$$

Again, the second-order nonlinear terms are omitted and the terms are separated

$$0 = D_1 V_g - V_c \tag{5.18}$$

$$L_1 \frac{\mathrm{d}\widetilde{i_1}}{\mathrm{d}t} = D_1 \widetilde{v_g}(t) + V_g \widetilde{d_1}(t) - \widetilde{v_c}(t) \tag{5.19}$$

Similar procedure can be applied to L_2 inductor equation yielding

$$0 = D_2 V_g - V_c \tag{5.20}$$

$$L_2 \frac{\mathrm{d}\widetilde{i_2}}{\mathrm{d}t} = D_2 \widetilde{v_g}(t) + V_g \widetilde{d_2}(t) - \widetilde{v_c}(t) \tag{5.21}$$

Finally, the output capacitor equation is perturbed.

$$C \frac{\mathrm{d}\left(V_c + \widetilde{v_c}(t)\right)}{\mathrm{d}t} = \left(I_1 + \widetilde{i_1}(t)\right) + \left(I_2 + \widetilde{i_2}(t)\right) - \frac{\left(V_c + \widetilde{v_c}(t)\right) - \left(V_f + \widetilde{v_f}(t)\right)}{R_d}$$

$$C \frac{\mathrm{d}V_c}{\mathrm{d}t} + C \frac{\mathrm{d}\widetilde{v_c}(t)}{\mathrm{d}t} = \underbrace{I_1 + I_2 - \frac{V_c - V_f}{R_d}}_{\text{DC terms}} + \underbrace{\widetilde{i_1}(t) + \widetilde{i_2}(t) - \frac{\widetilde{v_c} - \widetilde{v_f}}{R_d}}_{\text{I-order linear terms}} \tag{5.22}$$

The DC and AC terms are separated with the omission of nonlinear terms.

$$0 = I_1 + I_2 - \frac{V_c - V_f}{R_d} \tag{5.23}$$

$$C \frac{\mathrm{d}\widetilde{v_c}}{\mathrm{d}t} = \widetilde{i_1}(t) + \widetilde{i_2}(t) - \frac{\widetilde{v_c}(t) - \widetilde{v_f}(t)}{R_d} \tag{5.24}$$

The DC equations extracted in the procedure (5.15, 5.18, 5.20 and 5.23) collected

below are used to calculate the quiescent operating point of the converter

$$I_g = D_1 I_1 + D_2 I_2$$
$$0 = D_1 V_g - V_c$$
$$0 = D_2 V_g - V_c \tag{5.25}$$
$$0 = I_1 + I_2 - \frac{V_c - V_f}{R_d}$$

Upon finding the quiescent values of all the variables, the results are inserted into small-signal AC equations (5.16, 5.19, 5.21 and 5.24) collected below

$$\widetilde{i_g}(t) = D_1 \widetilde{i_1}(t) + D_2 \widetilde{i_2}(t) + I_i \widetilde{d_1}(t) + I_2 \widetilde{d_2}(t)$$
$$L_1 \frac{d\widetilde{i_1}}{dt} = D_1 \widetilde{v_g}(t) + V_g \widetilde{d_1}(t) - \widetilde{v_c}(t) \tag{5.26}$$
$$L_2 \frac{d\widetilde{i_2}}{dt} = D_2 \widetilde{v_g}(t) + V_g \widetilde{d_2}(t) - \widetilde{v_c}(t)$$
$$C \frac{d\widetilde{v_c}}{dt} = \widetilde{i_1}(t) + \widetilde{i_2}(t) - \frac{\widetilde{v_c}(t) - \widetilde{v_f}(t)}{R_d}$$
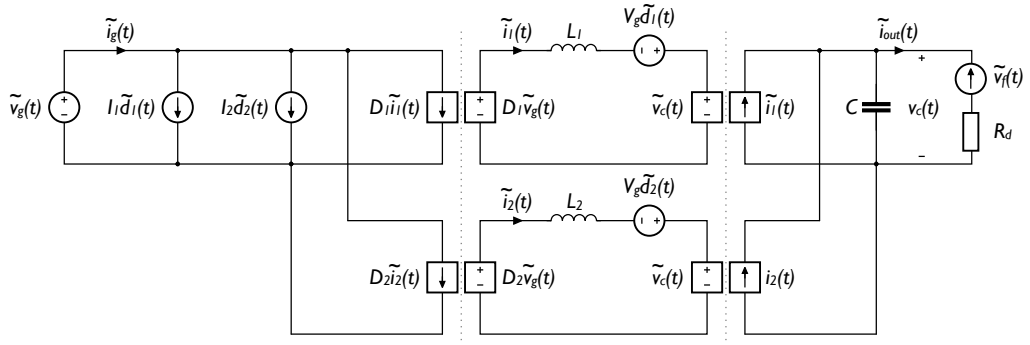

Figure 5.6: Circuits equivalent to the small-signal converter equations: (left) input port, inductor loops, (right) capacitor node.

The digital average current controller, chosen for this converter will control the phase current, regulating it, by varying the input duty cycle. Appropriate converter transfer functions must be analysed to design the dynamics of the controller.

$$\widetilde{i_1}(s) = G_{i_1 d_1} \widetilde{d_1}(s) + G_{i_1 d_2} \widetilde{d_2}(s) + G_{i_1 v_g} \widetilde{v_g}(s) \tag{5.27}$$

First summand in the above equation corresponds to the impact of control signal on the phase current. Second term corresponds to the effect of the duty cycle variation in one phase on the inductor current in the other phase. This corresponds to
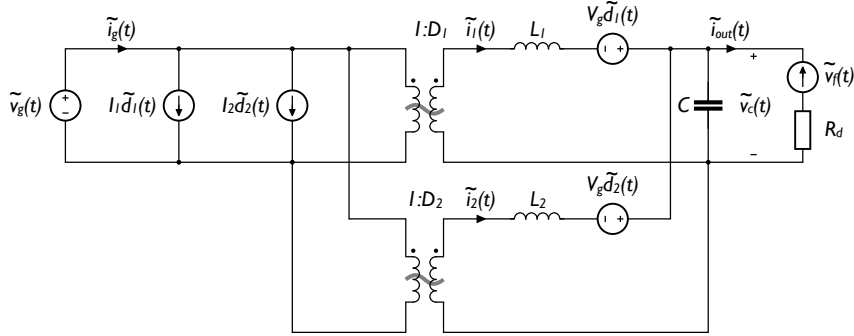
Figure 5.7: Complete small-signal AC equivalent circuit model of an ideal two phase, inter-leaved buck converter.

the circulating current in the converter. Last term in the summation is the effect of variation in the input voltage on the inductor current and is treated as an external disturbance.

Control to inductor current transfer function is calculated assuming all other input variations are equal to zero:

$$G_{i_1 d_1}(s) = \left.\frac{\widetilde{i_1}(s)}{\widetilde{d_1}(s)}\right|_{\widetilde{d_2}(s)=0,\ \widetilde{v}_g(s)=0} \tag{5.28}$$
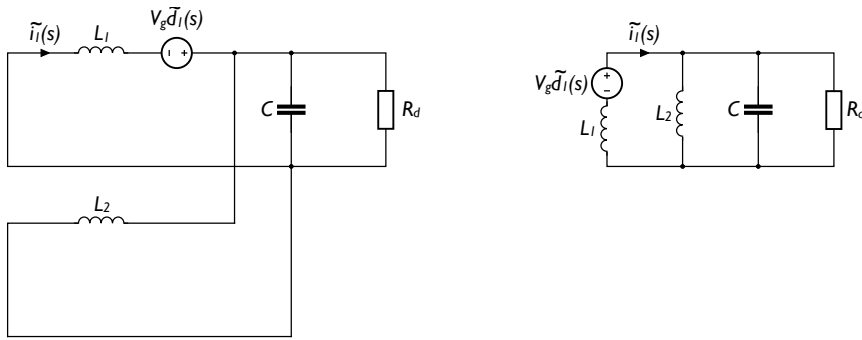

Figure 5.8: Manipulation of equivalent circuit of the interleaved buck converter to find the $G_{i_1 d_1}(s)$ control to output transfer function.

Because of the assumption $\widetilde{v}_g(s) = 0$, the transformers in the converter model (fig. 5.7) are shorted and the circuit can be manipulated into the final form, shown in figure 5.8.

The inductor current $\widetilde{i_1}(s)$ can be calculated as

$$\widetilde{i_1}(s) = \frac{1}{sL_1 + \left(R_d \middle\| sL_2 \middle\| \frac{1}{sC}\right)} V_g \widetilde{d_1}(s) \tag{5.29}$$

97

therefore the control to inductor current transfer function is equal to

$$G_{i_1 d_1}(s) = \frac{\widetilde{i_1}(s)}{\widetilde{d_1}(s)} = V_g \frac{1}{sL_1 + \frac{sR_dL_2}{s^2R_dL_2C+sL_2+R_d}} = V_g \frac{1}{\frac{sR_dL_2+s^3R_dL_1L_2C+s^2L_1L_2+sR_dL_1}{s^2R_dL_2C+sL_2+R_d}} =$$

$$= V_g \frac{s^2R_dL_2C + sL_2 + R_d}{s^3R_dL_1L_2C + s^2L_1L_2 + sR_d(L_1+L_2)} =$$

$$= V_g \frac{s^2\left(\frac{L_2}{L_1+L_2}\right)C + s\frac{1}{R_d}\left(\frac{L_2}{L_1+L_2}\right) + \left(\frac{1}{L_1+L_2}\right)}{s^2\left(\frac{L_1L_2}{L_1+L_2}\right)C + s\frac{1}{R_d}\left(\frac{L_1L_2}{L_1+L_2}\right) + s} \tag{5.30}$$

Noting the parallel connection of the inductors using following form

$$\left(\frac{L_1L_2}{L_1+L_2}\right) = \left(L_1\|L_2\right) \tag{5.31}$$

we obtain the final transfer function

$$G_{i_1 d_1}(s) = V_g \left(\frac{L_2}{L_1+L_2}\right) \frac{s^2C + s\frac{1}{R_d} + \frac{1}{L_2}}{s^3\left(L_1\|L_2\right)C + s^2\frac{1}{R_d}\left(L_1\|L_2\right) + s} \tag{5.32}$$

Control to other phase inductor current transfer function is equal to the current variation in one phase to the duty cycle variation in the other phase:

$$G_{i_1 d_2}(s) = \left.\frac{\widetilde{i_1}(s)}{\widetilde{d_2}(s)}\right|_{\widetilde{d_1}(s)=0,\ \widetilde{v_g}(s)=0} \tag{5.33}$$

Manipulation of the basic model of the converter, similarly as for the previous transfer function, yields a simplified model shown in figure 5.9.
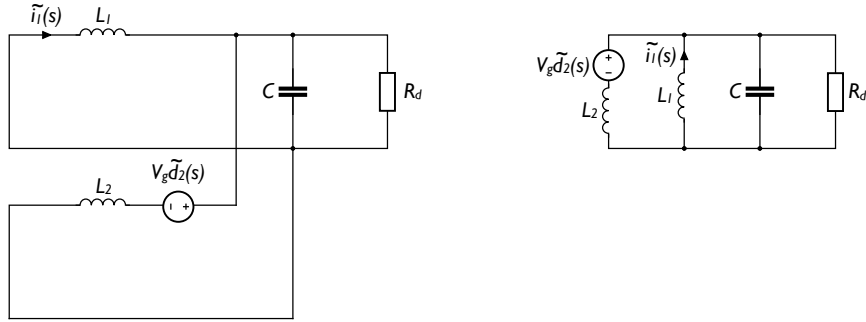

Figure 5.9: Manipulation of equivalent circuit of the interleaved buck converter to find the $G_{i_1 d_2}(s)$ control to output transfer function.

The capacitor voltage can be expressed as

$$v_c = \frac{\left(R_d\|sL_1\|\frac{1}{sC}\right)}{sL_2 + \left(R_d\|sL_1\|\frac{1}{sC}\right)} V_g \widetilde{d_2}(s) \tag{5.34}$$

98

while the $\widetilde{i_1}(s)$ current is equal to

$$\widetilde{i_1}(s) = \frac{-v_c}{sL_1} \tag{5.35}$$

and the transfer function can be calculated according to following equations

$$
\begin{aligned}
G_{i_1 d_2}(s) = \frac{\widetilde{i_1}(s)}{\widetilde{d_2}(s)} &= \frac{-V_g \frac{R_d}{s^2 R_d L_1 C + s L_1 + R_d}}{sL_2 + \frac{s R_d L_1}{s^2 R_d L_1 C + s L_1 + R_d}} = \frac{-V_g R_d}{sL_2 (s^2 R_d L_1 C + s L_1 + R_d) + s R_d L_1} = \\
&= \frac{-V_g}{s^3 L_1 L_2 C + s^2 \frac{1}{R_d} L_1 L_2 + s(L_1 + L_2)} = \\
&= -V_g \left(\frac{1}{L_1 + L_2} \right) \cdot \frac{1}{s^3 \left(L_1 \| L_2\right) C + s^2 \frac{1}{R_d} \left(L_1 \| L_2\right) + s} \tag{5.36}
\end{aligned}
$$

The input voltage to inductor current will not be resolved symbolically due to much higher complexity.

All transfer function shown above behave like integrators because the parasitic resistances were omitted in the modelling. Adding these resistances will change the transfer functions so that they will have finite DC response.
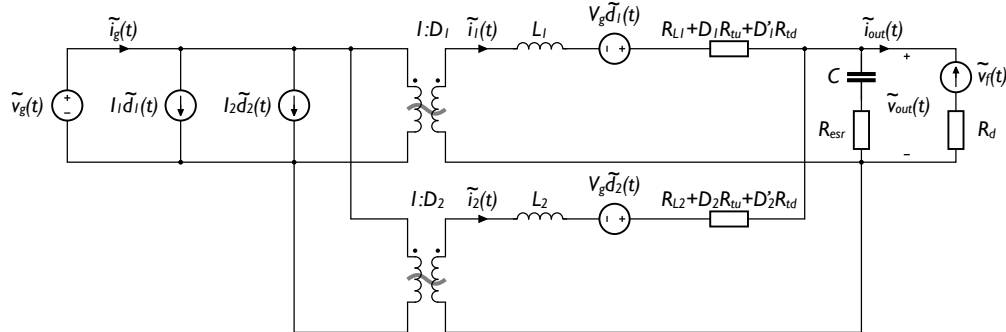

Figure 5.10: Complete small-signal AC equivalent circuit model of an nonideal two phase, interleaved buck converter. Includes conduction losses in transistors (R_{tu} and R_{td}—drain-source resistance of upper and lower transistor, respectively), inductors (R_{L1} and R_{L2}) and in output capacitor (R_{esr}).
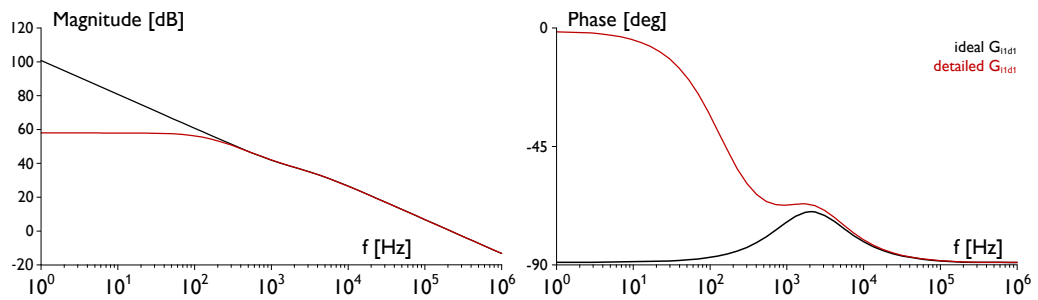
Figure 5.11: Ideal and detailed (including parasitic resistances) $G_{i_1 d_1}(s)$ transfer function of the LED driver.
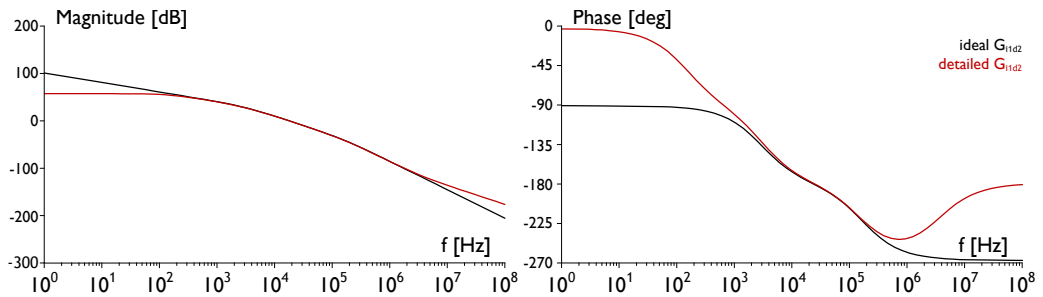

Figure 5.12: Ideal and detailed (including parasitic resistances) $G_{i_1 d_2}(s)$ transfer function of the LED driver.

5.5 CONTROLLER DESIGN

The obtained transfer functions $G_{i_1 d_1}(s)$ and $G_{i_1 d_2}(s)$ are further discretised using a Tustin transform, because this method preserves the stability of the system [109]. A
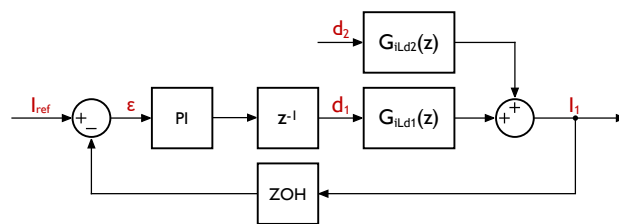

Figure 5.13: Current control loop in z domain.

model of the control system is then created in z domain, as shown in figure 5.13. PI controller parameters were tuned to obtain stable response. The colour control loop runs much lower than the current control loop, therefore the current controller does not need very high bandwidth.
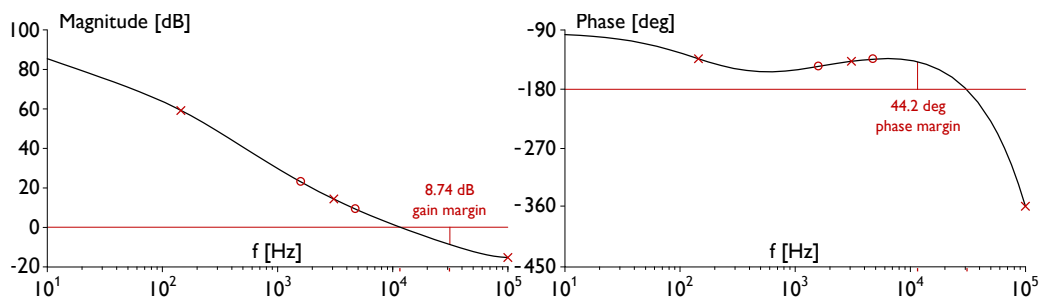
Figure 5.14: Open loop bode plots of the control system showing the stability of the design.

5.6 CURRENT MEASUREMENT

Current sensing is required in the feedback loop for both current mode control and over-current protection of diodes. It is important that the measurement technique is fast, accurate, lossless and immune to switching noise. The dynamics of the current measurement affects the dynamics of the current control loop.
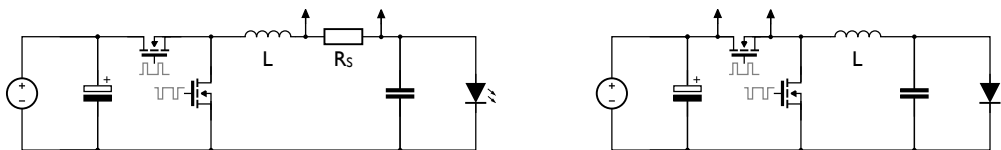
Figure 5.15: Current measurement by adding series measurement resistor R_s (left) and using transistor $R_{ds(on)}$ resistance (right).

5.6.1 Current sensing resistor

Most basic current measurement technique is adding a series resistor and measuring the voltage across it (fig. 5.15a). This method is very accurate as high precision resistor, with small tolerance and low temperature coefficient, can be used. The drawback is, that in order to obtain reasonably high voltage signal (above 100 mV), a resistor with resistance $R_s > 100\text{mV}/i$ has to be used. The higher the resistance the bigger the losses

$$p_{loss} = R_s i^2. \tag{5.37}$$

For example, a 1 A current sensor will need minimum 100 mΩ resistor dissipating 100 mW. A 10 A current sensor needs only 10 mΩ resistor that will dissipate 1 w of power. Low value sensing resistors can be manufactured as a fixed length track on a converter PCB.

Placement of the sense resistor influences both conditioning circuit and protection against short circuit. Placing the circuit in the return path of the current produces a ground referenced measurement but also increases the load potential with respect to the ground. LED die is typically electrically isolated from its heatsink therefore this method can be used.

Sensor connected in series with the inductor provides constant current monitoring and load short circuit protection but it is the least efficient solution. It will not detect any short circuit through both transistors. The measurement has high common mode voltage dependent on the output voltage.

Connecting the sensor in series with high side transistor provides very good short circuit protection and is typically used in peak current controlled converters. Losses depend on both output current and duty cycle of the converter therefore this placement is best used in low duty cycle buck converters. Differential voltage measurement with high common mode voltage is necessary.

5.6.2 MOSFET *drain-source resistance*

Instead of using an added resistor, a parasitic resistance already present in the circuit can be used (fig. 5.15b) [110]. The drain-source resistance of a open MOSFET can be used. This technique is considered as lossless as it does not introduce any additional losses apart from conduction losses of the transistor. When transistor is on, the value of the drain current is given by

$$ i_D = \frac{v_{sense}}{R_{DS(on)}}. \tag{5.38} $$

Again, the minimum $R_{DS(on)}$ resistance depends on the measured current level. By using this technique one may be forced to use worse transistor than available in the current state of the art market. Another drawback is the $R_{DS(on)}$ tolerance reaching 30–40% [111]. Datasheets typically provide the typical and maximum value of the resistance. An additional calibration circuit can be introduced to overcome this problem. The on resistance depends also strongly on the temperature and is sensitive to low V_{GS} voltage [110].

5.6.3 *Inductor* DCR

Instead of using MOSFET's on resistance a scheme based on measuring inductor DC resistance can be implemented [111]. Additional RC network has to be added to estimate the current in the inductor. The current is given by the Ohm law in s-domain

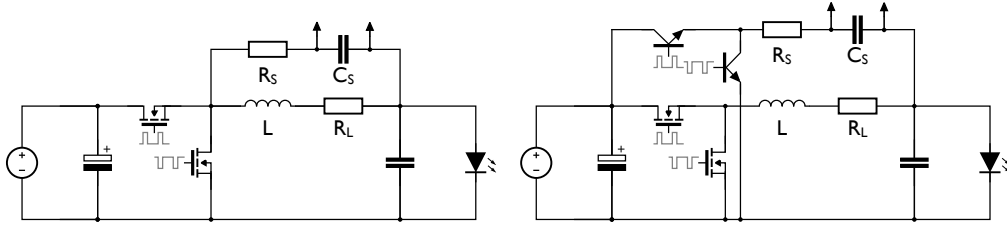$$ I_L = \frac{V_L}{R_L + sL} \tag{5.39} $$

Figure 5.16: Current measurement by inductor DCR current sensing (left) and improved inductor DCR current sensing (right).

where V_L is the voltage on the terminals of the inductor and R_L is the inductors DC resistance. The auxiliary R_s, C_s network forms a voltage divider.

$$V_C = \frac{1/sC_s}{R_s + 1/sC_s} V_L \tag{5.40}$$

$$V_C = \frac{1}{1 + sR_sC_s} V_L \tag{5.41}$$

$$V_L = (1 + sR_sC_s) V_C \tag{5.42}$$

Substituting the result to equation 5.39 yields

$$I_L = \frac{(1 + sR_sC_s)}{R_L + sL} V_C \tag{5.43}$$

$$I_L = \frac{1}{R_L} \left(\frac{1 + sR_sC_s}{1 + s\frac{L}{R_L}} \right) V_C \tag{5.44}$$

$$I_L = \frac{1}{R_L} \left(\frac{1 + s\tau_{RC}}{1 + s\tau_{RL}} \right) V_C \tag{5.45}$$

When both time constants are equal

$$\tau_{RC} = \tau_{RL} \Rightarrow R_sC_s = \frac{L}{R_L} \tag{5.46}$$

voltage on the capacitor C_s is proportional to inductor current

$$I_L = \frac{V_C}{R_L}. \tag{5.47}$$

However, the above equation is only true when the elements are well matched (eq. 5.46). Because of the high tolerance of inductive and capacitive components and dependence of L on the DC bias this condition is hard to satisfy.

5.6.4   Inductor DCR with improved signal-to-noise ratio

Signal voltage in the inductor DCR method depends on the series resistance of an inductor. If it is too small, the output signal will be susceptible to the interruption of noise. To increase signal to noise ratio (SNR) a change in the measuring circuit (fig. 5.16b) has been proposed [112]. Additional transistors drive the measuring RC network. Measured signal includes the resistance of the inductor and $R_{DS(on)}$ of the transistor. This increases the signal by a factor of $(R_{DS(on)} + R_L)/R_L$.
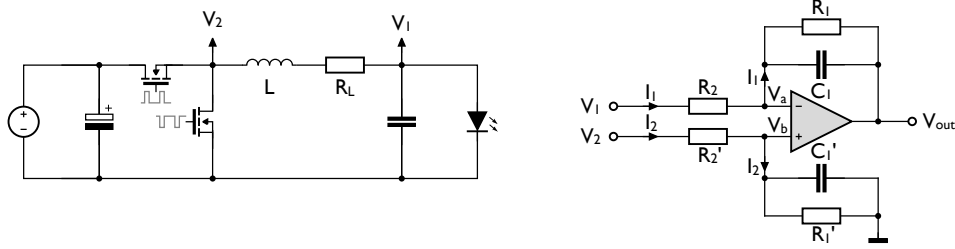

Figure 5.17: Schematic of current sensing circuit using a differential amplifier. For proper operation $R_1 = R_1'$, $R_2 = R_2'$ and $C_1 = C_1'$ must be used.

5.6.5   Improved inductor DCR

Two previous inductor DCR measurement methods require high value of inductor resistance so that the measured signal has sufficient magnitude. On the other hand efficiency requirement calls for the lowest possible resistance. It is however possible to create a measurement circuit that does not have this drawback using a single differential amplifier with impedances matched to inductor's time constant [113]. The schematic of this current measurement scheme is shown in figure 5.17. Impedance of paralleled R_1 and C_1 is equal to

$$Z_{RC} = \frac{R_1}{1 + sR_1C_1}. \tag{5.48}$$

Currents flowing in and out V_a and V_b nodes are calculated as follows

$$I_1 = \frac{V_1 - V_a}{R_2} \qquad I_1' = \frac{V_a - V_{out}}{Z_{RC}} \qquad I_2 = \frac{V_2 - V_b}{R_2} \qquad I_2' = \frac{V_b}{Z_{RC}} \tag{5.49}$$

Assuming that amplifier input currents are negligible one can write $I_1 = I_1'$ and $I_2 = I_2'$. Equations 5.49 can be rewritten as

$$Z_{RC}\left(V_1 - V_a\right) = R_2\left(V_a - V_{out}\right)$$
$$Z_{RC}\left(V_2 - V_b\right) = R_2 V_b$$
$$Z_{RC}\left(V_1 - V_a - V_2 + V_b\right) = R_2\left(V_a - V_b - V_{out}\right) \tag{5.50}$$

Assuming that the gain of amplifier $A \to \infty$ voltages V_a and V_b can be treated as equal $V_a = V_b$ and transfer function of the differential amplifier circuit can be calculated as

$$Z_{RC}\left(V_1 - V_2\right) = -R_2 V_{out}$$
$$Z_{RC} V_{in} = R_2 V_{out}$$
$$\frac{V_{out}}{V_{in}} = \frac{Z}{R_2} \qquad (5.51)$$

Voltage on the inductor is equal to

$$V_L = I_L\left(R_L + sL\right)$$
$$V_L = I_L R_L\left(1 + sL/R_L\right) \qquad (5.52)$$

Current sensing circuit is connected to the terminals of the inductor, therefore substituting eq. 5.48 and 5.52 into equation 5.51 yields

$$\frac{V_{out}}{I_L} = \frac{R_L R_1}{R_2} \cdot \frac{1 + sL/R_L}{1 + sR_1 C_1} \qquad (5.53)$$

When time constants $R_1 C_1$ and L/R_L are equal, eq. 5.53 is simplified to

$$\frac{V_{out}}{I_L} = \frac{R_L R_1}{R_2} \qquad (5.54)$$

Current signal is converted into voltage signal with gain set by the ration of R_1 and R_2 resistors and the series resistance of the inductor. This circuit requires high voltage, high bandwidth amplifier in order to accurately follow inductor current.
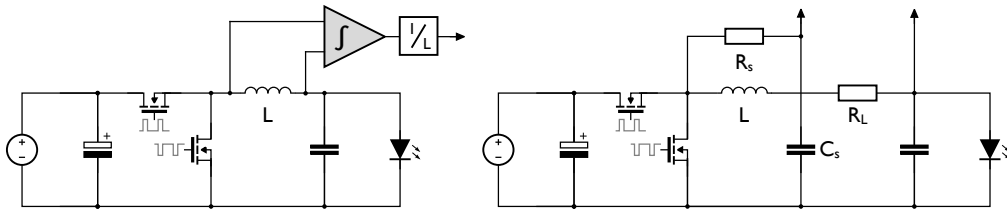

Figure 5.18: Current measurement by observer technique (left) and average current sensing (right).

5.6.6   Observer technique

This technique uses the inductor voltage to calculate the inductor current [114]. As the voltage-current relation of an inductor is given by

$$v_L = L\frac{\mathrm{d}i_L}{\mathrm{d}t}, \qquad (5.55)$$

the inductor current can be calculated by integrating the inductor voltage

$$i_L = \frac{1}{L} \int v_L \mathrm{d}t. \tag{5.56}$$

The inductor voltage is typically much larger signal than the output of a current sensing resistor and depends only on the input voltage.

5.6.7 Average current sensing

Figure 5.18b shows a simple method of measuring the average current in the inductor [43]. An additional RC network is added parallel to the recirculation transistor. Under steady state conditions, the average voltage on resistor R_s is zero therefore average voltage on the inductor can be written as $V_{out} - \langle V_C \rangle$. The average current in the inductor is derived as

$$\langle I_L \rangle = \frac{\langle V_L \rangle}{R_L} = \frac{V_{out} - \langle V_C \rangle}{R_L}. \tag{5.57}$$

For accurate current sensing, the DC resistance of the inductor has to be known. Values of the additional RC filter will affect the measurement bandwidth [115] therefore this technique is mostly applicable to control current sharing between phases in multiphase converters.

5.6.8 Overview

An overview of current measurement schemes is shown in table 5.1. An improved inductor DCR, described in chapter 5.6.5, was chosen for the converter. It uses a single operational amplifier and a tuned RC circuit therefore it is not expensive. Moreover, manufacturers provide inductors with specific tolerances for the DC resistance. The accuracy of the method can therefore be calculated, based on the resistance tolerance.

Table 5.1: Comparison of current measurement schemes.

METHOD	ACCURACY	COMMENTS
current sensing resistor	+++	high losses
MOSFET $R_{DS(on)}$	+	tradeoff between losses and accuracy
inductor DCR	++	complicated signal conditioning, DCR variation
improved inductor DCR	++	DCR variation
observer	+	troublesome long time integration
average current sensing	++	low bandwidth, DCR variation

$V_{in} = 30$ V

$V_{out} = \{9.6, 17.2, 15.6\}$ V   for red, green and blue diode string, respectively

$I_f = 13.5$ A

$I_{phase} = 0.5 \cdot I_f = 6.75$ A

$I_{pp} = 25\,\% \cdot I_{phase} = 1.6875$ A

$f_{sw} = 200$ kHz

5.7.1 Inductor

In order to calculate the necessary inductance value, the inductor voltage equation can be used.

$$v_L = L \frac{\mathrm{d}i_L}{\mathrm{d}t} \tag{5.58}$$

During on phase of the switching period ($d \cdot t_{sw}$) inductor current increases by the value of peak-to-peak ripple current I_{pp} and the voltage on the inductor is equal to $v_{in} - v_{out}$. Rearranging equation 5.58 and substituting appropriate variables yields

$$L = (V_{in} - V_{out}) \cdot \frac{V_{out}}{V_{in} \cdot f_{sw}} \cdot \frac{1}{I_{pp}} \tag{5.59}$$

Calculating above equation yields 19.3 µH for red, 21.7 µH for green and 22.2 µH for blue diode string. A closest 22 µH standard value for inductors was chosen to be used in the converter.

Basing on the DC bias current and required inductance value a 77350-A7 Magnetics core has been chosen for the inductor. Magnetics design calculator was used to design and estimate the power losses of the inductor. 21 turns of 16 AWG wire yields 21.71 µH at full DC current bias. Core losses are estimated at 90 mW. DC resistance of approximately 9 mΩ generates 410 mW copper losses. The total dissipated power is equal to 500 mW per inductor.

5.7.2 Output capacitor

The value of the output capacitor typically is chosen based on the maximum output voltage ripple magnitude and the voltage overshoot during load transient. As the LED is driven by the current, the voltage transients are not important. The output capacitor limits the 400 kHz (twice the switching frequency) ripple current flowing through the load. Therefore the only reason for the output capacitor is the EMI issues creased by the wires connecting the driver to the diodes.

MOSFET   A MOSFET (metal-oxide-semiconductor field-effect transistor) transistors are ideal switches for low voltage applications. When turned on, a channel of n-type or p-type semiconductor is formed between the drain and source terminals. Because of the small on resistance (typically few mΩ) the conduction losses are much lower than in BJT (bipolar junction transistor) experiencing a high voltage drop between output terminals.
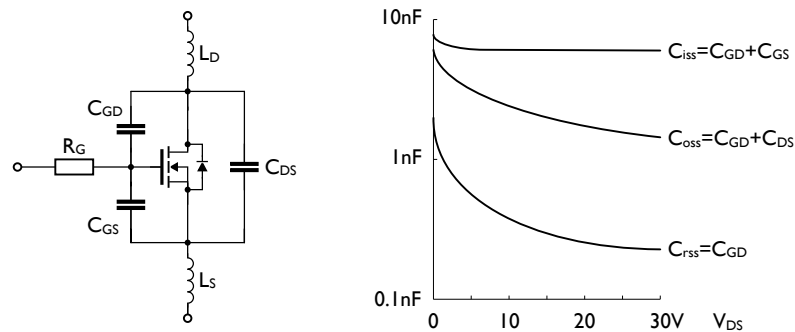

Figure 5.19: Power MOSFET with parasitic components [116]. Nonlinearities of input capacitance C_{iss}, reverse transfer capacitance C_{rss} and output capacitance C_{oss} of IPB80N04S3-03 transistor shown in the function of drain-source voltage.

MOSFET with basic parasitic components is shown in the figure 5.19. Drain and source inductance values depend on transistor package (typically few nH). Internal gate resistance has to be included in the driving loss calculations as its value is typically between 0.5–5 Ω.

LOSSES   There are three power loss mechanisms in the MOSFET. One is conduction losses, when transistor is fully on (fig. 5.20, period t_4–t_7), and power is dissipated in the ohmic channel according to $R_{DS(on)} \cdot i_D^2$ equation. Blocking losses are typically neglected because of very low drain leakage current (for example IPB80N04S3-03 has a 100 μA leakage current at $T_j = 125°C$ which gives 4 mW at $v_{DS} = 40V$). The last mechanism is the switching losses. Due to high complexity, the analysis is broken into specific periods (fig. 5.20).

PERIOD t_1–t_2 Before t_2, the current in the drain is zero and some voltage is present between drain and source. Only negligible blocking losses are present. MOSFET driver is charging the input capacitance C_{iss}. Transistor is in the off state. Gate-source voltage raises linearly (assuming constant current flowing into the gate). This period is defined as a turn-on delay $t_{d(on)}$.

PERIOD t_2–t_3 Gate-source voltage has reached the threshold voltage V_{th} and transistor is starting to conduct current. i_D raises but blocked voltage still remains on the output
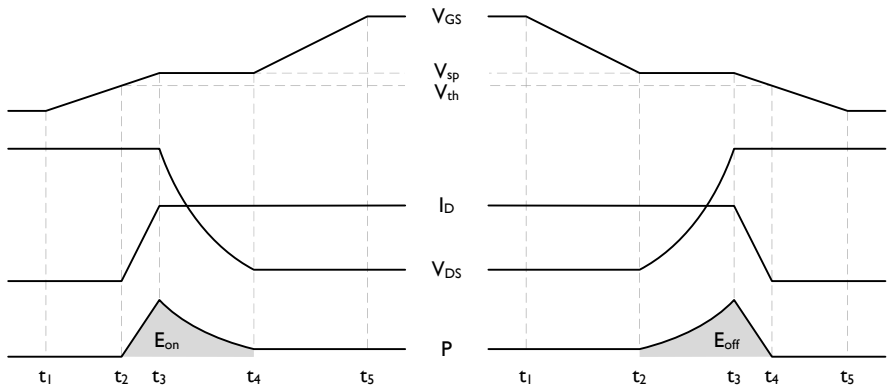
Figure 5.20: Switching waveforms of a power MOSFET during turn on (left) and turn off
(right). V_{GS} gate-source voltage, I_D drain current, V_{DS} drain-source voltage
and P power losses. V_{GS} waveform can be obtained from specific transistor
datasheet (V_{GS} vs. Q_G figure).

terminals. Power is dissipated due to non-zero product of i_D and v_{DS}. Gate-source
voltage continues to raise until it reaches plateau voltage V_{sp}.

C_{GS} is charged and gate current starts to charge C_{GD}. Due to a Miller effect, v_{GS} PERIOD t_3–t_4
is clamped to plateau voltage V_{sp}. Drain-source voltage is decreasing. The rate of
dv_{DS}/dt is dictated by the gate current charging the gate-drain capacitance C_{rss}. As-
suming constant gate current, the drain-source voltage slope is not constant due to
highly non-linear C_{rss} (fig. 5.19). Gate charge $Q_{GS} + Q_{GD}$ is the minimum charge
needed to turn the transistor on. Gate charge value is used to calculate required
gate drive current.

A loss model, based on above description, has been used to estimate the losses in MOSFET
the transistor. The model uses datasheet parameters ($R_{DS(on)}$, C_{oss}, C_{rss}, C_{gs}, R_g, Q_g, COMPARISON
Q_{gd}, V_{Gth} and gfs) to calculate turn on, turn off and conduction losses in the transis-
tors. Table 5.2 shows the loss distribution and the total loss in the device for the top
transistor. A IRLR3636 MOSFET was chosen based on this loss estimation. Losses in

Table 5.2: Losses in the top MOSFET at 6.75 A phase current (half of the nominal 13.5 A diode
current) and 16 V output voltage.

SYMBOL	TURN ON LOSSES [W]	TURN OFF LOSSES [W]	CONDUCTION LOSSES [W]	TOTAL LOSSES [W]
IRFP4321	0.552	0.071	0.409	1.032
SUD23N06	0.103	0.146	1.319	1.568
IRLS3036	0.616	1.164	0.067	1.848
IRLR3705Z	0.199	0.360	0.293	0.853
IRLR3636	0.245	0.400	0.161	0.806

the bottom transistor are dominated by the conduction losses, as the transistor is turning on and off with a diode forward voltage drop across it. The same MOSFET device was chosen due to its low cost and a low $R_{DS(on)}$ value.

5.7.4 Gate circuit

A LM5106 100 V half bridge gate driver with programmable dead-time has been chosen for driving the MOSFETS. The driver needs only one PWM signal to drive two: high and low MOSFETS so that one driver containing two phases requires only two PWM lines.

5.7.5 Current measurement

The improved inductor DCR current measurement method, described in detail in chapter 5.6.5, was chosen for the converter. In the luminaire, each colour diode string is driven with a driver consisting of two buck converters. Each of these converters requires a separate current measurement circuit, therefore the current measurement circuit should be cheap.
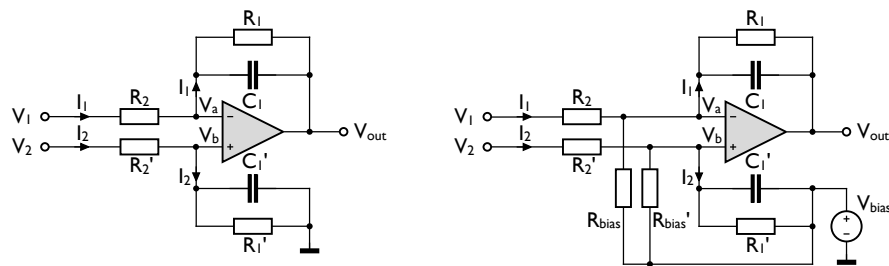

Figure 5.21: Current measurement scheme implemented in the driver. Inductor DCR measurement circuit (left) and improved circuit with biased input and output (right) allows the use of cheap operational amplifiers. Potentials V_1 and V_2 measured across the inductor.

A low cost LM837 operational amplifier was used due to its price, high operating voltage ±18 V and high unity-gain bandwidth of 25 MHz. This amplifier does not have rail-to-rail inputs or outputs, therefore the voltage levels were shifted to an appropriate level using bias voltage (for the output) and additional bias resistors (to bias both inputs) as shown in figure 5.21.

Time constant of the $R_1 C_1$ must be equal to the time constant of the inductor for the current measurement circuit to track the current accurately, as described in chapter 5.6.5. The effects of time constant mismatch can be visible in figure 5.22. Although, the feedback current signal experiences normal step response, the actual current response may be very different.
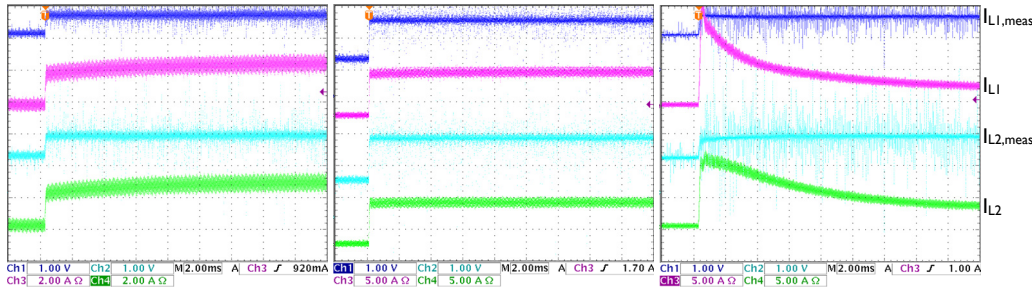
Figure 5.22: Measured effect of difference in $R_1 C_1$ and L/R_L time constants. Measured current $I_{Lx,meas}$ is controlled by the controller. Shape of the actual current depends on the relation of time constants. $R_1 C_1 < L/R_L$ (left), $R_1 C_1$ equal to L/R_L (middle) and $R_1 C_1 > L/R_L$ (right)
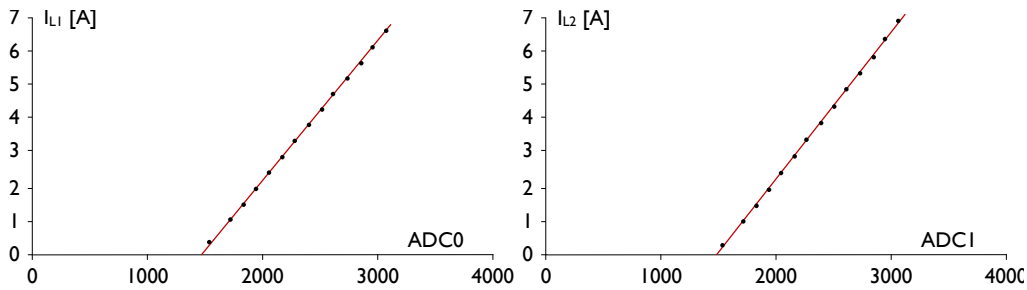

Figure 5.23: Measured linearity of current sensing circuits for each phase of the converter. ADCx values refer to the value of analog to digital conversion in the DSP.

The linearity of the current sensing circuit has been measured in the laboratory (fig. 5.23) showing a linear relationship between actual and measured current in the inductors. For the amplifier gain and bias voltage used in the experiments the achieved current measurement resolution is around 5 mA.

5.8 EXPERIMENTAL RESULTS

The design has been built in the laboratory (fig. 5.24). The converter is controlled using a TMS320F28027 Piccolo microcontroller board. DSP contains four independent PWM modules, each capable of generating two PWM signals with the same carrier waveform. This means that one DSP can control up to four LED drivers. The converter has been tested using a high power LED load shown in figure 5.25.

The dynamic response was tested by performing a step in current command. Results, shown in figure 5.26 show small difference between the model and the real system. Real system shows more damped response with little overshot. This phenomenon may be explained by lack of detailed modelling of all parasitic effects e.g. inductance change with the DC current value or switching losses in the transistors.
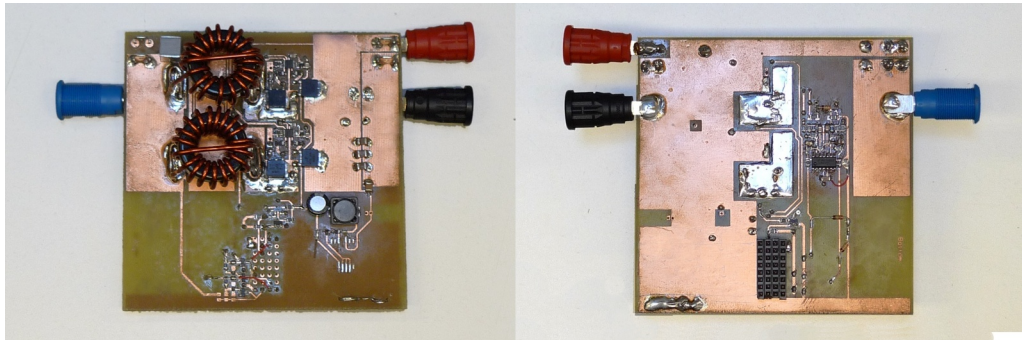
Figure 5.24: Dual interleaved buck converter built in the laboratory. Top side, show in the left picture, contains all power components: MOSFETs, inductors, gate drivers and filter capacitors. Bottom side of the PCB contains the current measurement circuit and a connector for the control board.
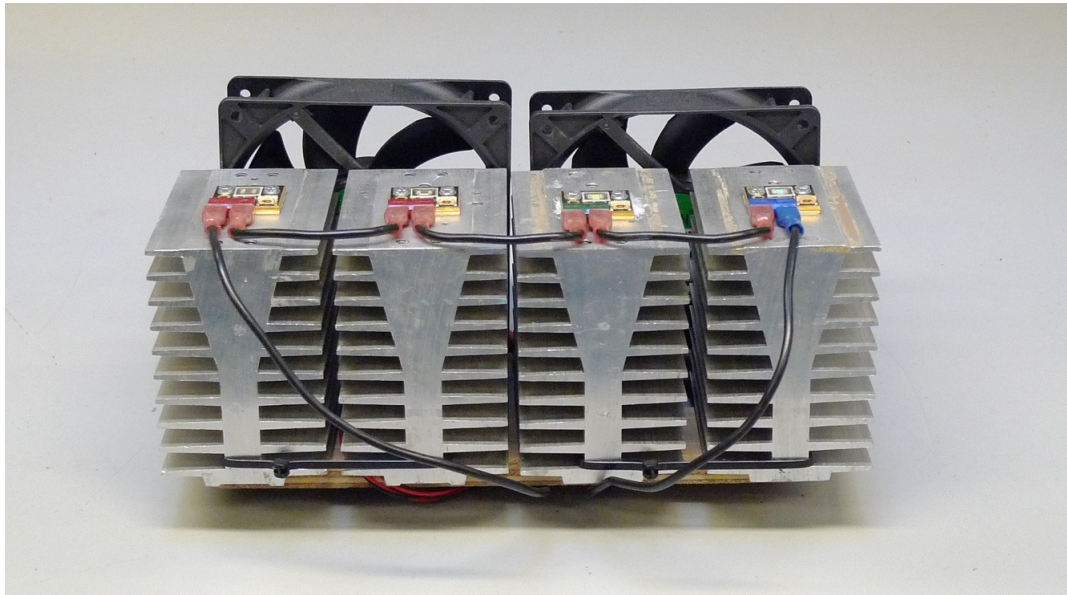
Figure 5.25: LED load used in the experiments composed of four series connected CBT-90 diodes.

Efficiency was measured with the previously shown load. Power needed to supply the DSP are not included in the efficiency calculations as one processor can be used for controlling multiple LED drivers and, at the same time, act as a colour controller.
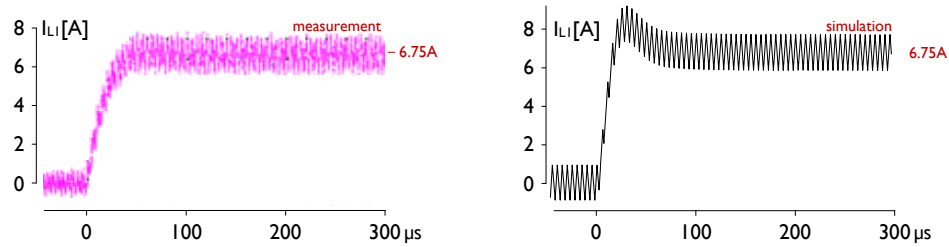
Figure 5.26: Measured (left) and simulated (right) current step in one of the phases of the converter. Gate driver losses are included in the measurement.
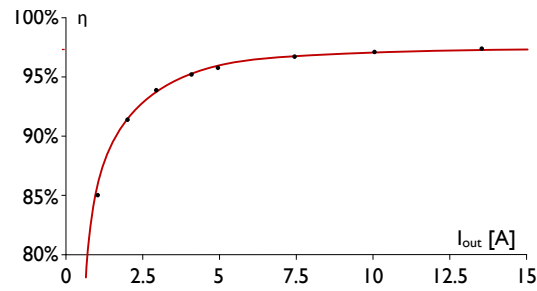
Figure 5.27: Measured efficiency of the LED driver supplying four, series connected green CBT-90 LEDS.

Figure 5.28: Thermal image of power converter driving four, series connected CBT-90 LEDS with 2 A, 20 W (left) and 13.5 A, 190 W (right). No forced cooling was used.

6 Conclusions

The aim of this work was to research LED driving solutions and to design a power converter for driving high power LED light sources. Thorough investigation of the previous scientific work showed three distinct research areas: LED properties (colorimetric, thermal, dimming, lifetime, etc.), luminaire control and LED drivers. Luminaire control 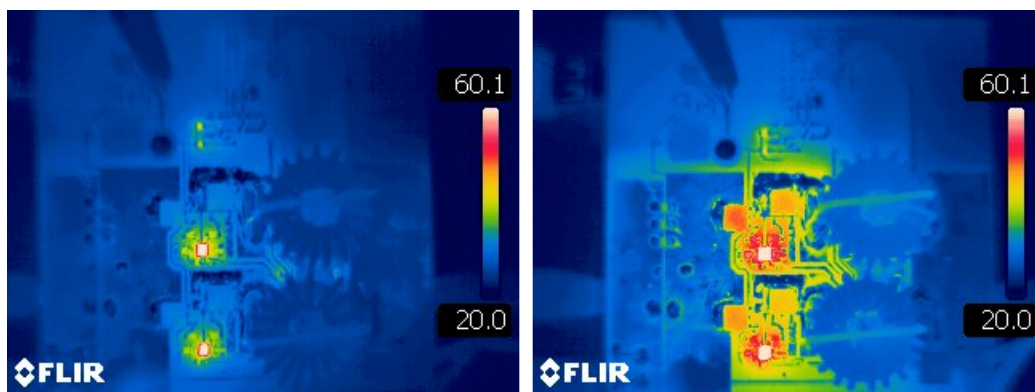work used the results of studies on diodes' properties together with the knowledge on colour theory to create colour control engines. However, little work bridges the gap between the colour control and LED drivers. While designing a LED driver, most of the focus is on topologies and converter lifetime and almost no focus is given to the driven diode. Similarly, researchers in the field of luminaire control treat LED drivers as black boxes where the only design choice is the dimming method. Therefore, in order to create an intelligent LED power converter, all three major research areas have been examined.

Previous research on pulse-width and amplitude modulation control show different effects, these methods have on diode performance and characteristics. It is therefore possible to drive the diode with any current shape to obtain different efficacy and colour points than with the two classical driving methods. To the hypothesis a diode was driven with a hybrid PWM/AM dimming mechanism. The choice of the driving current was made based on the observation that most commercial LED drivers offer both methods of control, so the implementation of this method in existing or future luminaires would not require much change in hardware design. Tests conducted in laboratory conditions proved that by using the hybrid dimming mechanism, many new control opportunities became possible.

HYBRID PWM/AM MODULATION

An observation that PWM and AM methods yield an opposite colour shift while dimming white phosphor-converted LED led to the discovery that by using the hybrid dimming mechanism one is able to control the position of the colour point and intensity of the diode. This phenomenon was used to stabilise the colour point that shifted with the heatsink temperature changes.

Similar effect on colour point was observed with green and blue InGaN diodes. The hybrid modulation was used to minimise the peak wavelength shift yielding a colour point moving inside the MacAdam ellipse throughout its dimming range. Future investigation should verify if this behaviour can be used to increase the accuracy of the colour sensors, as the spectrum shifts are the main cause of the measurement error.

Future research on this topic should include different driving currents, as the hybrid PWM/AM dimming is only a single example of the possible current shapes. Existing current control methods, like peak current control, are capable of controlling the current with very high bandwidth, therefore very complex current shapes

can easily be used to drive light-emitting diodes.

Review of luminaire control show various feedback mechanisms that stabilise the output light colour. Methods include measuring the colour or the intensity of the light and different indirect junction temperature measurement schemes. Junction temperature information is used, together with a model of the parameters change, to estimate diode colorimetric properties. Review of colour spaces and corresponding colour distance metrics shows that the ΔE_{ab}^* colour distance is a good measure of colour control loop accuracy.

Polychromatic luminaires, consisting of four or more LEDs, have been previously shown to have the possibility to optimise the control of primary diodes. The optimisation procedure can maximise various lamp parameters such as: efficacy, luminous flux or colour quality. Trichromatic luminaires did not have this ability using PWM or AM dimming methods. Research presented in this dissertation proved that by using the hybrid dimming mechanism, an increase in control allows the luminaire to optimise the same lamp parameters as in polychromatic luminaire consisting of more than three basic diodes. An increase of efficacy has been found, especially at lower intensity levels. An increased device gamut has been also shown, particularly in the cyan area of trichromatic RGB luminaire.

In this dissertation, a current-voltage diode model has been presented which utilises the fact that the diode's parameters depend on instantaneous values of junction temperature and forward current. Diode's voltage is dependent on its current and the junction temperature and is very easy to measure. It is therefore possible to create a model of diode's colorimetric and power properties based solely on instantaneous values of diode's current and voltage. The model was proved to generate accurate colorimetric feedback much under just noticeable ΔE_{ab}^* colour distance even under pulsed current conditions.

The current-voltage model can be applied to string connected light-emitting diodes but the accuracy of the method has not yet been verified in laboratory.

The model can be easily used in trichromatic luminaire colour control, where the only needed feedback value is the diode voltages. The instantaneous current information is taken from current command as the two values are different only during very short current settling transients.

Together with detailed thermal and electrical model of a diode, the model can provide a good platform for simulating colorimetric and power properties of the diode under different current shapes mentioned before. Current-voltage model can provide information about dissipated power to the detailed thermal model. The resulting junction temperature and driving current can be converted into forward voltage used in the current-voltage model. The accuracy of this complete luminaire description has not yet been proven and is a part of suggested future work. The detailed model has been used to show the effect of heastink thermal resistance on maximal achievable flux.

The data acquisition procedure used to create the current-voltage model is far from perfect as it includes the delays for thermally stabilising the luminaire system. As part of future work, the fact that the thermal time constant of LED structure and heatsink are much different should be utilised to increase the speed of the model generation. Also the means of generating the model of light-emitting diodes without the use of an actively controlled heatsink should be investigated. MODEL GENERATION PROCEDURE

The review of diodes' behaviour under different dimming mechanisms led to the conclusion that driving the diode with DC current yielded highest efficiency compared to other pulsed current methods. Therefore the converter should supply the diode with constant current of regulated value. Previous research also shows importance of lifetime analysis of the converter. The key component, limiting the lifetime of the converter, is assumed to be the electrolytic capacitor. As electrolytic capacitors are typically used in input and output of power converters as part of the filters, a topology minimising the need for these capacitors was investigated. The dual interleaved buck converter was built and tested driving four series connected high current CBT-90 diodes. This converter minimises the output current ripple using interleaving technique, where the current ripple from both phases cancel each other. Around 0.5 duty cycle this effect is the highest. Because of low series resistance of the light-emitting diodes, their voltage does not change much with the change of the driving current. The dual interleaved converter can be used with input voltage close to twice the forward voltage of the diode, therefore operating close to the 0.5 duty cycle in the whole diode current dimming range and thus minimising the need for output capacitor. POWER CONVERTER

117

Bibliography

[1] M. Dyble, N. Narendran, A. Bierman, and T. Klein. Impact of dimming white LEDs: chromaticity shifts due to different dimming methods. In I. T. Ferguson, J. C. Carrano, T. Taguchi, and I. E. Ashdown, editors, *Society of Photo-Optical Instrumentation Engineers (SPIE) Conference Series*, volume 5941, pages 291–299, 2005.

[2] Y. Gu, N. Narendran, T. Dong, and H. Wu. Spectral and luminous efficacy change of high-power LEDs under different dimming methods. volume 6337. SPIE, 2006.

[3] P. Manninen and P. Orreveteläinen. On spectral and thermal behaviors of AlGaInP light-emitting diodes under pulse-width modulation. *Applied Physics Letters*, 91(18):181121, 2007.

[4] I. Ashdown. Extended parallel pulse code modulation of LEDs. *Sixth International Conference on Solid State Lighting*, 6337(1):63370W, 2006.

[5] K.H. Loo, W.-K. Lun, S.-C. Tan, Y.M. Lai, and C.K. Tse. On the driving techniques for high-brightness LEDs. In *Energy Conversion Congress and Exposition, 2009. ECCE 2009. IEEE*, pages 2059–2064, 2009.

[6] M. Schmid, D. Kuebrich, M. Weiland, and T. Duerbaum. Evaluation on the efficiency of power LEDs driven with currents typical to switch mode power supplies. In *Industry Applications Conference, 2007. 42nd IAS Annual Meeting. Conference Record of the 2007 IEEE*, pages 1135–1140, 2007.

[7] Y. Xi and E. F. Schubert. Junction–temperature measurement in GaN ultraviolet light-emitting diodes using diode forward voltage method. *Applied Physics Letters*, 85(12):2163–2165, 2004.

[8] Y. Xi, J.-Q. Xi, Th. Gessmann, J. M. Shah, J. K. Kim, E. F. Schubert, A. J. Fischer, M. H. Crawford, K. H. A. Bogart, and A. A. Allerman. Junction and carrier temperature measurements in deep-ultraviolet light-emitting diodes using three different methods. *Applied Physics Letters*, 86(3):031907, 2005.

[9] S. Chhajed, Y. Xi, T. Gessmann, J.-Q. Xi, J. M. Shah, J. K. Kim, and E. F. Schubert. Junction temperature in light-emitting diodes assessed by different methods. In S. A. Stockman, H. W. Yao, and E. F. Schubert, editors, *Society of Photo-Optical Instrumentation Engineers (SPIE) Conference Series*, volume

5739 of *Society of Photo-Optical Instrumentation Engineers (SPIE) Conference Series*, pages 16–24, 2005.

[10] G. Farkas, Q. van Voorst Vader, A. Poppe, and Gy. Bognár. Thermal investigation of high power optical devices by transient testing. *Proc. of the 9th THERMINIC*, pages 213–218, 2003.

[11] V. Székely. Fine structure of heat flow path in semiconductor devices: A measurement and identification method. *Solid-State Electronics*, 31(9):1363–1368, 1988.

[12] S. Chhajed, Y. Xi, Y.-L. Li, Th. Gessmann, and E. F. Schubert. Influence of junction temperature on chromaticity and color-rendering properties of trichromatic white-light sources based on light-emitting diodes. *Journal of Applied Physics*, 97(5):054506, 2005.

[13] K. Man and I. Ashdown. Accurate colorimetric feedback for RGB LED clusters. In *Society of Photo-Optical Instrumentation Engineers (SPIE) Conference Series*, volume 6337 of *Society of Photo-Optical Instrumentation Engineers (SPIE) Conference Series*, 2006.

[14] J. Garcia, D.G. Lamar, M.A. Dalla-Costa, J.M. Alonso, and M.S. Rico. An estimator of luminous flux for enhanced control of high brightness LEDs. In *Power Electronics Specialists Conference, 2008. PESC 2008. IEEE*, pages 1852–1856, 2008.

[15] S.Y. Hui and Y.X. Qin. A general photo-electro-thermal theory for light emitting diode (LED) systems. *Power Electronics, IEEE Transactions on*, 24(8):1967–1976, 2009.

[16] B.-J. Huang, C.-W. Tang, and J.-H. Wu. Study of system dynamics of high-power LEDs. *Electronic Materials and Packaging, 2006. EMAP 2006. International Conference on*, pages 1–6, 2006.

[17] N. Narendran, Y. Gu, J. P. Freyssinier, H. Yu, and L. Deng. Solid-state lighting: failure analysis of white LEDs. *Journal of Crystal Growth*, 268(3-4):449 – 456, 2004. ICMAT 2003, Symposium H, Compound Semiconductors in Electronic an d Optoelectronic Applications.

[18] P. Jacob, A. Kunz, and G. Nicoletti. Reliability and wearout characterisation of LEDs. *Microelectronics and Reliability*, 46(9-11):1711–1714, 2006. Proceedings of the 17th European Symposium on Reliability of Electron Devices, Failure Physics and Analysis. Wuppertal, Germany 3rd-6th October 2006.

[19] J. Hu, L. Yang, and M. W. Shin. Electrical, optical and thermal degradation of high power GaN/InGaN light-emitting diodes. *Journal of Physics D Applied Physics*, 41(3):035107–+, 2008.

[20] P.N. Grillot, M.R. Krames, Hanmin Z., and Seng H.T. Sixty thousand hour light output reliability of AlGaInP light emitting diodes. *Device and Materials Reliability, IEEE Transactions on*, 6(4):564–574, 2006.

[21] M. Meneghini, S. Podda, A. Morelli, R. Pintus, L. Trevisanello, G. Meneghesso, M. Vanzi, and E. Zanoni. High brightness GaN LEDs degradation during DC and pulsed stress. *Microelectronics and Reliability*, 46(9-11):1720–1724, 2006. Proceedings of the 17th European Symposium on Reliability of Electron Devices, Failure Physics and Analysis. Wuppertal, Germany 3rd-6th October 2006.

[22] S. Buso, G. Spiazzi, M. Meneghini, and G. Meneghesso. Performance degradation of high-brightness light emitting diodes under DC and pulsed bias. *Device and Materials Reliability, IEEE Transactions on*, 8(2):312–322, 2008.

[23] P. Deurenberg, C. Hoelen, J. van Meurs, and J. Ansems. Achieving color point stability in RGB multi-chip LED modules using various color control loops. 5941:63–74, 2005.

[24] M. Subramanian, F.J.P Schuurmans, and M.D. Pashley. Red, green, and blue LEDs for white light illumination. *IEEE Journal of Selected Topics in Quantum Electronics*, 8:333–338, 2002.

[25] S. Muthu and J. Gaines. Red, green and blue LED-based white light source: implementation challenges and control design. In *Industry Applications Conference, 2003. 38th IAS Annual Meeting. Conference Record of the*, volume 1, page 515–522, 2003.

[26] B. Ackermann, V. Schulz, C. Martiny, A. Hilgers, and X. Zhu. Control of LEDs. In *Industry Applications Conference, 2006. 41st IAS Annual Meeting. Conference Record of the 2006 IEEE*, volume 5, pages 2608–2615, 2006.

[27] K. Lim, Joon Chok Lee, G. Panotopoulos, and R. Helbing. Illumination and color management in solid state lighting. In *Industry Applications Conference, 2006. 41st IAS Annual Meeting. Conference Record of the 2006 IEEE*, volume 5, pages 2616–2620, 2006.

[28] Y.N. Chang, C.C. Hung, S.C. Tung, and Sun-Yu Chan. Auto mixed light for rgb LED backlight module. In *Industrial Electronics, 2009. ISIE 2009. IEEE International Symposium on*, pages 864–869, 2009.

[29] S. Robinson and I. Ashdown. Polychromatic optical feedback control, stability, and dimming. In *Society of Photo-Optical Instrumentation Engineers (SPIE) Conference Series*, volume 6337 of *Society of Photo-Optical Instrumentation Engineers (SPIE) Conference Series*, 2006.

[30] O. Moisio, Pajula M., Pinho P., Halonen L., and Sepponen R. Use of junction temperature in control of CCT in LED luminaire. In *Proceedings of the CIE Midterm Meeting and International Lighting Congress*, pages 328–334, 2005.

[31] X. Qu, S.C. Wong, and C.K. Tse. Color control system for RGB LED light sources using junction temperature measurement. In *Industrial Electronics Society, 2007. IECON 2007. 33rd Annual Conference of the IEEE*, pages 1363–1368, 2007.

[32] B.-J. Huang and C.-W. Tang. Thermal-electrical-luminous model of multi-chip polychromatic LED luminaire. *Applied Thermal Engineering*, 29(16):3366–3373, 2009.

[33] A. Žukauskas, F. Ivanauskas, R. Vaicekauskas, M.S. Shur, and R. Gaska. Optimization of multichip white solid state lighting source with four or more LEDs. In I. T. Ferguson, Y.-S. Park, N. Narendran, & S. P. DenBaars, editor, *Society of Photo-Optical Instrumentation Engineers (SPIE) Conference Series*, volume 4445 of *Society of Photo-Optical Instrumentation Engineers (SPIE) Conference Series*, pages 148–155, 2001.

[34] H. Ries, I. Leike, and J. Muschaweck. Optimized additive mixing of colored light-emitting diode sources. *Optical Engineering*, 43(7):1531–1536, 2004.

[35] M. Ou-Yang and S.-W. Huang. Determination of gamut boundary description for multi-primary color displays. *Opt. Express*, 15(20):13388–13403, 2007.

[36] K.C. Lin. Approach for optimization of the color rendering index of light mixtures. *J. Opt. Soc. Am. A*, 27(7):1510–1520, 2010.

[37] H. van der Broeck, G. Sauerlander, and M. Wendt. Power driver topologies and control schemes for LEDs. In *Applied Power Electronics Conference, APEC 2007 - Twenty Second Annual IEEE*, pages 1319–1325, 2007.

[38] A. Torres, J. Garcia, M.R. Secades, A.J. Calleja, and J. Ribas. Advancing towards digital control for low cost high power LED drivers. In *Industrial Electronics, 2007. ISIE 2007. IEEE International Symposium on*, pages 3053–3056, 2007.

[39] X. Xu and X. Wu. High dimming ratio LED driver with fast transient boost converter. In *Power Electronics Specialists Conference, 2008. PESC 2008. IEEE*, pages 4192–4195, 2008.

[40] J.R. de Britto, A.E. Demian, L.C. de Freitas, V.J. Farias, E.A.A. Coelho, and J.B. Vieira. A proposal of LED lamp driver for universal input using Ćuk converter. In *Power Electronics Specialists Conference, 2008. PESC 2008. IEEE*, pages 2640–2644, 2008.

[41] T.F. Pan, H.J. Chiu, S.J. Cheng, and S.Y. Chyng. An improved single-stage flyback PFC converter for high-luminance lighting LED lamps. In *Electronic Measurement and Instruments, 2007. ICEMI '07. 8th International Conference on*, page 212–215, 2007.

[42] Z. Ye, F. Greenfeld, and Z. Liang. Offline SEPIC converter to drive the high brightness white LED for lighting applications. In *Industrial Electronics, 2008. IECON 2008. 34th Annual Conference of IEEE*, pages 1994–2000, 2008.

[43] Z. Xunwei, P. Xu, and F.C. Lee. A high power density, high efficiency and fast transient voltage regulator module with a novel current sensing and current sharing technique. In *Applied Power Electronics Conference and Exposition, 1999. APEC '99. Fourteenth Annual*, volume 1, pages 289–294 vol.1, 1999.

[44] M.R. Krames, O.B. Shchekin, R. Mueller-Mach, G.O. Mueller, L. Zhou, G. Harbers, and M.G. Craford. Status and future of high-power light-emitting diodes for solid-state lighting. *J. Display Technol.*, 3(2):160–175, 2007.

[45] R.-A. Moses and W. M. Hart. *Adler's Physiology of the Eye*. Mosby, 1987.

[46] J.J. Vos. Colorimetric and photometric properties of a 2-deg fundamental observer. *Color Research and Application*, 3:125–128, 1978.

[47] L.T. Sharpe, A. Stockman, W. Jagla, and H. Jägle. A luminous efficiency function, $V^\star(\lambda)$, for daylight adaptation. *Journal of Vision*, 5(11):948–968, 2005.

[48] W.S. Stiles and J.M. Burch. N.p.l. colour-matching investigation: Final report (1958). *Journal of Modern Optics*, 6:1–26, 1959.

[49] D. MacAdam. Visual sensitivities to color differences in daylight. *J. Opt. Soc. Am.*, 32(5):247–273, 1942.

[50] G. Wyszecki and W.S. Stiles. *Color Science: Concepts and Methods, Quantitative Data and Formulae (Wiley Series in Pure and Applied Optics)*. Wiley-Interscience, 2 edition, 2000.

[51] Y.-S. Kim, B.-H. Cho, B.-S Kang, and D.-I. Hong. US Patent No. US7024034, Color Temperature Conversion System and Method Using the Same, 2006.

[52] D.B. Judd, D.L. Macadam, G. Wyszecki, H.W. Budde, H.R. Condit, S.T. Henderson, and J.L. Simonds. Spectral distribution of typical daylight as a function of correlated color temperature. *J. Opt. Soc. Am.*, 54(8):1031–1040, Aug 1964.

[53] Method of measuring and specifying colour rendering properties. Technical Report 13.3, Commission Internationale de l´Eclairage, 1995.

[54] Y. Ohno. Simulation analysis of white LED spectra and color rendering. In *Proceedings for CIE Expert Sumposium on LED Light Sources*, 2004.

[55] Y. Ohno. Optical metrology for LEDs and solid state lighting. In *Fifth Symposium "Optics in Industry"*, volume 6046, 2006.

[56] J. Schanda and N. Sandor. Visual colour-rendering experiments. In *AIC Colour '05: 10th Congress of the International Colour Association*, pages 511–514, 2005.

[57] Colour Rendering of White LED Light Sources. Technical Report 177, Commission Internationale de l´Eclairage, 2007.

[58] J.P. Freyssinier and M. Rea. A two-metric proposal to specify the color-rendering properties of light sources for retail lighting. In *Society of Photo-Optical Instrumentation Engineers (SPIE) Conference Series*, volume 7784 of *Society of Photo-Optical Instrumentation Engineers (SPIE) Conference Series*, August 2010.

[59] M. Stokes, G. Sauerlander, M.D. Fairchild, and R.S. Berns. Precision requirements for digital color reproduction. In *ACM Transactions on Graphics*, volume 11, pages 406–422, 1992.

[60] C. Kittel. *Introduction to Solid State Physics*. John Wiley & Sons, Inc., 7th edition, 1996.

[61] J.-M. Liu. *Photonic Devices*. Cambridge University Press, 2005.

[62] J.-P. Colinge and C.A. Colinge. *Physics of semiconductor devices*. Springer, 2002.

[63] Y. C. Shen, G. O. Mueller, S. Watanabe, N. F. Gardner, A. Munkholm, and M. R. Krames. Auger recombination in ingan measured by photoluminescence. *Applied Physics Letters*, 91(14):141101, 2007.

[64] J. Hader, J. V. Moloney, B. Pasenow, S. W. Koch, M. Sabathil, N. Linder, and S. Lutgen. On the importance of radiative and Auger losses in GaN-based quantum wells. *Applied Physics Letters*, 92(26):261103, 2008.

[65] S.-H. Yen, M.-C. Tsai, M.-L. Tsai, Y.-J. Shen, T.-C. Hsu, and Y.-K. Kuo. Theoretical investigation of auger recombination on internal quantum efficiency of blue light-emitting diodes. *Applied Physics A: Materials Science & Processing*, 97:705–708, 2009. 10.1007/s00339-009-5298-8.

[66] Kish F.A. and Fletcher R.M.

[67] P. Roussel. SiC, Sapphire, and GaN materials status into opto and RF businesses. *The International Conference on Compound Semiconductor Manufacturing Technology*, 2006.

[68] E.F. Schubert. *Light-Emitting Diodes*. Cambridge University Press, 2006.

[69] Z. Hassan, N. Zainal, M. R. Hashim, and H. Abu Hassan. Simulation of high performance quantum well GaN-based LED. In *Physics and simulation of optoelectronic devices XIII*, volume 5722, pages 540–549, 2005.

[70] M.R. Krames, M. Ochiai-Holcomb, G.E. Höfler, C. Carter-Coman, E.I. Chen, I.-H. Tan, P. Grillot, N.F. Gardner, H.C. Chui, J.-W. Huang, S.A. Stockman, F.A. Kish, M.G. Craford, T.S. Tan, C.P. Kocot, M. Hueschen, J. Posselt, B. Loh, G. Sasser, and D. Collins. High-power truncated-inverted-pyramid $(Al_xGa_{1-x})_{0.5}In_{0.5}P$/GaP light-emitting diodes exhibiting > 50 % external quantum efficiency. *Applied Physics Letters*, 75:2365–+, 1999.

[71] J.J. Wierer, D.A. Steigerwald, M.R. Krames, J.J. OShea, M.J. Ludowise, G. Christenson, Y.-C. Shen, C. Lowery, P.S. Martin, S. Subramanya, W. Gotz, N.F. Gardner, R.S. Kern, and S.A. Stockman. High-power AlGaInN flip-chip light-emitting diodes. *Applied Physics Letters*, 78(22):3379 –3381, 2001.

[72] O.B. Shchekin, J.E. Epler, T.A. Trottier, T. Margalith, D.A. Steigerwald, M.O. Holcomb, P.S. Martin, and M.R. Krames. High performance thin-film flip-chip InGaN–GaN light-emitting diodes. *Applied Physics Letters*, 89(7):071109 –071109-3, 2006.

[73] C.C.Lee, W.V. Chen, and J. Park. A new i–v model for light-emitting devices with a quantum well. *Microelectronics Journal*, 37(11):1335 – 1338, 2006.

[74] T. Yoshizawa. *Handbook of Optical Metrology*. CRC Press, 2009.

[75] Min-Ho Kim, Martin F. Schubert, Qi Dai, Jong Kyu Kim, E. Fred Schubert, Joachim Piprek, and Yongjo Park. Origin of efficiency droop in GaN-based light-emitting diodes. *Applied Physics Letters*, 91(18):183507–183507–3, 2007.

[76] Jiuru Xu, Martin F. Schubert, Ahmed N. Noemaun, Di Zhu, Jong Kyu Kim, E. Fred Schubert, Min Ho Kim, Hun Jae Chung, Sukho Yoon, Cheolsoo Sone, and Yongjo Park. Reduction in efficiency droop, forward voltage, ideality factor, and wavelength shift in polarization-matched GaInN/GaInN multi-quantum-well light-emitting diodes. *Applied physics letters*, 94(1), 2009.

[77] J.C. Whitaker. *Microelectronics*. CRC Press, 2005.

[78] Y. P. Varshni. Temperature dependence of the energy gap in semiconductors. *Physica*, 34:149–154, 1967.

[79] I.A. Vainshtein, A.F. Zatsepin, and V.S. Kortov. Applicability of the empirical Varshni relation for the temperature dependence of the width of the band gap. *Physics of the Solid State*, 41:905–908, 1999.

[80] I. Vurgaftman, J. R. Meyer, and L. R. Ram-Mohan. Band parameters for III–V compound semiconductors and their alloys. *Journal of Applied Physics*, 89(11):5815–5875, 2001.

[81] A. Poppe, Y. Zhang, J. Wilson, G. Farkas, P. Szabo, J. Parry, M. Rencz, and V. Székely. Thermal measurement and modeling of multi-die packages. *Components and Packaging Technologies, IEEE Transactions on*, 32(2):484–492, 2009.

[82] A. Poppe, G. Molnar, and T. Temesvolgyi. Temperature dependent thermal resistance in power LED assemblies and a way to cope with it. In *Semiconductor Thermal Measurement and Management Symposium, 2010. SEMI-THERM 2010. 26th Annual IEEE*, pages 283–288, 2010.

[83] G. Marosy, Z. Ková, G. Molná, and A. Poppe. Diagnostics of LED-based streetlighting luminaires by means of thermal transient method. In *Thermal Investigations of ICs and Systems (THERMINIC), 2010 16th International Workshop on*, page 1–6, 2010.

[84] A. Poppe, G. Farkas, G. Molnár, B. Katona, T. Temesvölgyi, and J.-W. He. Emerging standard for thermal testing of power LEDs and its possible implementation. In *Society of Photo-Optical Instrumentation Engineers (SPIE) Conference Series*, volume 7784, 2010.

[85] L. Jayasinghe, T. Dong, and N. Narendran. Is the thermal resistance coefficient of high-power LEDs constant? In *Society of Photo-Optical Instrumentation Engineers (SPIE) Conference Series*, volume 6669 of *Society of Photo-Optical Instrumentation Engineers (SPIE) Conference Series*, 2007.

[86] Sheng-Liang Kuo, Chun-Kai Liu, Ming-Ji Dai, Chih-Kuang Yu, Heng-Chieh Chien, and Chung-Yen Hsu. Characteristics of thermal resistance for high power leds. In *Electronics Packaging Technology Conference, 2008. EPTC 2008. 10th*, pages 149 –154, 2008.

[87] R. Prasher. Thermal interface materials: Historical perspective, status, and future directions. *Proceedings of the IEEE*, 94(8):1571–1586, 2006.

[88] F. Cirolia and C. Finan. The effects of airborne contaminants on electronic power supplies. In *Applied Power Electronics Conference and Exposition, 2001. APEC 2001. Sixteenth Annual IEEE*, volume 1, pages 238–242, 2001.

[89] S.-C. Yang, P. Lin, C.-P. Wang, S.B. Huang, C.-L. Chen, P.-F. Chiang, A.-T. Lee, and M.-T. Chu. Failure and degradation mechanisms of high-power white light emitting diodes. *Microelectronics Reliability*, 50(7):959–964, 2010. Thermal, Mechanical and Multi-physics Simulation and Experiments in Micro-Electronics and Micro-Systems (EuroSimE 2009).

[90] N. Narendran and Y. Gu. Life of LED-based white light sources. *Journal of Display Technology*, 1(1):167–171, 2005.

[91] E. Zanoni. *Analysis of the Temperature impact on Reliability of GaN-based Light Emitting Diodes*. PhD thesis, Università degli Studi di Padova, 2008.

[92] Lighting Research Center, Rensselaer Polytechnic Institute. *LED Life for General Lighting*, 2005.

[93] Philips Lumileds Lighting Company. *Understanding power LED lifetime analysis*.

[94] Philips Lumileds Lighting Company. *Reliability Datasheet RD07: Luxeon Rebel reliability data*.

[95] C.W. Tyler and R.D. Hamer. Analysis of visual modulation sensitivity. IV. Validity of the Ferry-Porter law. *J. Opt. Soc. Am. A*, 7(4):743–758, 1990.

[96] W.-K. Lun, K.H. Loo, S.-C. Tan, Y.M. Lai, and C.K. Tse. Bilevel current driving technique for LEDs. *Power Electronics, IEEE Transactions on*, 24(12):2920–2932, 2009.

[97] K.H. Loo, W.-K. Lun, S.-C. Tan, Y.M. Lai, and C.K. Tse. On driving techniques for LEDs: Toward a generalized methodology. *Power Electronics, IEEE Transactions on*, 24(12):2967–2976, 2009.

[98] W.-K. Lun, K.H. Loo, S.-C. Tan, Y.M. Lai, and C.K. Tse. Implementation of bi-level current driving technique for improved efficacy of high-power LEDs. In *Energy Conversion Congress and Exposition, 2009. ECCE 2009. IEEE*, pages 2808–2814, 2009.

[99] I. Ashdown and M. Salsbury. Peak wavelength shifts and opponent color theory. In *Society of Photo-Optical Instrumentation Engineers (SPIE) Conference Series*, volume 6669, 2007.

[100] W. Howell. Application Note 011: An Overview of the Electronic Drive Technologies for Intensity Control and Colour Mixing of Low Voltage Light Sources Such As LEDs and LEPs. Technical report, Artistic License Inc., 2002.

[101] T.N.E. Greville. The pseudoinverse of a rectangular or singular matrix and its application to the solution of systems of linear equations. *SIAM Review*, 1(1):38–43, 1959.

[102] J. Garcia, M.A. Dalla-Costa, J. Cardesin, J.M. Alonso, and M. Rico-Secades. Dimming of high-brightness LEDs by means of luminous flux thermal estimation. *Power Electronics, IEEE Transactions on*, 24(4):1107–1114, 2009.

[103] A. Žukauskas, R. Vaicekauskas, F. Ivanauskas, R. Gaska, and M.S. Shur. Optimization of white polychromatic semiconductor lamps. *Applied Physics Letters*, 80(2):234–236, 2002.

[104] A. Žukauskas, R. Vaicekauskas, F. Ivanauskas, G. Kurilcik, Z. Bliznikas, K. Breive, J. Krupic, A. Rupsys, A. Novickovas, P. Vitta, A. Navickas, V. Raskauskas, M.S. Shur, and R. Gaska. Quadrichromatic white solid state lamp with digital feedback. In I. T. Ferguson, N. Narendran, S. P. DenBaars, and J. C. Carrano, editors, *Society of Photo-Optical Instrumentation Engineers (SPIE) Conference Series*, volume 5187 of *Society of Photo-Optical Instrumentation Engineers (SPIE) Conference Series*, pages 185–198, 2004.

[105] R.W. Erickson and D. Maksimovic. *Fundamentals of Power Electronics*. Springer, 2ed edition, 2001.

[106] Y.-M. Chen, H.-C. Wu, M.-W. Chou, and K.-Y. Lee. Online failure prediction of the electrolytic capacitor for LC filter of switching-mode power converters. *Industrial Electronics, IEEE Transactions on*, 55(1):400 –406, 2008.

[107] A. Consoli, A. Testa, G. Giannetto, and F. Gennaro. A new VRM topology for next generation microprocessors. *32nd Annual Power Electronics Specialists Conference, 2001. PESC. 2001 IEEE*, 1:339–344, 2001.

[108] J. Wei, P. Xu, H.-P. Wu, F.C. Lee, K. Yao, and M. Ye. Comparison of three topology candidates for 12 v VRM. In *Applied Power Electronics Conference and Exposition, 2001. APEC 2001. Sixteenth Annual IEEE*, volume 1, pages 245–251, 2001.

[109] K.-J. Åström and B. Wittenmark. *Computer controlled systems*. Prentice Hall, 1996.

[110] H.P. Forghani-zadeh and G.A. Rincon-Mora. A lossless, accurate, self-calibrating current-sensing technique for DC-DC converters. In *Industrial Electronics Society, 2005. IECON 2005. 31st Annual Conference of IEEE*, 2005.

[111] L. Hua and S. Luo. Design considerations of time constant mismatch problem for inductor DCR current sensing method. In *Applied Power Electronics Conference and Exposition, 2006. APEC '06. Twenty-First Annual IEEE*, pages 7 pp.–, 2006.

[112] P.R. Lethellier. Method and apparatus for sensing output inductor current in a DC-DC power converter. United States Patent 6,441,597, 2002.

[113] E. Dallago, M. Passoni, and G. Sassone. Lossless current sensing in low-voltage high-current dc/dc modular supplies. *Industrial Electronics, IEEE Transactions on*, 47(6):1249–1252, 2000.

[114] P. Midya, M. Greuel, and P.T. Krein. Sensorless current mode control-an observer-based technique for DC-DC converters. In *Power Electronics Specialists Conference, 1997. PESC '97 Record., 28th Annual IEEE*, volume 1, pages 197–202 vol.1, 1997.

[115] A.M. Patel and M. Ferdowsi. Advanced current sensing techniques for power electronic converters. In *Vehicle Power and Propulsion Conference, 2007. VPPC 2007. IEEE*, pages 524–530, 2007.

[116] L. Balogh. Design and application guide for high speed MOSFET gate drive circuits. Texas Instruments Application Note.